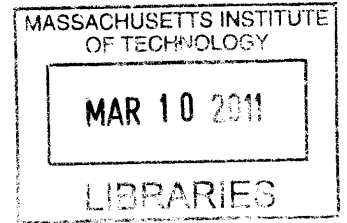


Analyzing and Improving Image Quality in Reflective Ghost Imaging

by

Nicholas D. Hardy



Submitted to the Department of Electrical Engineering and Computer
Science

in partial fulfillment of the requirements for the degree of **ARCHIVES**

Master of Science in Electrical Engineering and Computer Science

at the

MASSACHUSETTS INSTITUTE OF TECHNOLOGY

February 2011

© Massachusetts Institute of Technology 2011. All rights reserved.

Author
Department of Electrical Engineering and Computer Science
January 27, 2011

Certified by
Jeffrey W. Shapiro
Julius A. Stratton Prof. of Elec. Eng.
Thesis Supervisor

Accepted by
Terry P. Orlando
Chairman, Committee on Graduate Students

Report Documentation Page

Form Approved
OMB No. 0704-0188

Public reporting burden for the collection of information is estimated to average 1 hour per response, including the time for reviewing instructions, searching existing data sources, gathering and maintaining the data needed, and completing and reviewing the collection of information. Send comments regarding this burden estimate or any other aspect of this collection of information, including suggestions for reducing this burden, to Washington Headquarters Services, Directorate for Information Operations and Reports, 1215 Jefferson Davis Highway, Suite 1204, Arlington VA 22202-4302. Respondents should be aware that notwithstanding any other provision of law, no person shall be subject to a penalty for failing to comply with a collection of information if it does not display a currently valid OMB control number.

1. REPORT DATE FEB 2011	2. REPORT TYPE	3. DATES COVERED 00-00-2011 to 00-00-2011	
4. TITLE AND SUBTITLE Analyzing and Improving Image Quality in Reflective Ghost Imaging		5a. CONTRACT NUMBER	
		5b. GRANT NUMBER	
		5c. PROGRAM ELEMENT NUMBER	
6. AUTHOR(S)		5d. PROJECT NUMBER	
		5e. TASK NUMBER	
		5f. WORK UNIT NUMBER	
7. PERFORMING ORGANIZATION NAME(S) AND ADDRESS(ES) Massachusetts Institute of Technology, 77 Massachusetts Avenue, Cambridge, MA, 02139		8. PERFORMING ORGANIZATION REPORT NUMBER	
9. SPONSORING/MONITORING AGENCY NAME(S) AND ADDRESS(ES)		10. SPONSOR/MONITOR'S ACRONYM(S)	
		11. SPONSOR/MONITOR'S REPORT NUMBER(S)	
12. DISTRIBUTION/AVAILABILITY STATEMENT Approved for public release; distribution unlimited			
13. SUPPLEMENTARY NOTES			
14. ABSTRACT Ghost imaging is a transverse imaging technique that relies on the correlation between a pair of light fields, one that has interacted with the object to be imaged and one that has not. Most ghost imaging experiments have been performed in transmission, and virtually all ghost imaging theory has addressed the transmissive case. Yet stand-off sensing applications require that the object be imaged in reflection. We use Gaussian-state analysis to develop expressions for the spatial resolution, image contrast, and signal-to-noise ratio for ghost imaging performed by measuring a fraction of the light that reflects off a rough-surfaced object that creates target returns with fully developed speckle. This is done for a pseudothermal source with phase-insensitive classical correlation between the two fields, and for a quantum source with non-classical phase-sensitive correlation between the fields. In the low flux limit this quantum source becomes the biphoton state. We compare our results to the corresponding behavior seen in transmissive ghost imaging, and we develop performance results for the reflective form of computational ghost imaging. We also provide a preliminary stand-off sensing performance comparison between reflective ghost imaging and a conventional direct-detection laser radar system. We also consider the resolution degradation on each system when the fields propagate through turbulence. Finally, we investigate ways of increasing the signal-to-noise ratio of reflective ghost imaging through use of multiple bucket detectors, multiple-wavelength sources, and compressive sensing.			
15. SUBJECT TERMS			
16. SECURITY CLASSIFICATION OF:			17. LIMITATION OF ABSTRACT
a. REPORT unclassified	b. ABSTRACT unclassified	c. THIS PAGE unclassified	Same as Report (SAR)
			18. NUMBER OF PAGES 93
			19a. NAME OF RESPONSIBLE PERSON

Analyzing and Improving Image Quality in Reflective Ghost Imaging

by

Nicholas D. Hardy

Submitted to the Department of Electrical Engineering and Computer Science
on January 27, 2011, in partial fulfillment of the
requirements for the degree of
Master of Science in Electrical Engineering and Computer Science

Abstract

Ghost imaging is a transverse imaging technique that relies on the correlation between a pair of light fields, one that has interacted with the object to be imaged and one that has not. Most ghost imaging experiments have been performed in transmission, and virtually all ghost imaging theory has addressed the transmissive case. Yet stand-off sensing applications require that the object be imaged in reflection. We use Gaussian-state analysis to develop expressions for the spatial resolution, image contrast, and signal-to-noise ratio for ghost imaging performed by measuring a fraction of the light that reflects off a rough-surfaced object that creates target returns with fully developed speckle. This is done for a pseudo-thermal source with phase-insensitive classical correlation between the two fields, and for a quantum source with non-classical phase-sensitive correlation between the fields. In the low flux limit this quantum source becomes the biphoton state. We compare our results to the corresponding behavior seen in transmissive ghost imaging, and we develop performance results for the reflective form of computational ghost imaging. We also provide a preliminary stand-off sensing performance comparison between reflective ghost imaging and a conventional direct-detection laser radar system. We also consider the resolution degradation on each system when the fields propagate through turbulence. Finally, we investigate ways of increasing the signal-to-noise ratio of reflective ghost imaging through use of multiple bucket detectors, multiple-wavelength sources, and compressive sensing.

Thesis Supervisor: Jeffrey H. Shapiro

Title: Julius A. Stratton Prof. of Elec. Eng.

Acknowledgments

The completion of this thesis would not have been possible without the intellectual contributions, support, and patience of several people, all of whom I would like to thank. First is my advisor, Professor Jeffrey Shapiro, for his patient guidance and luminous instruction throughout my studies, and careful editing of this thesis. Next is Dr. Franco Wong, for his tutelage in my first few months at MIT, the experience I gained in his lab, and for insightful conversations since. This thesis heavily leveraged framework and theory developed by Dr. Baris Erkmen, whom I would like to thank for his efforts.

I would like to thank my parents, David and Catherine Hardy, for their support, encouragement, and always providing a place to call home. I also would like to thank Beverly Chu for her tireless support, editing of this thesis, and for always being my touchstone. Lastly, I would like to thank my fellow members of the Optical and Quantum Communications Group for our shared struggles and triumphs over this last year, and my friends and family for much needed respites.

This work was supported by the U.S. Army MURI Grant No. W911NF-05-0197, and the W. M. Keck Foundation Center for Extreme Quantum Information Theory.

Contents

1	Introduction	9
2	Ghost Imaging with Pseudothermal Light	13
2.1	Theoretical Setup	13
2.2	Spatial Resolution and Image Contrast	17
2.3	Signal-to-Noise Ratio	21
3	Ghost Imaging with Non-Classical Light	27
3.1	Theoretical Setup	27
3.2	Resolution and Contrast	31
3.3	Signal-to-Noise Ratio	33
4	Computational Reflective Ghost Imaging	37
4.1	Theoretical Setup	37
4.2	Comparison to Pseudothermal Ghost Imager	39
5	Comparison to a Laser Radar System	43
5.1	Theoretical Setup	43
5.2	Spatial Resolution and Image Contrast	45
5.3	Signal-to-Noise Ratio	46
6	Evaluation of Turbulence Effects	49
6.1	Turbulence Review	49

6.2	Classical Source	52
6.2.1	Resolution analysis	52
6.2.2	Special cases	55
6.3	Non-classical Source	56
6.4	Laser Radar	58
7	Improving Ghost Image Quality	61
7.1	Multiple Bucket Detectors	62
7.2	Multiple Wavelengths	66
7.3	Compressive Sensing	70
8	Conclusion and Future Work	75
A	Detailed SNR Derivation	79
A.1	Pseudothermal Ghost Imager	79
A.1.1	Source fluctuations noise term, T_1	81
A.1.2	Remaining noise terms	85
A.2	SPDC Ghost Imager	87

Chapter 1

Introduction

In this thesis we explore the viability of using ghost imaging for stand-off sensing. To this end we characterize the image quality of such systems, and compare the results to the image quality of an equivalent laser radar system. We connect our work back to previous theory developed for transmissive ghost imaging, as well as to experiments done in reflection. Finally, we explore ways to improve the quality of reflective ghost imaging. The most promising of these approaches is the application of compressive sensing, which leverages the structure of natural images to reduce image capture time while improving image quality.

Ghost imaging exploits the correlation between two light fields to create an image that neither field alone could provide. We denote these two fields the “signal” and “reference”: the signal field interacts with the target, after which a single-pixel “bucket” detector makes a power measurement of the field; simultaneously, the reference field’s transverse power distribution is measured with a high spatial-resolution detector, which is usually a scanning pinhole or a CCD array. The signal and reference fields have some cross correlation, determined by the choice of source, so measuring the reference field provides some knowledge of the field illuminating the target. Since the power measurement on the signal arm is a function of the target and the field illuminating it, we are able to reconstruct the target by correlating the power measurement with the output of the high spatial-resolution detector. This imaging technique has become known as ghost imaging because the image information

is contained in the correlation between the two measurements: neither measurement alone contains sufficient information to reconstruct the target.

The first ghost imaging experiment used biphoton pairs for the signal and reference fields, which were generated by spontaneous parametric downconversion (SPDC) and post-selection [1]. Because biphotons are entangled states—with a phase-sensitive cross correlation between the signal and reference fields stronger than allowed by classical physics—for which the quantum theory of photodetection is needed to calculate the measurement statistics, it was initially thought that ghost imaging was a non-local quantum phenomenon. However, the non-classical nature of ghost imaging was called into question when experiments were later performed using a classical pseudothermal light source [2, 3]. In this setup laser light is passed through a ground-glass diffuser, after which it is divided by a 50-50 beam splitter into identical signal and reference fields with a phase-insensitive cross correlation.

Gaussian-state analysis has enabled a unified treatment of biphoton and pseudothermal ghost imaging that shows the image formation process is one of classical coherence propagation, with high contrast in DC-coupled biphoton ghost images being the principal ghost-image signature of that non-classical source [4]. In particular, identical statistics for pseudothermal ghost imaging result from the use of quantum photodetection theory, in which both the light beams and photodetectors are treated quantum-mechanically; and semiclassical photodetection theory, in which the light beams are treated classically but photodetectors inject shot noise on top of any fluctuations in the illumination. A thorough review of these considerations can be found in [5]. For our purposes, it suffices to note that we can—and will—use semiclassical photodetection theory when dealing with classical sources.

To date, Gaussian-state analysis of transmissive pseudothermal ghost imaging has provided expressions for its spatial resolution, image contrast and signal-to-noise ratio (SNR) behaviors; i.e., a complete characterization of its performance [4, 6]. However, one of the more interesting potential applications of ghost imaging is stand-off sensing, in which the bucket detector observes the target in reflection, not transmission. Preliminary table-top experiments have demonstrated the feasibility of this approach [7, 8], but there has been little

exploration of the statistical characteristics of these images. Developing that theory within the Gaussian-state framework, which is a focus of this thesis, must confront an additional complication not seen in previous work; viz., the speckle induced by reflection from rough-surfaced objects. In particular, we shall report expressions for the spatial resolution, image contrast, and SNR of reflective ghost imaging of speckle targets for classical and non-classical sources in Chapters 2 and 3, respectively. These will be compared with the corresponding results for the transmissive case, in which there is no target-induced speckle. In Chapter 4 we will use this framework to obtain performance results for the reflective form of computational ghost imaging [9, 10], in which the reference beam is removed. Then, in Chapter 5, we will provide a preliminary stand-off sensing performance comparison between reflective ghost imaging and a conventional direct-detection laser radar.

The effects of turbulence on transmissive ghost imaging have been explored experimentally [8] and theoretically [11]. As most practical applications of reflective ghost imaging will require propagation through atmospheric turbulence, in Chapter 6 we extend our analysis to include turbulence on all paths. The effects of turbulence on image resolution will be explored for classical, non-classical, and computational reflective ghost imaging, as well as for a laser radar system. In Chapter 7 we explore ways to improve the image quality of reflective ghost imaging. The first of these methods is to employ multiple co-planar bucket detectors on the signal arm; since the target-induced speckle decorrelates with transverse separation in the detector plane, each bucket detector observes different speckle behavior, allowing us to average out its deleterious effects on the SNR. The second method is to use multiple sources at different wavelengths. This again seeks to average out the target-speckle effects: if the wavelengths are far enough apart, the returns associated with each source have uncorrelated speckle statistics. Finally, we extend the compressive sensing methods used in transmissive imaging [12] to reflective imaging. Compressive sensing allows for reduced image capture time and higher quality reconstructions when the target is sparsely represented in some basis [13, 14]. Chapter 8 concludes the thesis with a brief summary of results and suggestions for further research.

Chapter 2

Ghost Imaging with Pseudothermal Light

2.1 Theoretical Setup

In stand-off sensing, targets will most likely be separated from the source by distances on the order of kilometers. This indicates that high-powered classical sources might be necessary. While we also consider low-flux quantum sources in Chapter 3, we start our analysis with the system shown in Fig. 2-1, which utilizes pseudothermal light to perform reflective ghost imaging. A continuous-wave (cw) laser beam is passed through a rotating ground-glass diffuser followed by a 50/50 beam splitter to produce identical, spatially-incoherent signal and reference beams whose temporal bandwidths are much lower than those of the single-pixel (bucket) and high spatial-resolution (CCD array) detectors. The signal beam illuminates a rough-surfaced planar target at distance L from the beam splitter, and some of the light reflected from that target is collected, after L -m propagation, by the bucket detector. The reference beam directly illuminates the CCD array which, for theoretical convenience, we have placed L -m away from the beam splitter.¹ The photocurrents from the bucket detector

¹This assumption implies that we will form a 1:1 ghost image. In an actual implementation of reflective ghost imaging the CCD array would be in the focal plane of a lens located near the transmitter and we would obtain a minified ghost image.

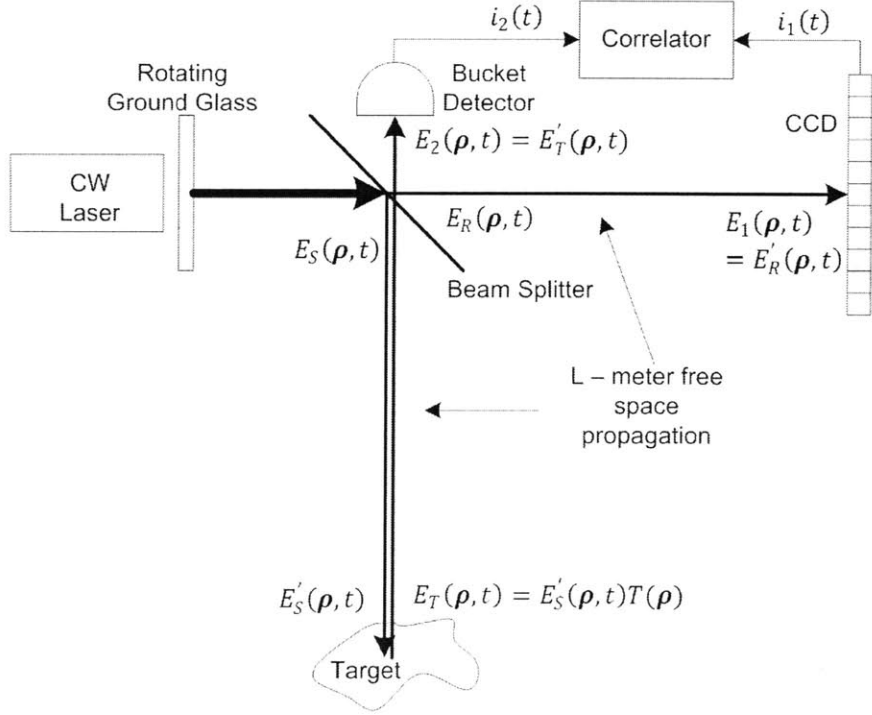


Figure 2-1: Setup for pseudothermal reflective ghost imaging.

and each pixel on the CCD are sent to a correlator, whose output for the CCD pixel located at transverse coordinate ρ_1 is

$$C(\rho_1) = \frac{1}{T_I} \int_{-T_I/2}^{T_I/2} dt i_1(t) i_2(t), \quad (2.1)$$

where T_I is the averaging time and we have suppressed an L/c time delay in $i_1(t)$ that is needed to account for the delay incurred by the light returning from the target.

The configuration and notation we are using parallels the semiclassical treatment of transmissive ghost imaging in [9] with the principal distinction being that in the transmissive case the bucket detector would be behind a transmission-mask target L -m from the signal source, whereas here that target is viewed in reflection. We have also switched the labels for the signal and reference fields; in [9] the reference field illuminates the target, while the signal field goes to the high spatial-resolution detector.

All the fields shown in Fig. 2-1 are complex envelopes about center frequency ω_0 of

linearly-polarized light fields normalized to have $\sqrt{\text{photons/m}^2\text{s}}$ units as functions of their transverse coordinate vectors and time. As a result, under the assumption of shot-noise limited detectors with quantum efficiency η , the photocurrents from the bucket and the CCD can be written as

$$i_m(t) = \int d\tau [q\eta P_m(\tau) + \Delta i_m(\tau)] h(t - \tau), \quad \text{for } m = 1, 2. \quad (2.2)$$

Here: $P_m(t) = \int_{\mathcal{A}_m} d\boldsymbol{\rho} |E_m(\boldsymbol{\rho}, t)|^2$ is the photon flux on the circular active region \mathcal{A}_m of detector m ; q is the electron charge; $\Delta i_m(t)$ is the shot noise from detector m ; and $h(t)$ is the detector's baseband impulse response, normalized to satisfy $\int dt h(t) = 1$. Physically, $q\eta P_m(t)$ is the conditional mean of $i_m(t)$, given the illumination, so that $\Delta i_m(t)$ is the photocurrent fluctuation conditioned on knowledge of the illumination. Note that given the photon-flux waveforms $P_1(t)$ and $P_2(t)$, the shot-noise currents $\Delta i_1(t)$ and $\Delta i_2(t)$ are statistically independent, zero-mean, random processes whose correlation functions are $\langle \Delta i_m(t_1) \Delta i_m(t_2) \rangle = q^2 \eta P_m(t_1) \delta(t_1 - t_2)$.

The fields that determine the preceding photon fluxes are found from diffraction theory, applied on three separate paths: the reference path (R), from the source to the high spatial-resolution detector; the signal path (S), from the source to the target; and the target-return path (T), from the target to the bucket detector. In the ensuing work, we will denote fields that have propagated L -m on path m with a prime; i.e., if we start with some field $E_m(\boldsymbol{\rho}', t)$, after L -m propagation it becomes $E'_m(\boldsymbol{\rho}, t)$ as

$$E'_m(\boldsymbol{\rho}, t) = \int d\boldsymbol{\rho}' E_m(\boldsymbol{\rho}', t) \frac{k_0 e^{ik_0(L+|\boldsymbol{\rho}-\boldsymbol{\rho}'|^2/2L)}}{i2\pi L} \quad m = R, S, T, \quad (2.3)$$

where $k_0 = \omega_0/c$ is the wave number, and we have suppressed time delays. The fields are defined as follows: $E_R(\boldsymbol{\rho}, t)$ is the reference field at the source, and $E'_R(\boldsymbol{\rho}, t)$ is the field illuminating the CCD; $E_S(\boldsymbol{\rho}, t)$ is the signal field at the source, and $E'_S(\boldsymbol{\rho}, t)$ is the field illuminating the target; $E_T(\boldsymbol{\rho}, t) = E'_S(\boldsymbol{\rho}, t)T(\boldsymbol{\rho})$ is the target-return field, which is

the propagated signal field immediately after reflecting off a target² with field-reflection coefficient $T(\boldsymbol{\rho})$, and $E'_T(\boldsymbol{\rho}, t)$ is the field illuminating the bucket detector. Since we are using the semiclassical theory of light, each photodetector is taken to directly measure the classical field impinging it, so $E_1(\boldsymbol{\rho}, t) = E'_R(\boldsymbol{\rho}, t)$, and $E_2(\boldsymbol{\rho}, t) = E'_T(\boldsymbol{\rho}, t)$.

Whereas in transmissive ghost imaging it is ordinarily the case that the target's field-transmission coefficient is assumed to be deterministic, the targets of interest for reflective ghost imaging will have microscopic surface variations—from a nominal, smooth surface profile whose standard deviations can greatly exceed the illumination wavelength and whose transverse correlation scale can be sub-wavelength. When such a surface is illuminated by laser light it gives rise to laser speckle in the target return, and a reasonable statistical model for that behavior is to take the target reflectivity to be

$$T(\boldsymbol{\rho}) = \sqrt{\mathcal{T}(\boldsymbol{\rho})} e^{2ik_0\Delta z(\boldsymbol{\rho})}, \quad (2.4)$$

where the height variations $\Delta z(\boldsymbol{\rho})$ are modeled as a zero-mean, real-valued, Gaussian random process with a transverse correlation on the order of a wavelength. Thus $T(\boldsymbol{\rho})$ is a zero-mean, complex-valued Gaussian random process that is completely characterized by the correlation function [15]

$$\langle T^*(\boldsymbol{\rho}_1)T(\boldsymbol{\rho}_2) \rangle = \lambda_0^2 \mathcal{T}(\boldsymbol{\rho}_1) \delta(\boldsymbol{\rho}_1 - \boldsymbol{\rho}_2), \quad (2.5)$$

where λ_0 is the center wavelength of the illumination and $\mathcal{T}(\boldsymbol{\rho})$ is the target's intensity-reflection coefficient, which is nonrandom and the quantity that we are seeking to image with the Fig. 2-1 setup.

In order to proceed further, we need to specify the source-field characteristics. Following the Gaussian-state analysis of Erkmen and Shapiro [4, 6, 9], we shall assume that $E_S(\boldsymbol{\rho}, t)$ and $E_R(\boldsymbol{\rho}, t)$ —the identical outputs from the 50–50 beam splitter in Fig. 2-1—are zero-mean, complex-valued Gaussian random fields that are completely characterized by their common

²We have assumed a stationary target, so that its field-reflection coefficient is constant in time.

cross-spectrally pure phase-insensitive correlation function per the Gaussian-Schell model as

$$\langle E_\ell^*(\boldsymbol{\rho}_1, t_1) E_m(\boldsymbol{\rho}_2, t_2) \rangle = \frac{2P}{\pi a_0^2} e^{-(|\boldsymbol{\rho}_1|^2 + |\boldsymbol{\rho}_2|^2)/a_0^2 - |\boldsymbol{\rho}_1 - \boldsymbol{\rho}_2|^2/2\rho_0^2} e^{-(t_2 - t_1)^2/2T_0^2}, \quad \ell, m \in \{R, S\}. \quad (2.6)$$

with photon-flux P , e^{-2} intensity radius a_0 , coherence length ρ_0 , and correlation time T_0 .

The preceding setup fully specifies all that is needed to compute the spatial resolution, image contrast, and SNR of the pseudothermal reflective ghost image. Before doing so, however, let us introduce one final condition. We shall assume that the CCD pixel active region, \mathcal{A}_1 , is sufficiently small that $|E_1(\boldsymbol{\rho}, t)|^2$ is essentially constant over each pixel, allowing us to use $P_1(t) = A_1 |E_1(\boldsymbol{\rho}, t)|^2$, where A_1 is the area of \mathcal{A}_1 . This condition ensures that the spatial resolution we obtain is limited by the field statistics, not by the CCD's pixel size.

2.2 Spatial Resolution and Image Contrast

The spatial resolution and image contrast of the pseudothermal reflective ghost image are properties of the ensemble-averaged photocurrent cross correlation, i.e., Eq (2.1) averaged over the shot noise and the fluctuations in the fields that illuminate the two detectors. Those field fluctuations arise from the randomness imposed by the ground-glass diffuser and, for the field illuminating the bucket detector, the target's surface roughness. It is easy to see that the fields illuminating the detectors are zero-mean random processes that are statistically stationary in time, and thus from Eq (2.2) the ensemble-averaged ghost image satisfies

$$\begin{aligned} \langle C(\boldsymbol{\rho}_1) \rangle &= \langle i_1(t) i_2(t) \rangle \\ &= q^2 \eta^2 A_1 \int d\tau_1 \int d\tau_2 h(t - \tau_1) h(t - \tau_2) \int_{\mathcal{A}_2} d\boldsymbol{\rho}' \langle |E'_R(\boldsymbol{\rho}_1, \tau_1)|^2 |E'_T(\boldsymbol{\rho}', \tau_2)|^2 \rangle, \end{aligned} \quad (2.7)$$

Back propagating with Eq (2.3) to the field illuminating the target, the intensity correlation becomes

$$\begin{aligned} \langle |E'_R(\boldsymbol{\rho}_1, \tau_1)|^2 |E'_T(\boldsymbol{\rho}', \tau_2)|^2 \rangle &= \frac{k_0^2}{4\pi^2 L^2} \int d\boldsymbol{\rho}_2 \int d\boldsymbol{\rho}_3 e^{ik_0(|\boldsymbol{\rho}' - \boldsymbol{\rho}_3|^2 - |\boldsymbol{\rho}' - \boldsymbol{\rho}_2|^2)/2L} \\ &\times \langle E_R'^*(\boldsymbol{\rho}_1, \tau_1) E_S'^*(\boldsymbol{\rho}_2, \tau_2) E'_R(\boldsymbol{\rho}_1, \tau_1) E'_S(\boldsymbol{\rho}_3, \tau_2) \rangle \langle T^*(\boldsymbol{\rho}_2) T(\boldsymbol{\rho}_3) \rangle, \end{aligned} \quad (2.8)$$

where we have exploited the statistical independence of $E'_m(\boldsymbol{\rho}, t)$ and $T(\boldsymbol{\rho})$, i.e., the fluctuations due to propagation through the ground glass and those induced by the target's surface roughness. Equation (2.3) shows that $E'_m(\boldsymbol{\rho}, t)$, for $m = R, S$, is a linear transformation of the zero-mean Gaussian random process $E_m(\boldsymbol{\rho}, t)$; hence it too is a zero-mean, Gaussian random process. Thus, as in the Gaussian-state analysis of transmissive ghost imaging [4], we employ Gaussian moment-factoring to write the fourth-order field moment in terms of second-order moments. Making use of Eq (2.5) to evaluate the surface moment, and for A_2 being the area of \mathcal{A}_2 , Eq (2.8) becomes

$$\begin{aligned} \langle |E'_R(\boldsymbol{\rho}_1, \tau_1)|^2 |E'_T(\boldsymbol{\rho}', \tau_2)|^2 \rangle \\ = \frac{A_2}{L^2} \int d\boldsymbol{\rho}_2 \mathcal{T}(\boldsymbol{\rho}_2) [\langle |E'_R(\boldsymbol{\rho}_1, \tau_1)|^2 \rangle \langle |E'_S(\boldsymbol{\rho}_2, \tau_2)|^2 \rangle + |\langle E_R'^*(\boldsymbol{\rho}_1, \tau_1) E'_S(\boldsymbol{\rho}_2, \tau_2) \rangle|^2] \end{aligned} \quad (2.9)$$

which clearly indicates the role of photon-flux correlation in ghost image formation.

Pseudothermal ghost imaging is performed with spatially incoherent light, i.e., $\rho_0 \ll a_0$ holds in the source's Gaussian-Schell model spatial correlation. Moreover, stand-off sensing pseudothermal ghost imaging will be performed in the far field, for which $k_0 a_0 \rho_0 / 2L \ll 1$ prevails. Following Erkmen and Shapiro [5], we can propagate the Gaussian-Schell correlation function in Eq (2.6) into the far field and obtain

$$\langle E_\ell'^*(\boldsymbol{\rho}_1, t_1) E_m'(\boldsymbol{\rho}_2, t_2) \rangle = \frac{2P}{\pi a_L^2} e^{\frac{ik_0}{2L}(|\boldsymbol{\rho}_2|^2 - |\boldsymbol{\rho}_1|^2)} e^{-(|\boldsymbol{\rho}_1|^2 + |\boldsymbol{\rho}_2|^2)/a_L^2 - |\boldsymbol{\rho}_1 - \boldsymbol{\rho}_2|^2/2\rho_L^2} e^{-(t_2 - t_1)^2/2T_0^2} \quad (2.10)$$

for $\ell, m \in \{R, S\}$, with $a_L = 2L/k_0\rho_0$ and $\rho_L = 2L/k_0a_0$ being the new intensity and coherence radii, respectively.

To reduce Eq (2.7) to a form in which we can easily assess the reflective ghost image's spatial resolution and image contrast, we need to define detector's impulse response $h(t)$. For now, let us take this to be a DC-coupled Gaussian of bandwidth Ω_B ,³ i.e.,

$$h(t) = \frac{\Omega_B}{\sqrt{8\pi}} e^{-\Omega_B^2 t^2/8}. \quad (2.11)$$

Because we have assumed that the detector bandwidth is sufficient to follow the temporal behavior of the light emerging from the ground glass, we have that $\Omega_B T_0 \gg 1$. This lets us simplify the evaluation of the temporal integrals and obtain

$$\langle C(\boldsymbol{\rho}_1) \rangle = \frac{q^2 \eta^2 A_1 A_2}{L^2} \left(\frac{2P}{\pi a_L^2} \right)^2 \int d\boldsymbol{\rho}_2 \mathcal{T}(\boldsymbol{\rho}_2) e^{-2(|\boldsymbol{\rho}_1|^2 + |\boldsymbol{\rho}_2|^2)/a_L^2} [1 + e^{-|\boldsymbol{\rho}_1 - \boldsymbol{\rho}_2|^2/\rho_L^2}]. \quad (2.12)$$

When the intensity radius a_L is much larger than the target's transverse extent, so that the entire target is uniformly illuminated on average, we get our final form for the ensemble-averaged photocurrent cross correlation,

$$\langle C(\boldsymbol{\rho}_1) \rangle = \frac{q^2 \eta^2 A_1 A_2}{L^2} \left(\frac{2P}{\pi a_L^2} \right)^2 \int d\boldsymbol{\rho}_2 \mathcal{T}(\boldsymbol{\rho}_2) [1 + e^{-|\boldsymbol{\rho}_1 - \boldsymbol{\rho}_2|^2/\rho_L^2}]. \quad (2.13)$$

Equation (2.13) shows that the ensemble-average photocurrent cross correlation consists of a featureless background term,

$$C_0 = \frac{q^2 \eta^2 A_1 A_2}{L^2} \left(\frac{2P}{\pi a_L^2} \right)^2 \int d\boldsymbol{\rho}_2 \mathcal{T}(\boldsymbol{\rho}_2), \quad (2.14)$$

plus the image-bearing term,

$$C_1(\boldsymbol{\rho}_1) = \frac{q^2 \eta^2 A_1 A_2}{L^2} \left(\frac{2P}{\pi a_L^2} \right)^2 \int d\boldsymbol{\rho}_2 \mathcal{T}(\boldsymbol{\rho}_2) e^{-|\boldsymbol{\rho}_1 - \boldsymbol{\rho}_2|^2/\rho_L^2}. \quad (2.15)$$

Resolution The image-bearing term contains the target's intensity-reflection coefficient $\mathcal{T}(\boldsymbol{\rho}_2)$ convolved with a Gaussian point-spread function (PSF) that limits the spatial resolu-

³The frequency response associated with this impulse response is $H(\Omega) = \int dt h(t) e^{-i\Omega t} = e^{-2\Omega^2/\Omega_B^2}$.

tion to the target-plane coherence length $\rho_L = \lambda_0 L / \pi a_0$. This is the same spatial resolution that was previously found via Gaussian-state analysis for far-field transmissive ghost imaging with a pseudothermal source [4]. Indeed, the only difference between Eq (2.15) and the corresponding result for the transmissive case is the factor A_2/L^2 that appears in the former. In transmissive ghost imaging all the light that passes through the target is collected by the bucket detector, but the quasi-Lambertian nature of the rough-surfaced target combines with the stand-off measurement by the bucket detector to introduce the solid-angle subtense factor $A_2/L^2 \ll 1$ in Eq (2.15).

Contrast Turning now to the image contrast implied by Eq (2.13), we will employ the contrast definition from [4], viz.

$$\mathcal{C} = \frac{\max_{\mathcal{R}}[C(\boldsymbol{\rho}_1)] - \min_{\mathcal{R}}[C(\boldsymbol{\rho}_1)]}{C_0}, \quad (2.16)$$

with the assumption that the target is entirely contained within a region \mathcal{R} centered at the origin in transverse coordinates and having a diameter that is much smaller than a_L . For simplicity, we will also assume that ρ_L is small enough to resolve all features in the target's intensity-reflection coefficient, so that

$$\int d\boldsymbol{\rho}_2 \mathcal{T}(\boldsymbol{\rho}_2) e^{-|\boldsymbol{\rho}_1 - \boldsymbol{\rho}_2|^2 / \rho_L^2} \approx \pi \rho_L^2 \mathcal{T}(\boldsymbol{\rho}_1), \quad (2.17)$$

and we will take $\max_{\mathcal{R}}[\mathcal{T}(\boldsymbol{\rho}_1)] = 1$, $\min_{\mathcal{R}}[\mathcal{T}(\boldsymbol{\rho}_1)] = 0$. Thus

$$\mathcal{C} \approx \pi \rho_L^2 / A_T, \quad (2.18)$$

where $A_T = \int d\boldsymbol{\rho}_2 \mathcal{T}(\boldsymbol{\rho}_2)$ is the effective area of the target. Thus $\mathcal{C} \approx 1/\text{number of on-target resolution cells}$. This image contrast coincides with what was previously derived for DC-coupled transmissive ghost imaging in far-field operation in [4].

2.3 Signal-to-Noise Ratio

The featureless background that we encountered in the preceding section can be eliminated by means of AC-coupling one or both of the photodetectors in the Fig. 2-1 setup, as has sometimes been done in pseudothermal ghost-imaging experiments [16]. SNR analysis for transmissive ghost imaging is simplified substantially by inclusion of such AC-coupled detectors [6], so we shall take the same route here by assuming that the photodetectors' baseband frequency response include a DC block. Specifically, the detectors' frequency response is now modeled by

$$H_B(\Omega) = e^{-2\Omega^2/\Omega_B^2} - e^{-2\Omega^2/\Omega_N^2}, \quad (2.19)$$

where the DC-notch bandwidth, Ω_N , is much smaller than both Ω_B , the detectors' high-frequency cutoff, and $1/T_0$, the source bandwidth.⁴ With this AC-coupling we have that the average photocurrent cross correlation is background free, viz., Eq (2.13) becomes

$$\langle C(\boldsymbol{\rho}_1) \rangle = \frac{q^2 \eta^2 A_1 A_2}{L^2} \left(\frac{2P}{\pi a_L^2} \right)^2 \int d\boldsymbol{\rho}_2 \mathcal{T}(\boldsymbol{\rho}_2) e^{-|\boldsymbol{\rho}_1 - \boldsymbol{\rho}_2|^2 / \rho_L^2}. \quad (2.20)$$

Thus it is appropriate to define the ghost image's SNR at the image point $\boldsymbol{\rho}_1$ via

$$\text{SNR} = \frac{\langle C(\boldsymbol{\rho}_1) \rangle^2}{\text{Var}[C(\boldsymbol{\rho}_1)]} = \frac{\langle C(\boldsymbol{\rho}_1) \rangle^2}{\langle C^2(\boldsymbol{\rho}_1) \rangle - \langle C(\boldsymbol{\rho}_1) \rangle^2}, \quad (2.21)$$

i.e, it is the ratio of the squared strength of the image component of the photocurrent cross correlation divided by the variance of that cross correlation.

Equation (2.20) provides an expression for the numerator in Eq (2.21) and the second term in its denominator. However, to simplify our results, we shall assume that ρ_L is sufficiently small to resolve all features in $\mathcal{T}(\boldsymbol{\rho})$, reducing Eq (2.20) to

$$\langle C(\boldsymbol{\rho}_1) \rangle = \frac{A_1 A_2 q^2 \eta^2}{L^2} \left(\frac{2P}{\pi a_L^2} \right)^2 \pi \rho_L^2 \mathcal{T}(\boldsymbol{\rho}_1). \quad (2.22)$$

⁴Because we have assumed a narrowband pseudothermal source, $\Omega_N T_0 \ll 1$ is a more stringent condition than $\Omega_N \ll \Omega_B$.

This leaves us with the formidable task of evaluating

$$\langle C^2(\boldsymbol{\rho}_1) \rangle = \frac{1}{T_I^2} \int_{-T_I/2}^{T_I/2} dt \int_{-T_I/2}^{T_I/2} du \langle i_1(t) i_2(t) i_1(u) i_2(u) \rangle, \quad (2.23)$$

which requires us to determine an eighth moment of the fields and a fourth moment of the target's field-reflection coefficient. Fortunately, Gaussian-moment factoring can be applied to both of these moment evaluations, but the Fresnel-propagation kernels that canceled out in finding the average photocurrent cross correlation do not do so here. We can simplify the analysis by using the dimensionless difference coordinate $\boldsymbol{\nu} = \rho_L k_0 (\boldsymbol{\rho}' - \boldsymbol{\rho}'')/L$, where $\boldsymbol{\rho}'$ and $\boldsymbol{\rho}''$ are coordinates at the bucket detector, and defining

$$A'_T = \int d\boldsymbol{\rho} \mathcal{T}^2(\boldsymbol{\rho}), \quad (2.24)$$

$$A'_F = \int d\boldsymbol{\xi} |\mathbb{T}(\boldsymbol{\xi})|^2 O(\boldsymbol{\xi}, 4\alpha/\rho_L), \quad (2.25)$$

$$\Gamma = \frac{1}{2\pi} \int d\boldsymbol{\nu} e^{-|\boldsymbol{\nu}|^2/2} O(\boldsymbol{\nu}, 4\alpha), \quad (2.26)$$

where $O(\boldsymbol{\zeta}, D)$ is the dimensionless version of the two-circle overlap function for circles of diameter D ,

$$O(\boldsymbol{\zeta}, D) = \begin{cases} \left[\cos^{-1} \left(\frac{|\boldsymbol{\zeta}|}{D} \right) - \frac{|\boldsymbol{\zeta}|}{D} \sqrt{1 - \frac{|\boldsymbol{\zeta}|^2}{D^2}} \right] \frac{2}{\pi}, & |\boldsymbol{\zeta}| \leq D \\ 0, & \text{else} \end{cases}, \quad (2.27)$$

$\alpha = \sqrt{A_2/\pi a_0^2}$, and $\mathbb{T}(\boldsymbol{\xi}) = \mathcal{F}[\mathcal{T}(\boldsymbol{\rho})](\boldsymbol{\xi})$ is the Fourier transform of the target. Γ was normalized so that it approaches one for very large receiving apertures; i.e., $\lim_{\alpha \rightarrow \infty} \Gamma = 1$. Next, we assume that $A'_T/\rho_L^2 \gg 30$, which is equivalent to saying that the ghost image consists of at least 10×10 resolution cells. The full derivation under these conditions is

shown in the Appendix, with the resulting SNR being

$$\text{SNR} = \frac{\mathcal{T}^2(\rho_1) \frac{T_I}{T_0}}{\frac{A'_T + A'_F \frac{a_0^2}{4\pi A_2}}{\sqrt{2\pi\rho_L^2}} + \mathcal{T}^2(\rho_1) \frac{T_I}{T_0} \frac{\Gamma\pi a_0^2}{2A_2} + \frac{\mathcal{T}(\rho_1)}{\eta\mathcal{I}} \frac{L^2}{A_2} + \frac{\pi\rho_L^2 \mathcal{T}^2(\rho_1)}{A_1\eta\mathcal{I}} \left[\frac{4}{3} + \frac{a_0^2}{4\pi A_2} \right] + \frac{\mathcal{T}(\rho_1) T_0 \Omega_B \rho_L^2 \sqrt{\pi}}{16\sqrt{2} A_1 \eta^2 \mathcal{I}^2} \frac{L^2}{A_2}}, \quad (2.28)$$

where $\mathcal{I} = PT_0\rho_L^2/a_L^2$ is the source brightness in photons per spatiotemporal mode.

Equation (2.28) was written in its full form to allow for any size bucket detector. This is useful when looking at small bucket detectors, such that $A_2 \rightarrow 0$; even for high-brightness illumination and a long integration time, we are limited in such situations to $\text{SNR} \leq 1$ because there is no averaging of the target-induced speckle. However, for a lensed ghost imaging system it is reasonable to assume that the area of the collecting lens in front of the bucket detector is at least as large as the area of the source beam, or $A_2/\pi a_0^2 \geq 1$. In this regime, we can simplify Eq (2.28) to

$$\text{SNR} = \frac{\mathcal{T}^2(\rho_1) \frac{T_I}{T_0}}{\frac{A'_T}{\sqrt{2\pi\rho_L^2}} + \mathcal{T}^2(\rho_1) \frac{T_I}{T_0} \frac{\Gamma\pi a_0^2}{2A_2} + \frac{\mathcal{T}(\rho_1)}{\eta\mathcal{I}} \frac{L^2}{A_2} + \frac{4\pi\rho_L^2 \mathcal{T}^2(\rho_1)}{3A_1\eta\mathcal{I}} + \frac{\mathcal{T}(\rho_1) T_0 \Omega_B \rho_L^2 \sqrt{\pi}}{16\sqrt{2} A_1 \eta^2 \mathcal{I}^2} \frac{L^2}{A_2}}. \quad (2.29)$$

The terms in the noise denominator of Eq (2.29), which originate from different combinations of field variations and shot noises, have important physical interpretations. From left to right in that denominator we have: the noise contributed by target-plane speckle from the pseudothermal illumination; the noise contributed by the speckle on the bucket detector arising from the target's surface roughness; the beat noise between the pseudothermal speckle on the CCD pixel and the bucket detector's shot noise; the beat noise between the CCD pixel's shot noise and the pseudothermal speckle on the bucket detector; and the beat noise between the shot noises on the two detectors. From here it is of interest to look at the low-brightness ($\mathcal{I} \ll 1$) and high-brightness ($\mathcal{I} \gg 1$) SNR asymptotes. These are given by

$$\text{SNR}_L = \frac{16\sqrt{2} T_I}{\sqrt{\pi}} \frac{A_1 \eta^2 \mathcal{I}^2}{T_0 \Omega_B T_0 \rho_L^2} \mathcal{T}(\rho_1) \frac{A_2}{L^2}, \quad (2.30)$$

and

$$\text{SNR}_H = \frac{\mathcal{T}^2(\boldsymbol{\rho}_1) \frac{T_I}{T_0}}{\frac{A'_T}{\sqrt{2\pi\rho_L^2}} + \mathcal{T}^2(\boldsymbol{\rho}_1) \frac{T_I}{T_0} \frac{\Gamma\pi a_0^2}{2A_2}}, \quad (2.31)$$

respectively.

The low-brightness SNR is dominated by the beat noise between the detectors' shot noises. It coincides with the low-brightness SNR found for transmissive ghost imaging [6], except for the following two differences: the reflective case has the target's average intensity-reflection coefficient, $\mathcal{T}(\boldsymbol{\rho}_1)$, appearing in lieu of transmissive target's $|T(\boldsymbol{\rho}_1)|^2$; and the reflective case includes the solid-angle scaling factor, A_2/L^2 , previously encountered in our comparison of the these ghost imagers' spatial resolutions.

The reflective ghost imager's high-brightness SNR asymptote is controlled by the two speckle terms from Eq (2.29), i.e., the speckle arising from the pseudothermal source's spatial incoherence and the speckle arising from the target's surface roughness. Neither speckle noise can be said to universally dominate the high-brightness SNR asymptote, as their relative strengths are governed by both spatial and temporal factors. We need to look at two limiting cases: when the integration time is short enough that the source's spatial incoherence dominates the noise, and when the integration time is long enough that the target-induced speckle dominates the noise. These short integration-time and long integration-time, high-brightness SNR asymptotes are

$$\text{SNR}_{H, \text{short-}T_I} = \sqrt{2\pi} \frac{T_I}{T_0} \frac{\rho_L^2}{A'_T} \mathcal{T}^2(\boldsymbol{\rho}_1), \quad (2.32)$$

and

$$\text{SNR}_{H, \text{long-}T_I} = \frac{2A_2}{\Gamma\pi a_0^2}. \quad (2.33)$$

Here we see the short integration-time, high-brightness SNR for reflective ghost imaging equals the high-brightness SNR for transmissive ghost imaging with $\mathcal{T}^2(\boldsymbol{\rho}_1)$ appearing instead of $|T(\boldsymbol{\rho}_1)|^4$. This agreement is to be expected, as both of these SNRs are limited by the speckle created by the pseudothermal illumination. However, as the integration time

increases, the high-brightness SNR for the reflective case saturates at the value given by Eq (2.33). Here the SNR is limited by the target-induced speckle. Because we have assumed a stationary target whose field-reflection coefficient is constant, no amount of post-detector integration will reduce its speckle noise, and SNR saturation occurs. Furthermore, this effect can be severe: for $A_2/\pi a_0^2 = 1$ we find $\text{SNR}_{H,\text{long}T_I} = 3.266$, and for $A_2/\pi a_0^2 = 2$ we have $\text{SNR}_{H,\text{long}T_I} = 5.54$. So, for realistic stand-off sensing, the SNR will be limited to single-digit values if no further measures are taken to average out the target-induced speckle.

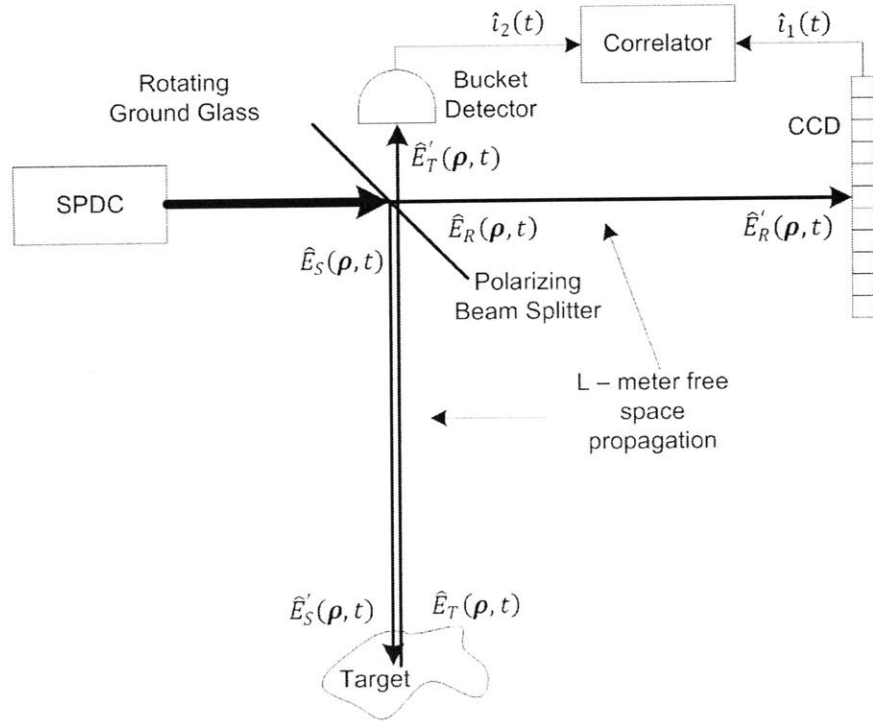
Chapter 3

Ghost Imaging with Non-Classical Light

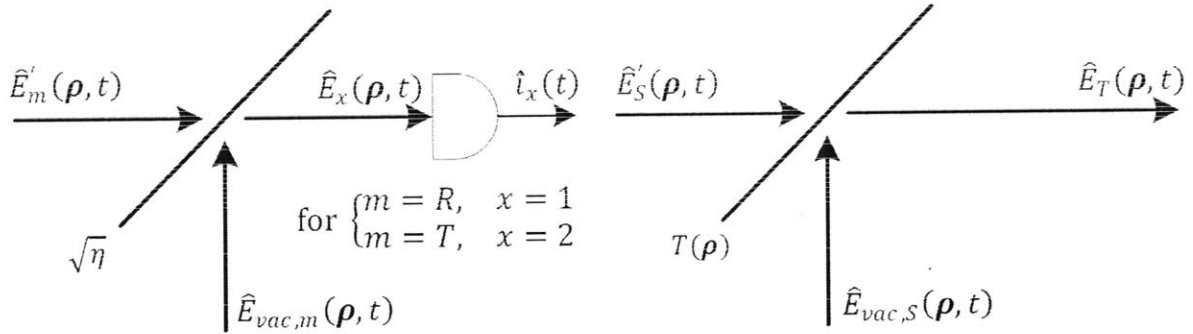
3.1 Theoretical Setup

Our analysis of reflective ghost imaging in Chapter 2 focused on a pseudothermal light source with classical phase-insensitive correlation between the signal and reference fields. This setup was chosen because we felt it most closely resembled a system that could be reliably constructed for experimentation. However, it behooves us to consider alternative light sources, especially those with quantum entanglement between the signal and reference fields. In this chapter we derive the resolution, contrast, and SNR for ghost imagers with phase-sensitive correlation between the signal and reference fields. We work within a Gaussian-state framework as done in [4], exploring correlations ranging from the classical limit up to the quantum limit. But first, we need to reframe our setup in terms of quantum mechanics, as shown in Figs. 3-1(a), 3-1(b), and 3-1(c).

We start by replacing the signal and reference fields at the source with their associated



(a) The output from an SPDC is passed through a polarizing beam splitter, creating signal and reference fields from the signal and idler photons which have a non-classical cross correlation.



(b) For sub-unity quantum efficiency detectors we have to account for the loss, and inject vacuum to get, the reflected field has suffered loss. We therefore preserve the field commutator relationship. This relationship is given in Eq (3.6), and is analogous to the field and vacuum passing through a spatially varying beam splitter of transmissivity $T(\rho)$.
(c) Since some light is transmitted through the target to account for the loss, and inject vacuum to get, the reflected field has suffered loss. We therefore preserve the field commutator relationship. This relationship is given in Eq (3.6), and is analogous to the field and vacuum passing through a spatially varying beam splitter of transmissivity $T(\rho)$.

Figure 3-1: The setup in Fig. 2-1 is reframed in terms of quantum mechanics. The source is changed, the classical fields become field operators, and we have to inject vacuum at the detectors and target to preserve commutator brackets.

field operators $\hat{E}_S(\boldsymbol{\rho}, t)$ and $\hat{E}_R(\boldsymbol{\rho}, t)$. These fields obey the commutator relations

$$[\hat{E}_\ell(\boldsymbol{\rho}_1, t_1), \hat{E}_m(\boldsymbol{\rho}_2, t_2)] = 0, \quad (3.1)$$

$$[\hat{E}_\ell(\boldsymbol{\rho}_1, t), \hat{E}_m^\dagger(\boldsymbol{\rho}_2, t_2)] = \delta_{\ell,m} \delta(\boldsymbol{\rho}_1 - \boldsymbol{\rho}_2) \delta(t_1 - t_2), \quad (3.2)$$

where $\ell, m \in \{S, R, T\}$. The propagation of the classical fields in Eq (2.3) becomes its operator counterpart

$$\hat{E}'_m(\boldsymbol{\rho}, t) = \int d\boldsymbol{\rho}' \hat{E}_m(\boldsymbol{\rho}', t) \frac{k_0 e^{ik_0(L+|\boldsymbol{\rho}-\boldsymbol{\rho}'|^2/2L)}}{i2\pi L} \quad \text{for } m = R, S, T. \quad (3.3)$$

The signal and reference field operators have the same basic interpretation as their classical counterparts, i.e., having the statistics of zero-mean Gaussian random processes, but the target-return field description has changed. In order to preserve the field commutator relations in Eqs (3.1) and (3.2), we have to inject vacuum to compensate for the loss at the target, as shown in Fig. 3-1(c) and modeled as

$$E_T(\boldsymbol{\rho}, t) = \hat{E}'_S(\boldsymbol{\rho}, t)T(\boldsymbol{\rho}) + \hat{E}_{vac.S}(\boldsymbol{\rho}, t)\sqrt{1 - |T(\boldsymbol{\rho})|^2}, \quad (3.4)$$

where $\hat{E}_{vac.S}(\boldsymbol{\rho}, t)$ is a vacuum-state field operator.⁵

The photodetectors can now be thought of as making a measurement of a quantum field operator. Since we are dealing with sub-unity quantum efficiency detectors, we have to inject vacuum-state field operators to maintain the field commutator relationships at the detectors, as shown in Fig. 3-1(b). Thus, our photocurrent is a measurement of the quantum operator

$$\hat{i}_x(t) = q \int d\tau \int_{\mathcal{A}_x} d\boldsymbol{\rho} \hat{E}_x^\dagger(\boldsymbol{\rho}, \tau) \hat{E}_x(\boldsymbol{\rho}, \tau) h(t - \tau) \quad \text{for } x = 1, 2, \quad (3.5)$$

⁵Strictly speaking, this expression requires $|T(\boldsymbol{\rho})|^2 \leq 1$ for all $\boldsymbol{\rho}$, which conflicts with the statistics we have assumed for the field reflection coefficient. However, the A_2/L angular subtense factor that we will encounter on the target return will make our statistics a reasonable approximation for the detected field operator. Also note that the vacuum-state field operator will not contribute to the bucket-detector output.

where

$$\hat{E}_x(\boldsymbol{\rho}, t) = \sqrt{\eta} \hat{E}'_m(\boldsymbol{\rho}, t) + \sqrt{1 - \eta} \hat{E}_{vac,m}(\boldsymbol{\rho}, t), \quad (3.6)$$

and $x = 1$ for $m = R$, and $x = 2$ for $m = T$. For this treatment our source will be an SPDC, whose output is Gaussian-state light with a phase-sensitive cross correlation between the signal and reference (signal and idler) fields given by [5, 6]

$$\begin{aligned} \langle \hat{E}_R(\boldsymbol{\rho}_1, t_1) \hat{E}_S(\boldsymbol{\rho}_2, t_2) \rangle &= \frac{2P}{\pi a_0^2} e^{-(|\boldsymbol{\rho}_1|^2 + |\boldsymbol{\rho}_2|^2)/a_0^2} \\ &\times \left[e^{-|\boldsymbol{\rho}_2 - \boldsymbol{\rho}_1|^2/2\rho_0^2} e^{-(t_2 - t_1)^2/2T_0^2} + i \left(\frac{2}{\pi} \right)^{\frac{1}{4}} \sqrt{\frac{a_0^2}{PT_0\rho_0^2}} e^{-|\boldsymbol{\rho}_2 - \boldsymbol{\rho}_1|^2/\rho_0^2} e^{-(t_2 - t_1)^2/T_0^2} \right]. \end{aligned} \quad (3.7)$$

The fields will be taken to have no phase-insensitive cross correlation, no phase-sensitive autocorrelation, and a phase-insensitive autocorrelation given by

$$\langle \hat{E}_m^\dagger(\boldsymbol{\rho}_1, t_1) \hat{E}_m(\boldsymbol{\rho}_2, t_2) \rangle = \frac{2P}{\pi a_0^2} e^{-(|\boldsymbol{\rho}_1|^2 + |\boldsymbol{\rho}_2|^2)/a_0^2 - |\boldsymbol{\rho}_1 - \boldsymbol{\rho}_2|^2/2\rho_0^2} e^{-(t_2 - t_1)^2/2T_0^2}, \quad m = R, S. \quad (3.8)$$

Looking at the Gaussian-state cross correlation function in Eq (3.7) we see two separate correlations. In the low-brightness limit the second term becomes dominant, and the state can be approximated as a biphoton state with a correlation much stronger than the classical limit. Conversely, in the high-brightness limit the first term dominates, and the light approaches a classical state, with the correlation being the same as for the Gaussian-Schell model in Chapter 2. Equation (3.7) captures this full quantum-to-classical behavior, allowing us to say that at low-brightness we have an entangled biphoton state, and at high-brightness we have a classical state with phase-sensitive cross correlation between signal and reference fields.

3.2 Resolution and Contrast

To evaluate the resolution and contrast, we follow the same procedure as for classical light; i.e., we look at an ensemble average of the product of the photocurrents as

$$\begin{aligned}\langle \hat{C}(\boldsymbol{\rho}_1) \rangle &= \langle \hat{i}_1(t) \hat{i}_2(t) \rangle \\ &= q^2 A_1 \int d\tau_1 \int d\tau_2 h(t - \tau_1) h(t - \tau_2) \int_{\mathcal{A}_2} d\boldsymbol{\rho}' \langle \hat{E}_1^\dagger(\boldsymbol{\rho}_1, \tau_1) \hat{E}_2^\dagger(\boldsymbol{\rho}', \tau_2) \hat{E}_1(\boldsymbol{\rho}_1, \tau_1) \hat{E}_2(\boldsymbol{\rho}', \tau_2) \rangle.\end{aligned}$$

Substituting in Eq (3.6) and recognizing the independence of the zero-mean vacuum fluctuations from the field fluctuations, we have

$$\langle \hat{E}_1^\dagger(\boldsymbol{\rho}_1, \tau_1) \hat{E}_2^\dagger(\boldsymbol{\rho}', \tau_2) \hat{E}_1(\boldsymbol{\rho}_1, \tau_1) \hat{E}_2(\boldsymbol{\rho}', \tau_2) \rangle = \eta^2 \langle \hat{E}_R^\dagger(\boldsymbol{\rho}_1, \tau_1) \hat{E}_T^\dagger(\boldsymbol{\rho}', \tau_2) \hat{E}'_R(\boldsymbol{\rho}_1, \tau_1) \hat{E}'_T(\boldsymbol{\rho}', \tau_2) \rangle.$$

From Eq (3.3) we then find that

$$\begin{aligned}\langle \hat{E}_R^\dagger(\boldsymbol{\rho}_1, \tau_1) \hat{E}_T^\dagger(\boldsymbol{\rho}', \tau_2) \hat{E}'_R(\boldsymbol{\rho}_1, \tau_1) \hat{E}'_T(\boldsymbol{\rho}', \tau_2) \rangle &= \frac{k_0^2}{4\pi^2 L^2} \int d\boldsymbol{\rho}_2 \int d\boldsymbol{\rho}_3 e^{ik_0(|\boldsymbol{\rho}' - \boldsymbol{\rho}_3|^2 - |\boldsymbol{\rho}' - \boldsymbol{\rho}_2|^2)/2L} \\ &\times \langle \hat{E}_R^\dagger(\boldsymbol{\rho}_1, \tau_1) \hat{E}_S^\dagger(\boldsymbol{\rho}_2, \tau_2) \hat{E}'_R(\boldsymbol{\rho}_1, \tau_1) \hat{E}'_S(\boldsymbol{\rho}_3, \tau_2) \rangle \langle T^*(\boldsymbol{\rho}_2) T(\boldsymbol{\rho}_3) \rangle,\end{aligned}$$

once again leaving us needing to evaluate the fourth order field moment after L -meters of propagation, as well as the second order target-surface moment. The target moment is treated in the same manner as it was for classical illumination, and is thus evaluated with Eq (2.5). Since our fields are normally ordered, and we have Gaussian-state light, we apply the Gaussian-moment factoring theorem to arrive at

$$\begin{aligned}\langle \hat{E}_R^\dagger(\boldsymbol{\rho}_1, \tau_1) \hat{E}_T^\dagger(\boldsymbol{\rho}', \tau_2) \hat{E}'_R(\boldsymbol{\rho}_1, \tau_1) \hat{E}'_T(\boldsymbol{\rho}', \tau_2) \rangle \\ = \frac{A_2}{L^2} \int d\boldsymbol{\rho}_2 \mathcal{T}(\boldsymbol{\rho}_2) \left[\langle |\hat{E}'_R(\boldsymbol{\rho}_1, \tau_1)|^2 \rangle \langle |\hat{E}'_S(\boldsymbol{\rho}_2, \tau_2)|^2 \rangle + |\langle \hat{E}'_R(\boldsymbol{\rho}_1, \tau_1) \hat{E}'_S(\boldsymbol{\rho}_2, \tau_2) \rangle|^2 \right],\end{aligned}$$

which is similar to the form we found for pseudothermal light, except that we have a phase-sensitive cross correlation in lieu of a phase-insensitive cross correlation. To finish the eval-

uation, we need to propagate the phase-sensitive cross correlation and phase-insensitive autocorrelation L meters as follows:

$$\begin{aligned} \langle \hat{E}'_R(\boldsymbol{\rho}_1, t_1) \hat{E}'_S(\boldsymbol{\rho}_2, t_2) \rangle &= \left(\frac{2P}{\pi a_L^2} \right) e^{\frac{ik}{2L} |\boldsymbol{\rho}_1|^2} e^{\frac{ik}{2L} |\boldsymbol{\rho}_2|^2} e^{-|\boldsymbol{\rho}_1 + \boldsymbol{\rho}_2|^2 / 2\rho_L^2} \\ &\times \left[e^{-(|\boldsymbol{\rho}_1|^2 + |\boldsymbol{\rho}_2|^2) / a_0^2} e^{-(t_2 - t_1)^2 / 2T_0^2} + \frac{i}{2} \left(\frac{2}{\pi} \right)^{\frac{1}{4}} \sqrt{\frac{a_L^2}{PT\rho_L^2}} e^{-(|\boldsymbol{\rho}_1|^2 + |\boldsymbol{\rho}_2|^2) / 2a_0^2} e^{-(t_2 - t_1)^2 / T_0^2} \right], \end{aligned} \quad (3.9)$$

and

$$\langle \hat{E}'_m(\boldsymbol{\rho}_1, t_1) \hat{E}'_m(\boldsymbol{\rho}_2, t_2) \rangle = \frac{2P}{\pi a_L^2} e^{\frac{ik_0}{2L} (|\boldsymbol{\rho}_2|^2 - |\boldsymbol{\rho}_1|^2)} e^{-(|\boldsymbol{\rho}_1|^2 + |\boldsymbol{\rho}_2|^2) / a_L^2 - |\boldsymbol{\rho}_1 - \boldsymbol{\rho}_2|^2 / 2\rho_L^2} e^{-(t_2 - t_1)^2 / 2T_0^2}, \quad (3.10)$$

for $m = R, S$. We can now evaluate the ensemble average of the correlation function, once again assuming that the on-target average illumination pattern is wide enough that it is essentially uniform across the target. With that, we find that the mean of the correlation becomes

$$\langle C(\boldsymbol{\rho}_1) \rangle = \frac{q^2 \eta^2 A_1 A_2}{L^2} \left(\frac{2P}{\pi a_L^2} \right)^2 \int d\boldsymbol{\rho}_2 \mathcal{T}(\boldsymbol{\rho}_2) \left[1 + e^{-|\boldsymbol{\rho}_1 + \boldsymbol{\rho}_2|^2 / \rho_L^2} \left(\frac{1}{2\sqrt{2\pi\mathcal{I}}} + 1 \right) \right] \quad (3.11)$$

where once again $\mathcal{I} = PT_0 \rho_L^2 / a_L^2$. As was done in Chapter 2, this can be broken into the background term

$$C_0 = \frac{q^2 \eta^2 A_1 A_2}{L^2} \left(\frac{2P}{\pi a_L^2} \right)^2 \int d\boldsymbol{\rho}_2 \mathcal{T}(\boldsymbol{\rho}_2), \quad (3.12)$$

and the image-bearing term

$$C_1(\boldsymbol{\rho}_1) = \frac{q^2 \eta^2 A_1 A_2}{L^2} \left(\frac{2P}{\pi a_L^2} \right)^2 \int d\boldsymbol{\rho}_2 \mathcal{T}(\boldsymbol{\rho}_2) e^{-|\boldsymbol{\rho}_1 + \boldsymbol{\rho}_2|^2 / \rho_L^2} \left(\frac{1}{2\sqrt{2\pi\mathcal{I}}} + 1 \right). \quad (3.13)$$

Resolution Comparing this to our results from pseudothermal illumination, we see that the image is blurred by the same PSF, except that the coordinates are inverted ($\boldsymbol{\rho}_1 \rightarrow -\boldsymbol{\rho}_1$). Thus, the image has the same resolution of $\rho_L = \lambda_0 L / \pi a_0$.

Contrast Comparing Eq (3.12) to Eq (2.14), we see that phase-sensitive and phase-insensitive imaging have the same background term. Comparing Eq (3.13) to (2.15), we see that the image-bearing terms differ; this is due to our inclusion of non-classical correlations effects. If we look at the high-brightness case, the classical correlation dominates the non-classical correlation, and the image-bearing term for classical phase-sensitive imaging is the same as the image-bearing term for phase-insensitive imaging (except for the coordinate inversion).

To evaluate at the contrast we will use Eq (2.16), the definition we used for the phase-insensitive imaging. Using the simplifying assumption that the PSF is narrow enough to resolve all target-features, and that $\max_{\mathcal{R}}[\mathcal{T}(\boldsymbol{\rho}_1)] = 1$ and $\min_{\mathcal{R}}[\mathcal{T}(\boldsymbol{\rho}_1)] = 0$, we can say

$$\int d\boldsymbol{\rho}_2 \mathcal{T}(\boldsymbol{\rho}_2) e^{-|\boldsymbol{\rho}_1 + \boldsymbol{\rho}_2|^2 / \rho_L^2} \approx \pi \rho_L^2 \mathcal{T}(-\boldsymbol{\rho}_1), \quad (3.14)$$

and simplify our contrast definition to

$$\mathcal{C} \approx \frac{\pi \rho_L^2}{A_T} \left(\frac{1}{2\sqrt{2\pi\mathcal{I}}} + 1 \right), \quad (3.15)$$

where once again $A_T = \int d\boldsymbol{\rho}_2 \mathcal{T}(\boldsymbol{\rho}_2)$. In the high-brightness limit, Eq (3.7) approaches a classical phase-sensitive cross correlation and the contrast in Eq (3.15) approaches Eq (2.18), our result from the pseudothermal ghost imager. However, in the low-brightness limit the the quantum correlation dominates, and the contrast in Eq (3.15) grows without bound. This is the same behavior seen in transmissive biphoton imaging [1, 4]. Thus, maximally correlated phase-sensitive imaging has the same resolution as phase-insensitive imaging, but improved contrast in the low-brightness limit.

3.3 Signal-to-Noise Ratio

The derivation of the SNR for phase-sensitive light will follow what was done in Section 2.3 for the phase-insensitive case. The SNR will be defined as in Eq (2.21) as the ratio of the

squared mean to the variance for the image-bearing portion of the photocurrent correlation, which will now be given by Eq (3.13). We will be implementing a DC-block in the detector response as modeled by Eq (2.19), and will assume that the target features are completely resolved by the imager, allowing us to use the simplification in Eq (3.14). With that, the mean of the image-bearing term becomes

$$C_1(\boldsymbol{\rho}_1) = \frac{q^2 \eta^2 A_1 A_2}{L^2} \left(\frac{2P}{\pi a_L^2} \right)^2 \pi \rho_L^2 \mathcal{T}(-\boldsymbol{\rho}_1) \left(\frac{1}{2\sqrt{2\pi\mathcal{I}}} + 1 \right), \quad (3.16)$$

leaving us needing to evaluate the image-bearing term's second moment

$$\langle \hat{C}^2(\boldsymbol{\rho}_1) \rangle = \frac{1}{T_I^2} \int_{-T_I/2}^{T_I/2} dt \int_{-T_I/2}^{T_I/2} du \langle \hat{i}_1(t) \hat{i}_2(t) \hat{i}_1(u) \hat{i}_2(u) \rangle. \quad (3.17)$$

In evaluating Eq (3.17), we have our first major departure from the derivation in Section 2.3. In Chapter 2 we used a semiclassical treatment of the light, where fluctuations in the measurement were treated as coming from the conversion of the continuous field to discrete charges in the detector, which we called the detector shot noise. However, we are now dealing with quantum-mechanical entangled fields, and must use a full quantum treatment. In quantum optics theory, measurement fluctuations arise from fluctuations of the quantum field, coupled with the type of measurement being performed. Mathematically, these noise terms appear from applying the commutator operations in Eqs (3.1) and (3.2) when normally ordering our higher order field-moments. While the noise qualitatively comes from different sources, quantitatively this has the same effect as the semiclassical treatment: after normally-ordering our fields we have an eighth-order moment, two sixth-order moments, and a fourth-order moment. This comes as no surprise, as it was shown in [4] that ghost-image formation using a downconversion source is inherently a classical phenomenon, with the only non-classical features coming from the stronger-than-classical correlation of signal and idler photons. As before, since these higher-order moments are all normally ordered, and the fields are zero-mean, we can apply the Gaussian-moment factoring theorem to express them as the sum of products of second order moments.

We evaluate the moments at a distance of L -meters from the source, using Eq (3.9) for the phase-sensitive cross correlation and Eq (3.10) for the phase-insensitive autocorrelations. All other second-order moments evaluate to zero. We will again move to the normalized and difference coordinate $\boldsymbol{\nu} = \rho_L k_0(\boldsymbol{\rho}' - \boldsymbol{\rho}'')/L$, where $\boldsymbol{\rho}'$ and $\boldsymbol{\rho}''$ are coordinates at the bucket detector. The definitions of Γ , α , A'_F , and A'_T are the same as in Chapter 2. Finally, assuming that there are at least 10×10 resolution cells in the image and inverting our coordinate system as $\boldsymbol{\rho}_1 \rightarrow -\boldsymbol{\rho}_1$, we have

$$\text{SNR} = \frac{\frac{T_I}{T_0} \mathbb{I}^2}{\frac{A'_T + \frac{a_0^2 A'_F}{4\pi A_2}}{\sqrt{2\pi\rho_L^2} \mathcal{T}(\boldsymbol{\rho}_1)^2} + \frac{T_I}{T_0} \frac{\Gamma\pi a_0^2}{2A_2 \mathcal{T}(\boldsymbol{\rho}_1)^2} \mathbb{I}^2 + \left(\frac{L^2}{A_2 \mathcal{I}\eta \mathcal{T}(\boldsymbol{\rho}_1)} + \frac{\pi\rho_L^2}{A_1 \mathcal{I}\eta} \left[\frac{4}{3} + \frac{a_0^2}{4\pi A_2} \right] + \frac{\sqrt{\pi} L^2 T_0 \Omega_B \rho_L^2}{16\sqrt{2} A_1 A_2 \mathcal{I}^2 \eta^2 \mathcal{T}(\boldsymbol{\rho}_1)} \right) \mathbb{I}}, \quad (3.18)$$

where $\mathbb{I} = \left(\frac{1}{2\sqrt{2\pi}\mathcal{I}} + 1 \right)$. Please see the Appendix for the full derivation. This result is quite unwieldy, so we would like to simplify it by assuming that the receiving aperture is at least as large as the source aperture, giving us

$$\text{SNR} = \frac{\mathcal{T}(\boldsymbol{\rho}_1)^2 \frac{T_I}{T_0} \mathbb{I}^2}{\frac{A'_T}{\sqrt{2\pi\rho_L^2}} + \mathcal{T}^2(\boldsymbol{\rho}_1) \frac{T_I}{T_0} \frac{\Gamma\pi a_0^2}{2A_2} \mathbb{I}^2 + \frac{\mathcal{T}(\boldsymbol{\rho}_1)}{\mathcal{I}\eta} \frac{L^2}{A_2} + \frac{4\pi\rho_L^2 \mathcal{T}^2(\boldsymbol{\rho}_1)}{3A_1 \mathcal{I}\eta} \mathbb{I} + \frac{\mathcal{T}(\boldsymbol{\rho}_1) \sqrt{\pi} T_0 \Omega_B \rho_L^2}{16\sqrt{2} A_1 \mathcal{I}^2 \eta^2} \frac{L^2}{A_2} \mathbb{I}}. \quad (3.19)$$

This result corresponds to the transmissive result calculated in [6], in the same manner as its classical phase-sensitive counterpart in Chapter 2 did; that is, there is now a solid-angle subtense factor on terms associated with the bucket detector, and a target-speckle term in the variance that does not diminish with integration time.

In the classical limit $\mathbb{I} \rightarrow 1$, Eq (3.19) becomes Eq (2.29), and we can see that classically correlated phase-sensitive imaging has the same SNR characteristics as phase-insensitive imaging with pseudothermal light. This means that the high-brightness limit is also the same, and is given by Eq (2.31). Now, in the low-brightness limit the quantum correlation

is significant, $\mathbb{I} \rightarrow \frac{1}{2\sqrt{2\pi\mathcal{I}}}$, and the low-brightness SNR becomes

$$\text{SNR}_L = \frac{T_I}{T_0} \frac{8A_1\eta^2\mathcal{I}}{\pi\Omega_B T_0 \rho_L^2} \mathcal{T}(\rho_1) \frac{A_2}{L^2}. \quad (3.20)$$

This equals the classical low-brightness limit divided by a factor of $2\sqrt{2\pi\mathcal{I}}$, which means that for $\mathcal{I} \ll 1$, the low-brightness SNR is orders of magnitude larger for quantum-correlated light than for classically correlated light. This is the second signature of biphoton state ghost imaging: improved low-brightness SNR.

Chapter 4

Computational Reflective Ghost Imaging

4.1 Theoretical Setup

Ghost imaging requires knowledge of the time-varying speckle pattern illuminating the target. Because the ground-glass diffuser in Fig. 2-1 randomly modulates the source field, we measure the reference field's speckle pattern with the CCD array, and exploit its correlation with the speckle pattern impinging on the target to form the ghost image. Suppose, however, that a known source is subjected to a deterministic spatiotemporal modulation, through use of a spatial light modulator (SLM), in a manner that projects a time-varying but deterministic speckle pattern on the target. In this case the speckle pattern at the target can be computed from diffraction theory, and we do not need the reference arm to form a ghost image [9]. As shown in Fig. 4-1, we form a computational ghost image by cross correlating the computed reference-arm photocurrent,

$$\tilde{i}_1(t) = \int d\tau q\eta \tilde{P}_1(\tau)h(t - \tau), \quad (4.1)$$

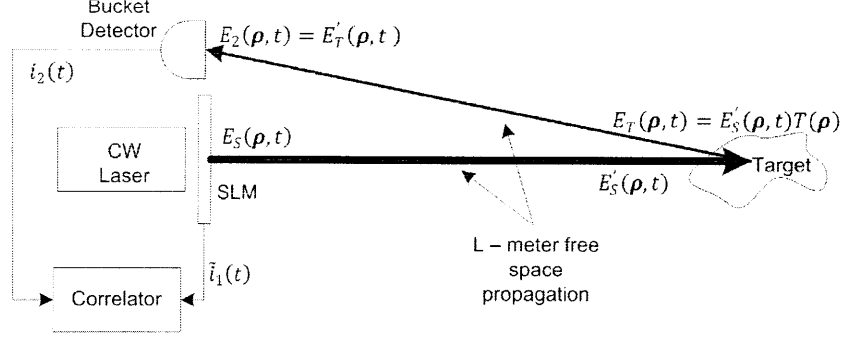


Figure 4-1: Setup for computational reflective ghost imaging.

with the measured photocurrent, $i_2(t)$, from the bucket detector. Here,

$$\tilde{P}_1(t) = A_1 |\tilde{E}_1(\boldsymbol{\rho}_1, t)|^2, \quad (4.2)$$

gives the computed photon flux for a CCD pixel located at $\boldsymbol{\rho}_1$ in terms of the computed speckle pattern $|\tilde{E}_1(\boldsymbol{\rho}_1, t)|^2$.

The SLM is traditionally a square of size $D \times D$, composed of a grid of square pixels of size $d \times d$. Each pixel centered at transverse location $\boldsymbol{\rho}_\ell$ causes a phase shift $\phi_\ell(t)$ on the light impinging it, imparting a spatially-varying phase shift on the resulting field. This means that, assuming the light hitting the SLM can be approximated as a plane-wave, the field leaving the SLM is

$$E(\boldsymbol{\rho}, t) = \sum_{\ell} \text{rect}\left(\frac{x - x_\ell}{d}\right) \text{rect}\left(\frac{y - y_\ell}{d}\right) e^{i\phi_\ell(t)}, \quad (4.3)$$

where $\text{rect}(\cdot)$ is the unit-length rectangle function, $\boldsymbol{\rho} = (x, y)$, and $\boldsymbol{\rho}_\ell = (x_\ell, y_\ell)$ is the center of pixel ℓ . Propagating this into the far field results in

$$E'(\boldsymbol{\rho}', t) = \sum_{\ell} \frac{d^2}{\lambda_0 L} \text{sinc}\left(\frac{x'd}{\lambda_0 L}\right) \text{sinc}\left(\frac{y'd}{\lambda_0 L}\right) e^{-ik_0(x'x_\ell + y'y_\ell)/L} e^{-ik_0(|x'|^2 + |y'|^2)/2L} e^{i\phi_\ell(t)}. \quad (4.4)$$

where $\text{sinc}(\cdot)$ is the sinc function, and $\boldsymbol{\rho}' = (x', y')$.

4.2 Comparison to Pseudothermal Ghost Imager

For comparison with the pseudothermal ghost imager, we would like to derive the spatial resolution, image contrast, and SNR of this computational counterpart. Looking at Eq (4.4), it is not immediately clear how to make the connection to imaging with Gaussian-state light. However, as the field in Eq (4.4) is the sum of a sufficiently large number of weighted independent, identically distributed (IID) random variables, from the Central Limit Theorem it will have Gaussian random process statistics [9]. This can be seen in Fig. 4-2, which shows a pseudorandom phase modulation pattern in (a), and the resulting far-field intensity pattern in (b). Thus, we can treat the far-field pattern $E'_S(\boldsymbol{\rho}, t)$ hitting the target and the reference field $\tilde{E}_1(\boldsymbol{\rho}_1, t) = E'_R(\boldsymbol{\rho}, t)$ — now calculated from the phase shifts by Eq (4.4) — as zero-mean, complex-valued Gaussian random processes. Furthermore, to simplify our analysis, we shall assume that we can use the Gaussian-Schell model for the field correlations as given in Eq (2.10). Under these conditions, the far-field coherence length can be approximated as $\rho_L \approx 2L/k_0D$, and the far-field intensity radius by $a_L \approx 2L/kd$. With these assumptions, all the derivations from Chapter 2 carry over to computational ghost imaging by simple omission of the CCD array's shot noise.

Resolution Under the Gaussian-Schell assumption the spatial resolution of the computational ghost imager is identical to that of the pseudothermal ghost imager at $\rho_L = 2L/k_0d$; therefore, in practice, the resolutions should be similar.

Contrast The computational imager has the same image contrast as pseudothermal ghost imaging for DC-coupled operation, found in Eq (2.18). Moreover, AC-coupling of the bucket detector's photocurrent or the CCD array's computed photocurrent will eliminate the featureless background term in the photocurrent cross correlation, giving the computational ghost imager the same high-contrast behavior seen earlier for AC-coupling in pseudothermal ghost imaging.

Signal-to-noise ratio There is an interesting difference between computational and pseudothermal ghost imaging that appears when we compare their SNR formulas. Since the reference arm is computed, there are no shot noise fluctuations on the current $\tilde{i}_1(t)$ associated with our high-spatial resolution reference arm, and the computational ghost image's SNR is given by

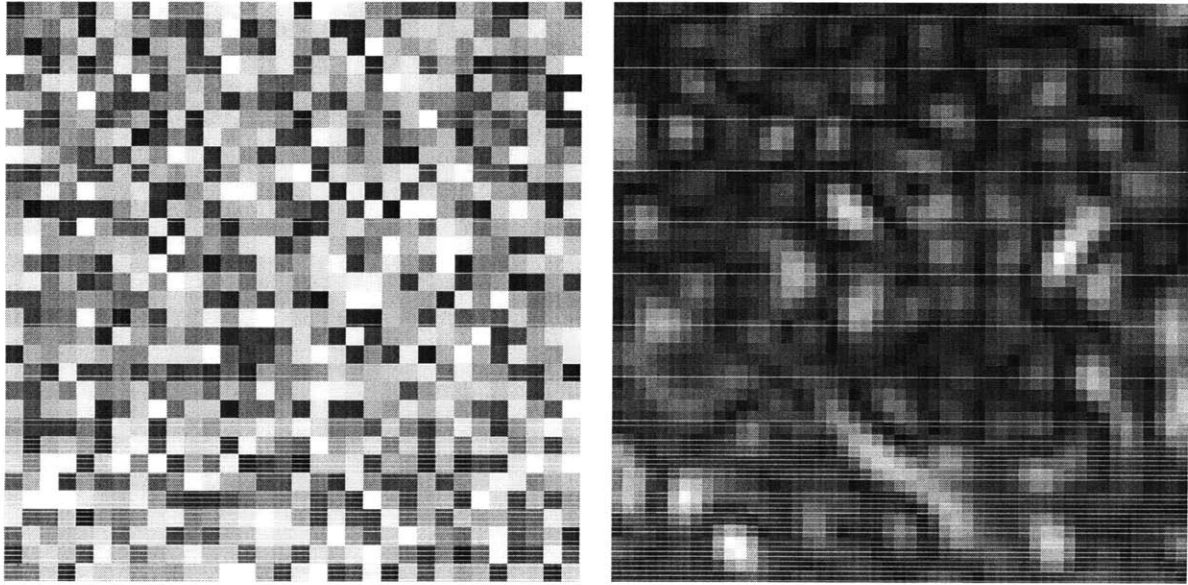
$$\text{SNR}_{\text{comp}} = \frac{\mathcal{T}^2(\rho_1) \frac{T_I}{T_0}}{\frac{A'_T}{\sqrt{2\pi\rho_L^2}} + \mathcal{T}^2(\rho_1) \frac{T_I}{T_0} \frac{\Gamma\pi a_0^2}{2A_2} + \frac{\mathcal{T}(\rho_1)}{\eta\mathcal{L}} \frac{L^2}{A_2}}. \quad (4.5)$$

Comparing this formula with the pseudothermal result from Eq (2.29) we see that the noise denominator for the computational ghost image's SNR contains, from left to right, terms that represent: the noise from the speckle pattern cast on the target; the noise from the speckle on the bucket detector arising from the target's surface roughness; and the beat noise between the computed field speckle on each pixel and the bucket detector's shot noise. It follows that the high-brightness SNR asymptote for computational ghost imaging is identical to that for pseudothermal ghost imaging, as it is limited by the source and target-induced speckle. However, the computational ghost image's SNR enjoys a considerable advantage at low source brightness, viz., its low-brightness asymptote of

$$\text{SNR}_{\text{comp. } L} = \mathcal{T}(\rho_1) \frac{T_I}{T_0} \eta\mathcal{L} \frac{A_2}{L^2}, \quad (4.6)$$

which is significantly higher than that for the pseudothermal ghost imager because it scales linearly, rather than quadratically, with source brightness.

Interestingly, the computational low-brightness limit also compares favorably to the non-classical limit in Eq (3.20). Both scale linearly with the brightness, but given our receiver bandwidth and pixel size assumptions of $\Omega_B T_0 \gg 1$ and $A_1 \ll \rho_L^2$, the SNR for computational imaging in the low-brightness limit is orders of magnitude larger than the corresponding low-brightness (biphoton) limit for non-classical ghost imaging.



(a) The pseudorandom phase modulations applied to the pixels of the SLM. The phases at each pixel are IID uniform random variables on 0 to 2π , with a new realization at each time epoch.

(b) The far-field intensity pattern cast by the SLM. The field distribution closely mimics that of a Gaussian random process, with the coherence length being inversely proportional to the extent of the SLM, and the intensity radius inversely proportional to the width of each pixel

Figure 4-2: One realization of a pseudorandom phase pattern cast on an SLM and resulting calculated far-field intensity pattern.

Chapter 5

Comparison to a Laser Radar System

5.1 Theoretical Setup

The importance of ghost imaging for stand-off sensing rests on it offering some advantage over a comparable laser radar system for the same application. We will use the results from Chapters 2, 3, and 4 to provide a preliminary comparison between ghost imaging and laser radar for stand-off sensing. The laser radar system we shall consider is shown in Fig. 5-1. It is a direct-detection system in which a cw laser beam is used to produce a spatially coherent beam at range L -m whose deterministic intensity pattern matches—in both photon flux and intensity radius—the average intensity pattern of the Gaussian-Schell model we employed for the ghost imager. A fraction of the laser light reflected by the target is focused onto a CCD array by a lens that is co-located with the laser transmitter. A target image is then formed by T_I -s time averaging of the output currents from each CCD pixel. The entrance pupil for the laser radar's receiving lens will be taken to coincide with the bucket detector's \mathcal{A}_2 active region in the ghost imager, and we will assume shot-noise limited CCD operation as was the case for the Fig. 2-1 setup.⁶

⁶We recognize that most laser radar systems employ pulsed sources. We have chosen the cw case to put the laser radar on the most equal footing with the ghost imager for a baseline comparison between their spatial resolutions, image contrasts, and signal-to-noise ratios.

The laser radar image for the CCD pixel at location $\boldsymbol{\rho}_1$ is

$$I(\boldsymbol{\rho}_1) = \frac{1}{T_1} \int_{-T_1/2}^{T_1/2} dt i_3(t), \quad (5.1)$$

where $i_3(t)$ is the photocurrent from that pixel. This photocurrent will have the same structure as seen in Eq (2.2) for ghost imaging, i.e., it will consist of a term driven by the photon flux $P_3(t)$ illuminating the pixel in question plus the shot noise from that pixel. We shall assume the DC-coupled photodetector model from Eq (2.11), and we will assume the pixels are small enough that they do not limit the laser radar's spatial resolution. Once again we shall assume 1:1 imaging, although the actual system will cast a minified image on the CCD, and we shall invert the image plane coordinates so as to obtain an erect image of the target. With these assumptions standard Fourier-optics thin lens theory leads to the following expression for $E_3(\boldsymbol{\rho}_1, t)$, the field illuminating the CCD pixel at $\boldsymbol{\rho}_1$:

$$E_3(\boldsymbol{\rho}_1, t) = \int d\boldsymbol{\rho} T(\boldsymbol{\rho}) e^{ik_0|\boldsymbol{\rho}|^2/2L} \sqrt{\frac{2P}{\pi a_L^2}} e^{-|\boldsymbol{\rho}|^2/a_L^2} \frac{A_2}{\lambda_0^2 L^2} \frac{J_1(\pi D_2 |\boldsymbol{\rho} - \boldsymbol{\rho}_1| / \lambda_0 L)}{\pi D_2 |\boldsymbol{\rho} - \boldsymbol{\rho}_1| / 2\lambda_0 L}, \quad (5.2)$$

where D_2 is the diameter of \mathcal{A}_2 , J_1 is the first-order Bessel function of the first kind, and we have suppressed absolute and quadratic phase factors that do not contribute to $|E_3(\boldsymbol{\rho}_1, t)|^2$. The photon flux for the pixel at $\boldsymbol{\rho}_1$ is thus $P_3(t) = A_1 |E_3(\boldsymbol{\rho}_1, t)|^2$, and the photocurrent $i_3(t)$ is

$$i_3(t) = q\eta P_3(t) + \Delta i_3(t), \quad (5.3)$$

where the second term is the shot noise. Since the source is not fluctuating the detector response will not have a noticeable effect on the photocurrent, and has been omitted. In keeping with what we did for ghost imaging, we shall assume that the target is uniformly illuminated by the laser radar, so that we can use $e^{-|\boldsymbol{\rho}|^2/a_L^2} \approx 1$ in Eq (5.2).

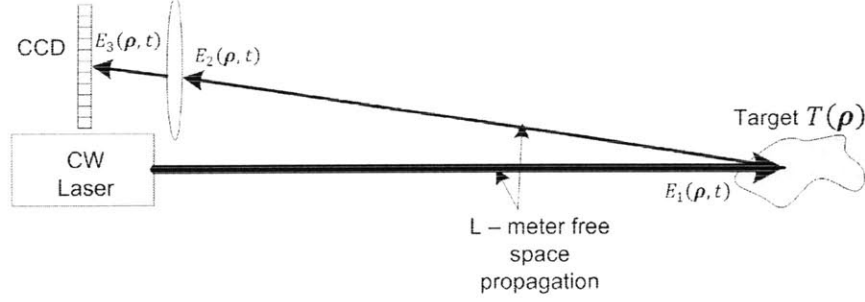


Figure 5-1: Setup for direct-detection laser radar.

5.2 Spatial Resolution and Image Contrast

To derive the laser radar's spatial resolution and image contrast, we once again look at the ensemble-averaged image. Averaging Eq (5.1) over the target's surface roughness and the detector's shot noise we find

$$\langle I(\boldsymbol{\rho}_1) \rangle = \frac{q\eta A_1 A_2^2}{\lambda_0^2 L^4} \frac{2P}{\pi a_L^2} \int d\boldsymbol{\rho} \mathcal{T}(\boldsymbol{\rho}) \left(\frac{J_1(\pi D_2 |\boldsymbol{\rho} - \boldsymbol{\rho}_1| / \lambda_0 L)}{\pi D_2 |\boldsymbol{\rho} - \boldsymbol{\rho}_1| / 2\lambda_0 L} \right)^2, \quad (5.4)$$

which shows that the target image is proportional to the target's intensity-reflection coefficient convolved with the familiar Airy disk PSF for incoherent imaging.

Resolution Our laser radar has a spatial resolution given by $1.22\lambda_0 L / D_2$. In our ghost imaging setup, with $D_2 = 2a_0$, the spatial resolution is given by $\rho_L = \lambda_0 L / \pi a_0 = 2\lambda_0 L / \pi D_2$, which is comparable to that of the laser radar.

Contrast Equation (5.4) also shows that our direct-detection laser radar's image is not embedded in a featureless background, making its image contrast superior to that of DC-coupled pseudothermal ghost imaging but equivalent to that of the AC-coupled version.

5.3 Signal-to-Noise Ratio

We define the laser radar's SNR by

$$\text{SNR} = \frac{\langle I(\boldsymbol{\rho}_1) \rangle^2}{\text{Var}[I(\boldsymbol{\rho}_1)]} = \frac{\langle I(\boldsymbol{\rho}_1) \rangle^2}{\langle I^2(\boldsymbol{\rho}_1) \rangle - \langle I(\boldsymbol{\rho}_1) \rangle^2}, \quad (5.5)$$

to enable a direct comparison with the ghost imaging SNR from Eq (2.21). We will assume that the Airy disk PSF resolves all significant features in the target's intensity-reflection coefficient, yielding

$$\langle I(\boldsymbol{\rho}_1) \rangle = \frac{q\eta A_1 A_2}{L^2} \frac{2P}{\pi a_L^2} \mathcal{T}(\boldsymbol{\rho}_1). \quad (5.6)$$

The variance calculation we need is much simpler than what we performed for ghost imaging. Making use of the iterated-expectation formula,

$$\begin{aligned} \text{Var}[I(\boldsymbol{\rho}_1)] &= E_{\{P_3(t): -T_I/2 \leq t \leq T_I/2\}}[\text{Var}(I(\boldsymbol{\rho}_1) \mid \{P_3(t) : -T_I/2 \leq t \leq T_I/2\})] \\ &+ \text{Var}_{\{P_3(t): -T_I/2 \leq t \leq T_I/2\}}[E(I(\boldsymbol{\rho}_1) \mid \{P_3(t) : -T_I/2 \leq t \leq T_I/2\})], \end{aligned} \quad (5.7)$$

we can easily evaluate the noise denominator in Eq (5.5). The first term on the right in Eq (5.7) is due to the target-induced speckle, and is given by $\langle I(\boldsymbol{\rho}_1) \rangle^2$, and the second term on the right in that equation is due to the shot noise, and is given by $q\langle I(\boldsymbol{\rho}_1) \rangle/T_I$. This leaves us with

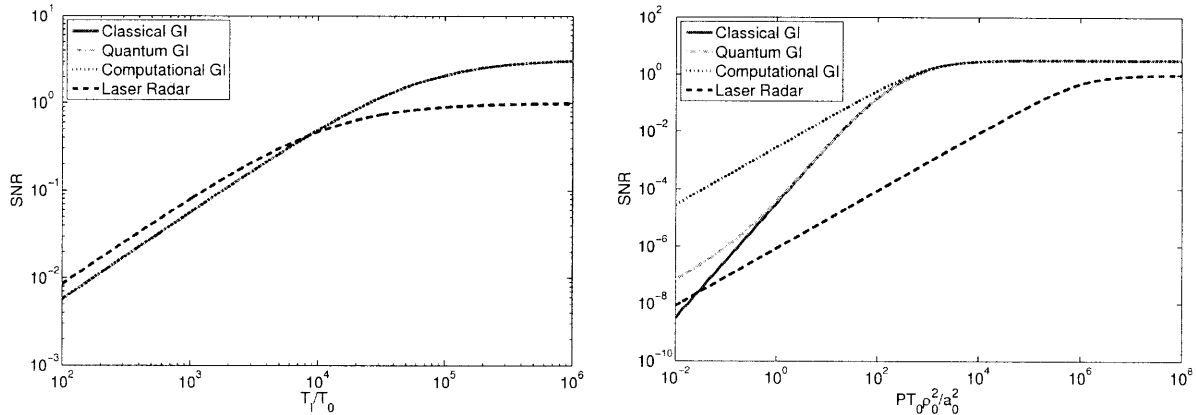
$$\text{SNR} = \frac{\mathcal{T}(\boldsymbol{\rho}_1)}{\mathcal{T}(\boldsymbol{\rho}_1) + \frac{L^2}{\eta A_1 A_2} \frac{\pi a_L^2}{2PT_I}}. \quad (5.8)$$

From this SNR expression we immediately see that when both the source brightness and integration time are sufficiently high, the laser radar's SNR saturates at a maximum value of unity, limited by the target-induced speckle. With the small CCD pixels we have assumed, ghost imaging still experiences a spatial averaging of the target speckle on the bucket detector, whereas no such effect is available for the laser radar system. Thus the laser radar's performance is inferior to that of the ghost imager when both systems have target-speckle limited SNRs. Outside of this limiting scenario, the relationship between the

two systems' SNRs is more complicated, as we will now show.

To compare the stand-off sensing SNRs for ghost imaging and direct-detection laser radar in more detail, consider the plots shown in Figs. 5-2(a) and 5-2(b). Both figures assume $\lambda_0 = 1.5 \mu\text{m}$ operation for ghost imaging and laser radar, with their transmitters having the same photon flux. For ghost imaging we assume the source parameters are $a_0 = 1 \text{ cm}$ and $\rho_0 = 0.15/\pi \text{ mm}$. The target is assumed to be at $L = 1 \text{ km}$ range, with effective area $A'_T = 100 \text{ m}^2$. Thus $a_L = \lambda_0 L / \pi \rho_0 = 10 \text{ m}$ implies that the target illumination is nearly uniform on average, with speckle-limited spatial resolution given by $\rho_L = \lambda_0 L / \pi a_0 = 0.15/\pi \text{ m}$. The CCD array's pixel area will be taken to satisfy $A_1 = 0.1\rho_L^2$, and the bucket detector's area will be set to $A_2 = \pi a_0^2$. Both detectors will have $\eta = 0.9$ quantum efficiency with bandwidths obeying $\Omega_B T_0 = 100$. The laser radar's transmitter will produce a spatially coherent Gaussian intensity pattern on the target with the same a_L value, and its CCD array will be identical to that of the ghost imager. We are interested in the SNR behavior of our systems as a function of source brightness and detector integration time; specifically, we look at the detector integration-time dependence of the SNRs for a strong source, and the SNR source-strength dependence for a long integration time.

Figure 5-2(a) plots the SNRs for pseudothermal ghost imaging, non-classical SPDC ghost imaging, computational ghost imaging, and direct-detection laser radar versus the normalized integration time, T_I/T_0 , when $\mathcal{T}(\rho_1) = 1$ and the transmitter's source brightness is $\mathcal{I} = 10^9$ photons/mode. All three ghost-imaging systems show the same high-brightness behavior, and we see a slight SNR advantage for laser radar operation when $T_I/T_0 < 10^4$, with the ghost imagers offering higher SNRs when all three systems approach their target-speckle limits. Figure 5-2(b) plots the four systems' SNRs versus the source brightness, assuming $\mathcal{T}(\rho_1) = 1$ and $T_I/T_0 = 10^7$. Here we see that computational ghost imaging provides the best performance, while laser radar operation is the worst performer except for $\mathcal{I} \sim 10^{-2}$. Pseudothermal ghost imaging is outperformed by computational operation until both systems' SNRs reach their common target-speckle limit. At very low brightnesses, the SPDC imager trails only the computational imager, but its performance quickly converges with that



(a) Signal-to-noise ratios versus normalized integration time, T_I/T_0 , for high source brightness $\mathcal{I} = \mathcal{I} = PT_0\rho_0^2/a_0^2$, for long integration-time operation $PT_0\rho_0^2/a_0^2 = 10^9$. (b) Signal-to-noise ratios versus source brightness, $PT_0\rho_0^2/a_0^2$, for long integration-time operation $T_I/T_0 = 10^7$.

Figure 5-2: Signal-to-noise ratio comparison between pseudothermal ghost imaging, computational ghost imaging, and laser radar operation. The parameter values assumed are given in the text.

of the pseudothermal imager.

Thus, for very low-brightness illumination, the SNRs are ordered from best to worst as follows: computational ghost imager, SPDC ghost imager, laser radar, and pseudothermal ghost imager. However, it should be noted the the SNRs in this range are of the order 10^{-8} , which provides little usable information. Once the brightness has increased to the point where we can retrieve some image information, the SNRs are clearly arranged from best to worst: computational ghost imager, SPDC and pseudothermal ghost imagers (which have converged), and the laser radar. It thus is reasonable to say that, for the systems we have compared, that computational ghost imaging has the best SNR behavior, followed by SPDC and pseudothermal ghost imaging, with the laser radar at the back. However, for short integration times and a very high-brightness source, there is an advantage to the laser-radar system. This is similar to the behavior seen in pulsed laser-radar systems, indicating that for a definitive comparison between ghost imaging and laser radars, we should include comparisons to a pulsed laser radar systems.

Chapter 6

Evaluation of Turbulence Effects

6.1 Turbulence Review

Our analysis in the preceding chapters had assumed all light fields were propagating through free space; that is, we have not taken into account any effects the propagation medium might have on real-world experiments. In many stand-off sensing applications the fields will be propagating through the atmosphere. The earth's atmosphere is comprised of a variety of gases and entrained particulates, causing wavelength-dependent absorption and Rayleigh scattering [17]. These effects will cause attenuation, but that can be minimized with an appropriate choice of the operating wavelength. The most deleterious atmospheric effects arise from propagating in bad weather, i.e., though fog or clouds [17]. Here the scattering is so severe that neither laser radar nor ghost imaging can be expected to provide useful standoff imaging. However, even in clear weather, the atmosphere is in constant flux. This random mixing of the air parcels with $\sim 1K$ temperature fluctuations create random spatiotemporal variations in the refractive index known as atmospheric turbulence [17]. For a real world analysis, the turbulence-induced effects on the resolution of a remote-sensing system must be explored. Initial work has been done to explore turbulence for transmissive ghost imaging with classical pseudothermal light in [11]; our results will be for reflective imaging with classical and non-classical sources, computational imaging, and also provide a comparison

to laser radar systems.

To start, we shall consider operation in good weather, at a wavelength for which absorption and scattering effects are minimal. In such scenarios, atmospheric turbulence yields refractive index changes on the order of 10^{-6} [17]. While these changes might seem small, their effect on light propagating over a long distance is profound. For instances, two in-phase fields at $\lambda = 1.5 \mu\text{m}$ propagating through media with a refractive index difference of just 10^{-6} will be out π -rad of phase in just .75 m. For propagations over several kilometers, with refractive index variations in both time and space, the accumulated phase distortions will be significant. Moreover, because these phase changes are spatially varying, constructive and destructive interference occurs, i.e., initial phase fluctuations lead to intensity fluctuations known as scintillation [18].

For our analysis we will be using the Kolmogorov model for turbulence. Kolmogorov said that for turbulence that caused the spatial variations of the refractive index to occur on distance scales between a maximum $L_0 \simeq 10 - 100 \text{ m}$ and a minimum $\ell_0 \simeq 10^{-3} \text{ m}$, the temperature fluctuation spatial-structure function followed a two-thirds power law [19]. That is, the second moment of the temperature difference between two points is proportional to two-thirds the distance between the points as

$$\begin{aligned} D_{TT}(\boldsymbol{\rho}) &= \langle (T(\boldsymbol{\rho}_0 + \boldsymbol{\rho}) - T(\boldsymbol{\rho}_0))^2 \rangle \\ &= C_T^2 |\boldsymbol{\rho}|^{2/3}, \end{aligned} \tag{6.1}$$

where D_{TT} is the temperature structure function and C_T^2 is the temperature structure constant.

The temporal fluctuations come from two sources: the changing of the shape of the refractive index structure as the current eddies mix the air, and the drifting of the structures with the average wind velocity [20]. In normal conditions, the time evolution is dominated by the latter mechanism, and the refractive index structure thus has a typical coherence time of $\tau_c = 10^{-3} - 10^{-2}$ second. This means that on shorter time scales the turbulence can be thought of as frozen.

There has been a lot of work done in analyzing laser beam propagation through turbulence, and for our work we take advantage of the Extended Huygens-Fresnel Principle [17]. This is written as the propagation of a spherical wave, multiplied by some path-dependent complex exponential which encompasses the turbulence-induced amplitude and phase variations for a particular path, defined by its starting and ending coordinates. For $\chi_m(\boldsymbol{\rho}, \boldsymbol{\rho}')$ and $\phi_m(\boldsymbol{\rho}, \boldsymbol{\rho}')$ being the log-amplitude and phase variations from $\boldsymbol{\rho}'$ to $\boldsymbol{\rho}$ on path m , if we suppress the time delay the Extended Huygens-Fresnel Principle becomes

$$E'_m(\boldsymbol{\rho}, t) = \int d\boldsymbol{\rho}' E_m(\boldsymbol{\rho}', t) e^{\chi_m(\boldsymbol{\rho}, \boldsymbol{\rho}') + i\phi_m(\boldsymbol{\rho}, \boldsymbol{\rho}')} \frac{k_0 e^{ik_0(L + |\boldsymbol{\rho} - \boldsymbol{\rho}'|^2/2L)}}{i2\pi L}. \quad (6.2)$$

We can usually take χ_m and ϕ_m to be jointly Gaussian, allowing us to construct a structure function⁷ [20]

$$D_m(\boldsymbol{\rho}, \boldsymbol{\rho}') = \langle (\chi_m(\boldsymbol{\rho}_0 + \boldsymbol{\rho}, \boldsymbol{\rho}'_0 + \boldsymbol{\rho}') - \chi_m(\boldsymbol{\rho}_0, \boldsymbol{\rho}'_0))^2 \rangle + \langle (\phi_m(\boldsymbol{\rho}_0 + \boldsymbol{\rho}, \boldsymbol{\rho}'_0 + \boldsymbol{\rho}') - \phi_m(\boldsymbol{\rho}_0, \boldsymbol{\rho}'_0))^2 \rangle \quad (6.3)$$

which satisfies [17]

$$D_m(\boldsymbol{\rho}, \boldsymbol{\rho}') = 2.91k^2 \int_0^L dz C_{n,m}^2(z) \left(\frac{|\boldsymbol{\rho}z + \boldsymbol{\rho}'(L-z)|}{L} \right)^{5/3} \quad (6.4)$$

for the refractive index structure constant $C_{n,m}^2(z) = 10^{-12}C_T^2(z)$. When considering propagation that is approximately parallel to the earth, it is reasonable to assume that the structure constant is stationary, i.e. $C_{n,m}^2(z) \rightarrow C_{n,m}^2$. Since χ_m and ϕ_m are jointly Gaussian we can define a complex random process

$$\psi_m(\boldsymbol{\rho}, \boldsymbol{\rho}') = \chi_m(\boldsymbol{\rho}, \boldsymbol{\rho}') + i\phi_m(\boldsymbol{\rho}, \boldsymbol{\rho}') \quad (6.5)$$

⁷The Gaussian assumption and its associated structure function are limited in validity to what is known as the weak-perturbation regime. However, a more general derivation will lend greater validity to the correlation function expression, given below in Eq (6.6), that will suffice for our purposes in this chapter.

whose correlation function on path m can be evaluated as

$$\begin{aligned} \langle e^{\psi_m^*(\rho_1, \rho_2) + \psi_m(\rho_3, \rho_4)} \rangle &= \exp(-D(\rho_1 - \rho_3, \rho_2 - \rho_4)/2) \\ &\approx \exp\left(-\frac{|\rho_1 - \rho_3|^2 + (\rho_1 - \rho_3) \cdot (\rho_2 - \rho_4) + |\rho_2 - \rho_4|^2}{2\rho_m^2}\right) \end{aligned} \quad (6.6)$$

where we have used the square-law approximation to the rigorous 5/3-law behavior and

$$\rho_m = (1.09k^2 C_{n,m}^2 L)^{-3/5} \quad \text{for } m = R, S, T, \quad (6.7)$$

is the turbulence coherence length on path m , under the assumption of a constant $C_{n,m}^2$ profile. In what follows, we shall assume that there is sufficient physical separation between the reference, signal, and target-return paths so that their turbulence effects are uncorrelated.

6.2 Classical Source

6.2.1 Resolution analysis

We start by looking at the ghost imaging system that we developed in Chapter 2, which utilized a pseudothermal source and a 50/50 beam splitter to create signal and reference fields with a phase-insensitive cross correlation; we now add statistically uncorrelated turbulence on all three paths. We look at an ensemble average of the correlation of photocurrents produced by each detector, using the same assumptions employed in our resolution analysis in Chapter 2 to arrive at

$$\begin{aligned} \langle C(\rho_1) \rangle &= \langle i_1(t) i_2(t) \rangle \\ &= q^2 \eta^2 A_1 \int d\tau_1 \int d\tau_2 h(t - \tau_1) h(t - \tau_2) \int_{\mathcal{A}_2} d\rho' \langle E_R'^*(\rho_1, \tau_1) E_R'(\rho_1, \tau_1) E_T'^*(\rho', \tau_2) E_T'(\rho', \tau_2) \rangle. \end{aligned}$$

Using Eqs (6.2) and (6.5) to back-propagate $E_T'(\rho', t_2)$ to $E_S'(\rho_2, t_2)$, once again suppressing the time delays, and recognizing the independence of the randomness in the target surface,

field speckle, and turbulence, we have

$$\begin{aligned} \langle E_R'^*(\boldsymbol{\rho}_1, \tau_1) E_R'(\boldsymbol{\rho}_1, \tau_1) E_T'^*(\boldsymbol{\rho}', \tau_2) E_T'(\boldsymbol{\rho}', \tau_2) \rangle &= \frac{k_0^2}{4\pi^2 L^2} \int d\boldsymbol{\rho}_2 \int d\boldsymbol{\rho}_3 e^{-ik_0(|\boldsymbol{\rho}' - \boldsymbol{\rho}_2|^2 + |\boldsymbol{\rho}' - \boldsymbol{\rho}_3|^2)/2L} \\ &\times \langle e^{\psi_T^*(\boldsymbol{\rho}', \boldsymbol{\rho}_2)} e^{\psi_T(\boldsymbol{\rho}', \boldsymbol{\rho}_3)} \rangle \langle E_R'^*(\boldsymbol{\rho}_1, \tau_1) E_R'(\boldsymbol{\rho}_1, \tau_1) E_S'^*(\boldsymbol{\rho}_2, \tau_2) E_S'(\boldsymbol{\rho}_3, \tau_2) \rangle \langle T^*(\boldsymbol{\rho}_2) T(\boldsymbol{\rho}_3) \rangle. \end{aligned}$$

Using Eq (2.5) to evaluate the surface moment, this simplifies to to

$$\begin{aligned} &\langle E_R'^*(\boldsymbol{\rho}_1, \tau_1) E_T'^*(\boldsymbol{\rho}', \tau_2) E_R'(\boldsymbol{\rho}_1, \tau_1) E_T'(\boldsymbol{\rho}', \tau_2) \rangle \\ &= \frac{1}{L^2} \int d\boldsymbol{\rho}_2 \mathcal{T}(\boldsymbol{\rho}_2) \langle E_R'^*(\boldsymbol{\rho}_1, \tau_1) E_S'^*(\boldsymbol{\rho}_2, \tau_2) E_R'(\boldsymbol{\rho}_1, \tau_1) E_S'(\boldsymbol{\rho}_2, \tau_2) \rangle \end{aligned}$$

Interestingly, since $\langle e^{\psi_T^*(\boldsymbol{\rho}', \boldsymbol{\rho}_2) + \psi_T(\boldsymbol{\rho}', \boldsymbol{\rho}_2)} \rangle = 1$, we find that the turbulence on the target-return path does not affect the resolution of the final image.

In our resolution analysis in Chapter 2 we could stop here and use the Gaussian-Schell model to evaluate the fourth-order field moment. However, since we are allowing for turbulence on the signal and reference paths, we have to back propagate these fields to the source, giving us

$$\begin{aligned} \langle E_R'^*(\boldsymbol{\rho}_1, \tau_1) E_S'^*(\boldsymbol{\rho}_2, \tau_2) E_R'(\boldsymbol{\rho}_1, \tau_1) E_S'(\boldsymbol{\rho}_2, \tau_2) \rangle &= \int d\boldsymbol{\rho}'_1 \int d\boldsymbol{\rho}'_2 \int d\boldsymbol{\rho}''_1 \int d\boldsymbol{\rho}''_2 \\ &\langle E_R^*(\boldsymbol{\rho}'_1, \tau_1) e^{\psi_R^*(\boldsymbol{\rho}_1, \boldsymbol{\rho}'_1)} \frac{k_0 e^{-ik_0(L+|\boldsymbol{\rho}_1 - \boldsymbol{\rho}'_1|^2/2L)}}{-i2\pi L} E_S^*(\boldsymbol{\rho}'_2, \tau_2) e^{\psi_S^*(\boldsymbol{\rho}_2, \boldsymbol{\rho}'_2)} \frac{k_0 e^{-ik_0(L+|\boldsymbol{\rho}_2 - \boldsymbol{\rho}'_2|^2/2L)}}{-i2\pi L} \\ &\times E_R(\boldsymbol{\rho}''_1, \tau_1) e^{\psi_R(\boldsymbol{\rho}_1, \boldsymbol{\rho}''_1)} \frac{k_0 e^{ik_0(L+|\boldsymbol{\rho}_1 - \boldsymbol{\rho}''_1|^2/2L)}}{i2\pi L} E_S(\boldsymbol{\rho}''_2, \tau_2) e^{\psi_S(\boldsymbol{\rho}_2, \boldsymbol{\rho}''_2)} \frac{k_0 e^{ik_0(L+|\boldsymbol{\rho}_2 - \boldsymbol{\rho}''_2|^2/2L)}}{i2\pi L} \rangle. \end{aligned}$$

We can now use Gaussian moment factoring and Eq (2.6) to evaluate the fourth-order field moment, and Eq (6.6) to evaluate the turbulence. Taking into account our DC-block filter

and using the far-field assumption, we have

$$\begin{aligned}
\langle E_R'^*(\boldsymbol{\rho}_1, \tau_1) E_S'^*(\boldsymbol{\rho}_2, \tau_2) E_R'(\boldsymbol{\rho}_1, \tau_1) E_S'(\boldsymbol{\rho}_2, \tau_2) \rangle &= \left(\frac{k_0}{2\pi L} \right)^4 \left(\frac{2P}{\pi a_0^2} \right)^2 \int d\boldsymbol{\rho}'_1 \int d\boldsymbol{\rho}'_2 \int d\boldsymbol{\rho}''_1 \int d\boldsymbol{\rho}''_2 \\
&\times e^{\frac{ik_0}{L} \boldsymbol{\rho}_1 \cdot (\boldsymbol{\rho}'_1 - \boldsymbol{\rho}''_1)} e^{\frac{ik_0}{L} \boldsymbol{\rho}_2 \cdot (\boldsymbol{\rho}'_2 - \boldsymbol{\rho}''_2)} e^{-|\boldsymbol{\rho}'_1 - \boldsymbol{\rho}''_1|^2 / 2\rho_R^2} e^{-|\boldsymbol{\rho}'_2 - \boldsymbol{\rho}''_2|^2 / 2\rho_S^2} e^{-(|\boldsymbol{\rho}'_1|^2 + |\boldsymbol{\rho}'_2|^2 + |\boldsymbol{\rho}''_1|^2 + |\boldsymbol{\rho}''_2|^2) / a_0^2} \\
&\times e^{-|\boldsymbol{\rho}'_1 - \boldsymbol{\rho}''_1|^2 / 2\rho_0^2} e^{-|\boldsymbol{\rho}'_2 - \boldsymbol{\rho}''_2|^2 / 2\rho_0^2} e^{-(\tau_2 - \tau_1)^2 / T_0^2}.
\end{aligned} \tag{6.8}$$

In evaluating Eq (6.8) we will assume that the turbulence coherence length on each path m will stay large enough that $\rho_m \gg \rho_0$, as ρ_0 is typically on the order of a few wavelengths. We will still assume that $a_0 \gg \rho_0$, but we will make no assumption about the relative sizes of a_0 and ρ_m . Under these conditions, we find that

$$\langle C(\boldsymbol{\rho}_1) \rangle = \frac{q^2 \eta^2 A_1 A_2}{L^2} \left(\frac{2P}{\pi a_L^2} \right)^2 \frac{2\rho_R^2 \rho_S^2}{2\rho_R^2 \rho_S^2 + a_0^2 (\rho_R^2 + \rho_S^2)} \int d\boldsymbol{\rho}_2 \mathcal{T}(\boldsymbol{\rho}_2) e^{-\frac{|\boldsymbol{\rho}_1 - \boldsymbol{\rho}_2|^2}{\rho_L^2} \frac{2\rho_R^2 \rho_S^2}{2\rho_R^2 \rho_S^2 + a_0^2 (\rho_R^2 + \rho_S^2)}}. \tag{6.9}$$

Our PSF has now widened, with the resolution transforming as $\rho_L \rightarrow \rho'_L$ for

$$\rho'_L = \rho_L \sqrt{\frac{2\rho_R^2 \rho_S^2 + a_0^2 (\rho_R^2 + \rho_S^2)}{2\rho_R^2 \rho_S^2}}. \tag{6.10}$$

By means of Eq (6.7) ρ'_L can be rewritten purely in terms of source size and structure constants on each path as

$$\rho'_L = \frac{2L}{ka_0} \sqrt{1 + \frac{a_0^2}{2} (1.09k^2 L)^{6/5} \left[(C_{n,S}^2)^{6/5} + (C_{n,R}^2)^{6/5} \right]}. \tag{6.11}$$

It is also worth noting that turbulence on the signal and reference paths have identical impacts on the PSF, and thus identical contributions to resolution degradation.

6.2.2 Special cases

We would now like to look at a few special cases that illustrate most of the turbulence behavior that we are interested in. These are: no turbulence on either path; turbulence on only one path, which corresponds to the computational case; and symmetric turbulence on both paths, which is a good approximation when both paths are going through similar atmosphere.

No Turbulence As the turbulence coherence lengths increase without bound ($\rho_R \rightarrow \infty$, $\rho_S \rightarrow \infty$) the effects of turbulence vanish. In this limit $\rho'_L = \rho_L$, and Eq (6.9) becomes

$$\langle C(\boldsymbol{\rho}_1) \rangle = \frac{q^2 \eta^2 A_1 A_2}{L^2} \left(\frac{2P}{\pi a_L^2} \right)^2 \int d\boldsymbol{\rho}_2 \mathcal{T}(\boldsymbol{\rho}_2) e^{-|\boldsymbol{\rho}_1 - \boldsymbol{\rho}_2|^2 / \rho_L^2}, \quad (6.12)$$

which matches Eq (2.15), our result calculated without turbulence.

Computational Case When doing the computational case the reference arm is calculated, so there is no turbulence to account for on the reference path. Thus we can let $\rho_R \rightarrow \infty$, and we find that

$$\langle C(\boldsymbol{\rho}_1) \rangle = \frac{q^2 \eta^2 A_1 A_2}{L^2} \left(\frac{2P}{\pi a_L^2} \right)^2 \frac{2\rho_S^2}{2\rho_S^2 + a_0^2} \int d\boldsymbol{\rho}_2 \mathcal{T}(\boldsymbol{\rho}_2) e^{-\frac{|\boldsymbol{\rho}_1 - \boldsymbol{\rho}_2|^2}{\rho_L^2} - \frac{2\rho_S^2}{2\rho_S^2 + a_0^2}}. \quad (6.13)$$

By comparing Eqs (6.9) and (6.13), we see that computational and non-computational versions have different PSF's and that the resolution for the computational case is better. That is,

$$\rho_L \sqrt{\frac{2\rho_S^2 + a_0^2}{2\rho_S^2}} < \rho_L \sqrt{\frac{2\rho_R^2 \rho_S^2 + a_0^2 (\rho_R^2 + \rho_S^2)}{2\rho_R^2 \rho_S^2}}. \quad (6.14)$$

It should be noted that while this situation describes the computational case, it is possible to have a non-computational case in which there is only turbulence on one arm. Since the

turbulence on both paths have identical effects, a situation where there is turbulence on only the reference path, and not the signal path, would be described by Eq (6.13) with ρ_R substituted for ρ_S .

Symmetric Case In many situations the signal and reference paths will be going through atmosphere with similar turbulence, and thus approximately the same structure functions and coherence lengths. This lets us say $\rho_R = \rho_S = \rho_t$, and

$$\langle C(\boldsymbol{\rho}_1) \rangle = \frac{q^2 \eta^2 A_1 A_2}{L^2} \left(\frac{2P}{\pi a_L^2} \right)^2 \frac{\rho_t^2}{\rho_t^2 + a_0^2} \int d\boldsymbol{\rho}_2 \mathcal{T}(\boldsymbol{\rho}_2) e^{-\frac{|\boldsymbol{\rho}_1 - \boldsymbol{\rho}_2|^2}{\rho_L^2} - \frac{\rho_t^2}{\rho_t^2 + a_0^2}}. \quad (6.15)$$

6.3 Non-classical Source

Having looked at the effects of turbulence for a classical light source, we once again turn our attention to non-classical sources. We again perform a Gaussian-state analysis, following the resolution derivation in Chapter 3 with turbulence added on all three paths. For propagation through turbulence we will replace Eq (6.2) with its operator equivalent

$$\hat{E}'_m(\boldsymbol{\rho}, t) = \int d\boldsymbol{\rho}' \hat{E}'_m(\boldsymbol{\rho}', t) e^{\psi_m(\boldsymbol{\rho}, \boldsymbol{\rho}')} \frac{k_0 e^{ik_0(L + |\boldsymbol{\rho} - \boldsymbol{\rho}'|^2/2L)}}{i2\pi L}, \quad \text{for } m = S, R, T,$$

where $\hat{E}'_T(\boldsymbol{\rho}, t) = \left[\hat{E}'_S(\boldsymbol{\rho}, t) T(\boldsymbol{\rho}) + \hat{E}'_{vac,S}(\boldsymbol{\rho}, t) \sqrt{1 - |T(\boldsymbol{\rho})|^2} \right]$ and $e^{\psi_m(\boldsymbol{\rho}, \boldsymbol{\rho}')}$ is the same complex random process from Eq (6.5) which encapsulates the effects of turbulence on path m from $\boldsymbol{\rho}'$ to $\boldsymbol{\rho}$. We take the ensemble average of the photocurrents, which after normally ordering the field operators and applying Eq (3.6) becomes

$$\begin{aligned} \langle \hat{C}(\boldsymbol{\rho}_1) \rangle &= \langle \hat{i}_1(t) \hat{i}_2(t) \rangle \\ &= q^2 \eta^2 A_1 \int d\tau_1 \int d\tau_2 h(t - \tau_1) h(t - \tau_2) \int_{\mathcal{A}_2} d\boldsymbol{\rho}' \langle \hat{E}'_R^\dagger(\boldsymbol{\rho}_1, \tau_1) \hat{E}'_T^\dagger(\boldsymbol{\rho}', \tau_2) \hat{E}'_R(\boldsymbol{\rho}_1, \tau_1) \hat{E}'_T(\boldsymbol{\rho}', \tau_2) \rangle. \end{aligned}$$

We back propagate, evaluate the surface moment with Eq (2.5) and the turbulence with Eq (6.6) to get

$$\begin{aligned} & \langle \hat{E}_R^{\prime\dagger}(\boldsymbol{\rho}_1, \tau_1) \hat{E}_T^{\prime\dagger}(\boldsymbol{\rho}', \tau_2) \hat{E}'_R(\boldsymbol{\rho}_1, \tau_1) \hat{E}'_T(\boldsymbol{\rho}', \tau_2) \rangle \\ &= \frac{1}{L^2} \int d\boldsymbol{\rho}_2 \mathcal{T}(\boldsymbol{\rho}_2) \langle \hat{E}_R^{\prime\dagger}(\boldsymbol{\rho}_1, \tau_1) \hat{E}_S^{\prime\dagger}(\boldsymbol{\rho}_2, \tau_2) \hat{E}'_R(\boldsymbol{\rho}_1, \tau_1) \hat{E}'_S(\boldsymbol{\rho}_2, \tau_2) \rangle. \end{aligned} \quad (6.16)$$

Again, we find that there is no effect from the turbulence on the target-return path. Propagating back to the source, evaluating the field and turbulence moments, and implementing the DC-block filter, we arrive at

$$\begin{aligned} & \langle \hat{E}_R^{\prime\dagger}(\boldsymbol{\rho}_1, \tau_1) \hat{E}_S^{\prime\dagger}(\boldsymbol{\rho}_2, \tau_2) \hat{E}'_R(\boldsymbol{\rho}_1, \tau_1) \hat{E}'_S(\boldsymbol{\rho}_2, \tau_2) \rangle = \left(\frac{k_0}{2\pi L} \right)^4 \left(\frac{2P}{\pi a_0^2} \right)^2 \int d\boldsymbol{\rho}'_1 \int d\boldsymbol{\rho}'_2 \int d\boldsymbol{\rho}''_1 \int d\boldsymbol{\rho}''_2 \\ & \times e^{\frac{ik_0}{L} \boldsymbol{\rho}_1 \cdot (\boldsymbol{\rho}'_1 - \boldsymbol{\rho}''_1)} e^{\frac{ik_0}{L} \boldsymbol{\rho}_2 \cdot (\boldsymbol{\rho}'_2 - \boldsymbol{\rho}''_2)} e^{-|\boldsymbol{\rho}'_1 - \boldsymbol{\rho}''_1|^2 / 2\rho_R^2} e^{-|\boldsymbol{\rho}'_2 - \boldsymbol{\rho}''_2|^2 / 2\rho_S^2} e^{-(|\boldsymbol{\rho}'_1|^2 + |\boldsymbol{\rho}''_1|^2 + |\boldsymbol{\rho}'_2|^2 + |\boldsymbol{\rho}''_2|^2) / a_0^2} \\ & \times \left(e^{-|\boldsymbol{\rho}'_2 - \boldsymbol{\rho}'_1|^2 / 2\rho_0^2} e^{-(\tau_2 - \tau_1)^2 / 2T_0^2} - i \left(\frac{2}{\pi} \right)^{\frac{1}{4}} \sqrt{\frac{a_0^2}{PT_0\rho_0^2}} e^{-|\boldsymbol{\rho}'_2 - \boldsymbol{\rho}'_1|^2 / \rho_0^2} e^{-(\tau_2 - \tau_1)^2 / T_0^2} \right) \\ & \times \left(e^{-|\boldsymbol{\rho}''_2 - \boldsymbol{\rho}''_1|^2 / 2\rho_0^2} e^{-(\tau_2 - \tau_1)^2 / 2T_0^2} + i \left(\frac{2}{\pi} \right)^{\frac{1}{4}} \sqrt{\frac{a_0^2}{PT_0\rho_0^2}} e^{-|\boldsymbol{\rho}''_2 - \boldsymbol{\rho}''_1|^2 / \rho_0^2} e^{-(\tau_2 - \tau_1)^2 / T_0^2} \right). \end{aligned} \quad (6.17)$$

Equation (6.17) can be directly evaluated, and we find the photocurrent average to be

$$\begin{aligned} \langle \hat{C}(\boldsymbol{\rho}_1) \rangle &= \frac{q^2 \eta^2 A_1 A_2}{L^2} \left(\frac{2P}{\pi a_L^2} \right)^2 \frac{2\rho_R^2 \rho_S^2}{2\rho_R^2 \rho_S^2 + a_0^2 (\rho_R^2 + \rho_S^2)} \left(1 + \frac{1}{2\sqrt{2\pi\mathcal{I}}} \right) \\ & \times \int d\boldsymbol{\rho}_2 \mathcal{T}(\boldsymbol{\rho}_2) e^{-\frac{|\boldsymbol{\rho}_1 + \boldsymbol{\rho}_2|^2}{\rho_L^2} \frac{2\rho_R^2 \rho_S^2}{2\rho_R^2 \rho_S^2 + a_0^2 (\rho_R^2 + \rho_S^2)}}, \end{aligned} \quad (6.18)$$

where $\mathcal{I} = PT_0\rho_0^2/a_0^2 = PT_0\rho_L^2/a_L^2$ is the brightness term from the SNR derivations. Since we are operating in the far field, there is no resolution gain from the use of entangled signal and reference fields, even in the low-brightness limit in which the Gaussian state becomes the biphoton state. Turbulence causes the same resolution spreading in phase-sensitive ghost imaging as it does in phase-insensitive ghost imaging, regardless of the nature of the correlation (classical or non-classical).

6.4 Laser Radar

Finally, we would like to compare the turbulence-induced degradation suffered by ghost imaging systems to that for a laser radar system under the same atmospheric conditions. We will be using the laser radar system developed in Chapter 5, and start by taking an ensemble average of the image-bearing term in Eq (5.1) to arrive at

$$\langle I(\boldsymbol{\rho}_1) \rangle = q\eta A_1 \langle E_3^*(\boldsymbol{\rho}_1, t) E_3(\boldsymbol{\rho}_1, t) \rangle. \quad (6.19)$$

Propagating back to the lens, we have

$$\begin{aligned} \langle I(\boldsymbol{\rho}_1) \rangle &= q\eta A_1 \int_{\mathcal{A}_2} d\boldsymbol{\rho}' \int_{\mathcal{A}_2} d\boldsymbol{\rho}'' \langle E_2^*(\boldsymbol{\rho}', t) E_2(\boldsymbol{\rho}'', t) \rangle \\ &\times e^{\frac{ik_0}{2L}|\boldsymbol{\rho}'|^2} e^{-\frac{ik_0}{2L}|\boldsymbol{\rho}''|^2} \frac{k_0 e^{-ik_0(L+|\boldsymbol{\rho}_1-\boldsymbol{\rho}'|^2/2L)}}{-i2\pi L} \frac{k_0 e^{ik_0(L+|\boldsymbol{\rho}_1-\boldsymbol{\rho}''|^2/2L)}}{i2\pi L}. \end{aligned} \quad (6.20)$$

We are not considering any turbulence between the lens and the CCD array. For convenience we are using a 1:1 imaging system, but in a realistic implementation the image produced is a minified version of the target. For this system we are considering turbulence on both paths, viz., on the signal path (S), from the source to the target, and the target-return path (T), from the target to the lens. Thus, back propagating to the target we have

$$\begin{aligned} \langle E_2^*(\boldsymbol{\rho}', t) E_2(\boldsymbol{\rho}'', t) \rangle &= \int d\boldsymbol{\rho}_2 \int d\boldsymbol{\rho}_3 \langle e^{\psi_T^*(\boldsymbol{\rho}', \boldsymbol{\rho}_2) + \psi_T(\boldsymbol{\rho}'', \boldsymbol{\rho}_3)} \rangle \langle T^*(\boldsymbol{\rho}_2) T(\boldsymbol{\rho}_3) \rangle \\ &\times \langle E_1^*(\boldsymbol{\rho}_2, t) E_1(\boldsymbol{\rho}_3, t) \rangle \frac{k_0 e^{-ik_0(L+|\boldsymbol{\rho}'-\boldsymbol{\rho}_2|^2/2L)}}{-i2\pi L} \frac{k_0 e^{ik_0(L+|\boldsymbol{\rho}''-\boldsymbol{\rho}_3|^2/2L)}}{i2\pi L}. \end{aligned}$$

Using Eq (2.5) and the far-field assumption this simplifies to

$$\begin{aligned} \langle E_2^*(\boldsymbol{\rho}', t) E_2(\boldsymbol{\rho}'', t) \rangle &= \frac{e^{-\frac{|\boldsymbol{\rho}'' - \boldsymbol{\rho}'|^2}{2\rho_T^2}}}{L^2} \int d\boldsymbol{\rho}_2 \mathcal{T}(\boldsymbol{\rho}_2) \\ &\times \langle E_1^*(\boldsymbol{\rho}_2, t) E_1(\boldsymbol{\rho}_2, t) \rangle e^{-\frac{ik_0}{2L}|\boldsymbol{\rho}'|^2} e^{\frac{ik_0}{2L}|\boldsymbol{\rho}''|^2} e^{\frac{ik_0}{L}\boldsymbol{\rho}' \cdot \boldsymbol{\rho}_2} e^{-\frac{ik_0}{L}\boldsymbol{\rho}'' \cdot \boldsymbol{\rho}_2}, \end{aligned}$$

Now, back-propagating $\langle E_1^*(\boldsymbol{\rho}_2, t) E_1(\boldsymbol{\rho}_2, t) \rangle$, and assuming the far-field condition, we have

$$\begin{aligned} \langle E_1^*(\boldsymbol{\rho}_2, t) E_1(\boldsymbol{\rho}_2, t) \rangle &= \left(\frac{2P}{\pi w_0^2} \right) \int d\boldsymbol{\rho}'_2 \int d\boldsymbol{\rho}''_2 \langle e^{\psi_S^*(\boldsymbol{\rho}_2, \boldsymbol{\rho}'_2) + \psi_S(\boldsymbol{\rho}_2, \boldsymbol{\rho}''_2)} \rangle e^{-\frac{(|\boldsymbol{\rho}'_2|^2 + |\boldsymbol{\rho}''_2|^2)}{w_0^2}} \frac{k_0^2 e^{\frac{ik_0}{L}\boldsymbol{\rho}_2 \cdot (\boldsymbol{\rho}'_2 - \boldsymbol{\rho}''_2)}}{4\pi^2 L^2} \\ &= \left(\frac{1}{1 + \frac{w_0^2}{\rho_S^2}} \right) \frac{2P}{\pi a_L^2} e^{-\frac{2|\boldsymbol{\rho}_2|^2}{a_L^2} - \frac{\rho_S^2}{w_0^2 + \rho_S^2}} \end{aligned}$$

Our laser radar system is constrained, for comparison purposes, to have an on-target average illumination pattern equal to that of the ghost imager. Since the laser is a coherent source, that means that the source beam waist w_0 for this system is approximately the same size as the source coherence length ρ_0 for the ghost imaging system. As such, we can assume that for the laser radar system $w_0 \ll \rho_S$, which let us simplify to

$$\langle E_1^*(\boldsymbol{\rho}_2, t) E_1(\boldsymbol{\rho}_2, t) \rangle = \frac{2P}{\pi a_L^2} e^{-\frac{2|\boldsymbol{\rho}_2|^2}{a_L^2}},$$

indicating that for this system there is no effect on the resolution from turbulence on the signal path.

This lets us rewrite Eq (6.20) as

$$\langle I(\boldsymbol{\rho}_1) \rangle = \frac{q\eta A_1}{\lambda_0^2 L^4} \frac{2P}{\pi a_L^2} \int_{A_2} d\boldsymbol{\rho}' \int_{A_2} d\boldsymbol{\rho}'' \mathbb{T} \left(\frac{k_0}{L}(\boldsymbol{\rho}'' - \boldsymbol{\rho}') \right) e^{-|\boldsymbol{\rho}'' - \boldsymbol{\rho}'|^2 / 2\rho_T^2} e^{-\frac{ik_0}{L}(\boldsymbol{\rho}'' - \boldsymbol{\rho}') \cdot \boldsymbol{\rho}_1}, \quad (6.21)$$

where $\mathbb{T}(\boldsymbol{\xi})$ is again the two-dimensional spatial Fourier transform of $\mathcal{T}(\boldsymbol{\rho})$. We invert the coordinates as $\boldsymbol{\rho}_1 \rightarrow -\boldsymbol{\rho}_1$ so that we have an upright image, and use difference coordinates

to evaluate the integrals over the lenses to arrive at

$$\langle I(\boldsymbol{\rho}_1) \rangle = \frac{q\eta A_1 A_2}{L^2} \frac{2P}{\pi a_L^2} \mathcal{T}(\boldsymbol{\rho}_1) * \frac{\rho_T^2 k_0^2}{2\pi L^2} e^{-|\boldsymbol{\rho}_1|^2 \frac{\rho_T^2 k_0^2}{2L^2}} * \frac{\pi D_2^2}{\lambda_0^2 L^2} \left(\frac{J_1(\pi D_2 |\boldsymbol{\rho}_1| / \lambda_0 L)}{\pi D_2 |\boldsymbol{\rho}_1| / \lambda_0 L} \right)^2. \quad (6.22)$$

To evaluate the spreading due to turbulence we can approximate the Jinc PSF, which has its first zero at $|\boldsymbol{\rho}_1| = 1.22\lambda_0 L / D_2$, as a Gaussian PSF with an e^{-1} point at $|\boldsymbol{\rho}_1| = 2\lambda_0 L / \pi D_2$, i.e.,

$$\frac{\pi D_2^2}{\lambda_0^2 L^2} \left(\frac{J_1(\pi D_2 |\boldsymbol{\rho}_1| / \lambda_0 L)}{\pi D_2 |\boldsymbol{\rho}_1| / \lambda_0 L} \right)^2 \rightarrow \frac{\pi D_2^2}{4\lambda_0^2 L^2} e^{-|\boldsymbol{\rho}_1|^2 \frac{\pi^2 D_2^2}{4\lambda_0^2 L^2}}. \quad (6.23)$$

This lets us simplify Eq (6.22) to

$$\langle I(\boldsymbol{\rho}_1) \rangle = \frac{q\eta A_1 A_2^2}{\lambda_0^2 L^4} \frac{2P}{\pi a_L^2} \frac{2\rho_T^2}{2\rho_T^2 + D^2/4} \int d\boldsymbol{\rho} \mathcal{T}(\boldsymbol{\rho}) e^{-|\boldsymbol{\rho} - \boldsymbol{\rho}_1|^2 \frac{\pi^2 D^2}{4\lambda_0^2 L^2} \frac{2\rho_T^2}{2\rho_T^2 + D^2/4}}. \quad (6.24)$$

We can now say that the effect of turbulence on the resolution is to degrade it by a factor of $\sqrt{\frac{2\rho_T^2 + D^2/4}{2\rho_T^2}}$. For a comparison to the ghost imaging system, we once again say that all lens diameters are of the same size, so that $D = 2a_0$, and our spreading factor becomes $\sqrt{\frac{2\rho_T^2 + a_0^2}{2\rho_T^2}}$. This is the same spreading we found when there was turbulence on one arm of the ghost imaging system, as shown in Eq (6.13). From this we can conclude that ghost imaging systems can be constructed that do not suffer resolution degradation from turbulence worse than the degradation found in a flood-light illumination laser radar system. It should also be noted that for a raster-scanning type laser radar system, which we have not yet considered, the source beam size is significantly larger than for the flood-light system, and therefore the turbulence on the signal path will no longer be insignificant. Indeed, partially coherent beams, such as our pseudothermal source, have been shown to be less affected by turbulence than similar fully coherent beams [21, 22], indicating that ghost imaging might have an advantage in comparison to a raster-scanning laser radar. We also might expect that the effects of turbulence on the SNR of ghost imaging and laser radar systems could be different, but we have not explored this issue.

Chapter 7

Improving Ghost Image Quality

So far we have analyzed reflective ghost imaging for classical and non-classical sources, as well as for a computed reference beam. These results were compared to a laser radar system; ghost imaging has a somewhat advantageous asymptotic SNR behavior for high-brightness illumination and long capture times, as well as improved low-brightness behavior when there is a non-classical correlation between the fields, and when a computed reference arm is employed. However, the SNR is still limited by the speckled nature of the return patterns cast by the rough surface of the target. In this chapter we propose three methods to improve the image quality, focusing on reducing the target-speckle imposed SNR limit.

First, we propose a detection scheme in which multiple bucket detectors are employed, each capturing the returned light at different transverse locations within the same plane, as detailed in Fig. 7-1. The target-speckle attributes of the returning field decorrelate with transverse location, so each detector should see different speckle behavior, allowing us to average it out and improve the asymptotic SNR. This same target-speckle averaging could also be accomplished by the use of multiple wavelength illumination, as shown in Fig. 7-4. If we use several narrow-band sources sufficiently far apart in wavelength, the return patterns from each source will have uncorrelated speckle statistics at the same transverse location, allowing us average out the speckle effects. Finally, each bucket detector measurement in a ghost imaging setup can be thought of as a random projection of the target reflection

pattern. Since we know the pattern being cast on the target, compressive sensing methods can be applied to the bucket detector measurements to achieve a high-quality image quickly. This connection has already been made, and experimentally verified, in [12] for transmissive ghost imaging. In reflective-imaging we have the added complication of the target-speckle, but we will demonstrate that a connection can still be made back to the idea of projective measurements, enabling the use of compressive sensing techniques.

7.1 Multiple Bucket Detectors

For this setup we consider n co-planar bucket detectors in some arbitrary setup. The correlation function at each transverse location $\boldsymbol{\rho}_1$ is taken to be the average of the correlation function for the CCD pixel at $\boldsymbol{\rho}_1$ and each bucket detector. The output photocurrent of a CCD pixel will still be denoted as $i_1(t)$, while the output of each bucket detector ℓ will be labeled $i_\ell(t)$ for $2 \leq \ell \leq n + 1$. We thus build up the correlation function pixel-wise as

$$C(\boldsymbol{\rho}_1) = \frac{1}{n} \sum_{\ell=2}^{n+1} \frac{1}{T_I} \int_{-T_I/2}^{T_I/2} dt i_1(t) i_\ell(t). \quad (7.1)$$

The resolution and contrast for this system can easily be found from

$$\langle C(\boldsymbol{\rho}_1) \rangle = \frac{1}{n} \sum_{\ell=2}^{n+1} \frac{1}{T_I} \int_{-T_I/2}^{T_I/2} dt \langle i_1(t) i_\ell(t) \rangle \quad (7.2)$$

by recognizing that $\langle i_1(t) i_\ell(t) \rangle$ is the same for all ℓ , and not a function of time. The average correlation function becomes $\langle C(\boldsymbol{\rho}_1) \rangle = \langle i_1(t) i_\ell(t) \rangle$, which is what was derived in Chapter 2 for one bucket detector. Thus, no resolution or contrast gain is realized by utilizing multiple bucket detectors.

However, this setup does offer a SNR enhancement. Using the SNR definition in Eq (2.21), as well as the same simplifying assumptions that allow us to use Eq (2.22) for the

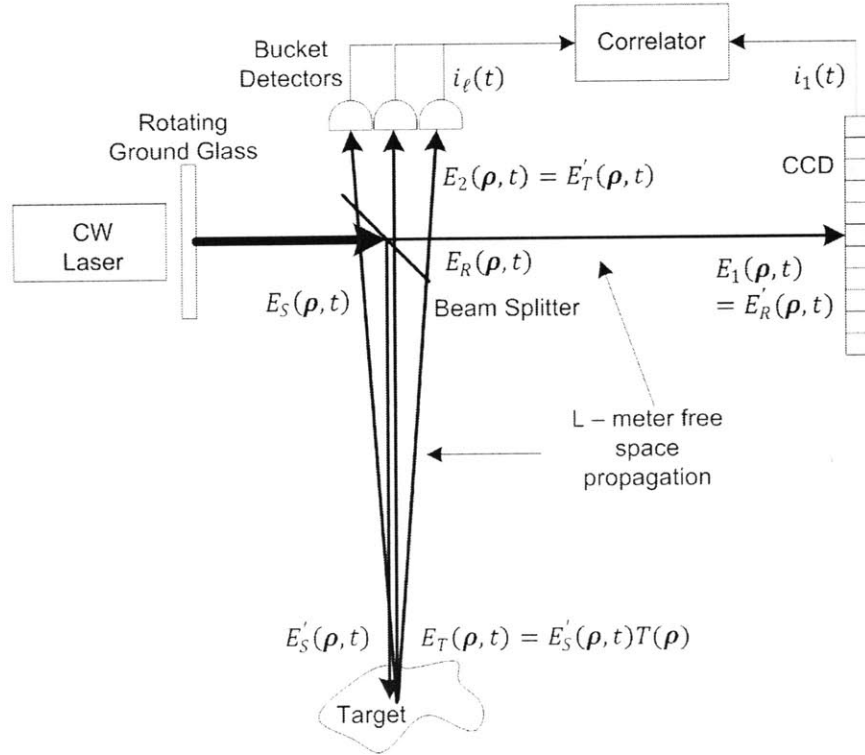


Figure 7-1: Reflective ghost imaging with multiple bucket detectors.

first moment, we are left only needing to calculate the second moment of

$$\langle C^2(\rho_1) \rangle = \frac{1}{n^2} \sum_{\ell=2}^{n+1} \sum_{m=2}^{n+1} \frac{1}{T_I^2} \int_{-T_I/2}^{T_I/2} dt \int_{-T_I/2}^{T_I/2} du \langle i_1(t) i_\ell(t) i_1(u) i_m(u) \rangle. \quad (7.3)$$

We are interested in raising the high-brightness, long integration time SNR asymptote, so we restrict our analysis to this limit, in which we find

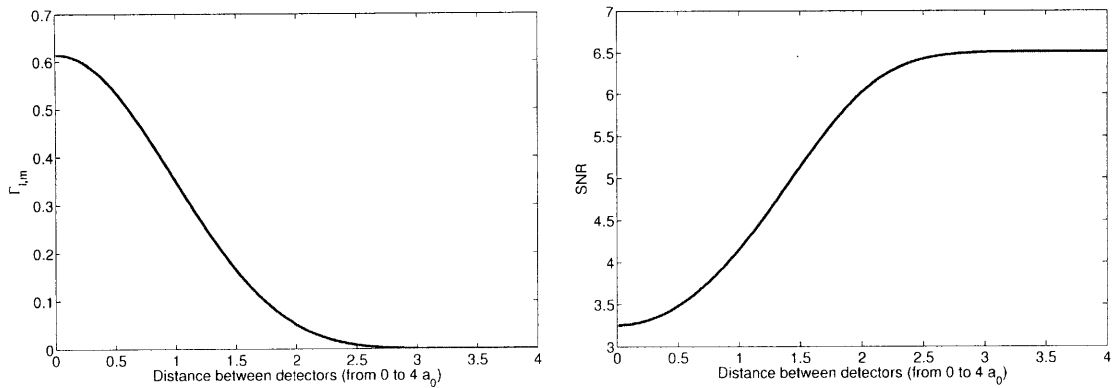
$$\text{SNR}_{H, \text{ long-}T_I} = \frac{n^2 2A_2 / \pi a_0^2}{\sum_{\ell=2}^{n+1} \sum_{m=2}^{n+1} \Gamma_{\ell, m}}, \quad (7.4)$$

where

$$\Gamma_{\ell, m} = \frac{1}{2\pi} \int d\nu e^{-|\nu - \Delta_{\ell, m}|^2 / 2} O(\nu, 4\alpha). \quad (7.5)$$

The Γ function in Eq (2.26) comes from integrating over the bucket detector in two different coordinates systems— $\boldsymbol{\rho}'$ and $\boldsymbol{\rho}''$ —a function of the difference of these coordinates. To evaluate it we moved to the normalized difference coordinates $\boldsymbol{\nu} = \rho_L k_0 (\boldsymbol{\rho}' - \boldsymbol{\rho}'')/L$ and integrated over the two-circle overlap function. This worked because the different coordinate systems were for the same bucket detector, and centered at the same point. Since we are now using multiple bucket detectors, we have to account for the difference in their transverse location. We want to recenter one coordinate system so that both are aligned by shifting it by some $\boldsymbol{\rho}'_\ell - \boldsymbol{\rho}''_m$ where $\boldsymbol{\rho}'_\ell$ is the center of detector ℓ , and $\boldsymbol{\rho}''_m$ is the center of detector m . Thus, we now define $\boldsymbol{\nu} = \rho_L k_0 (\boldsymbol{\rho}' - \boldsymbol{\rho}'')/L + \Delta_{\ell,m}$ for $\Delta_{\ell,m} = \rho_L k_0 (\boldsymbol{\rho}'_\ell - \boldsymbol{\rho}''_m)/L$, allowing us to correctly use the two-circle overlap function to evaluate our expression.

The averaging over speckle statistics is encapsulated in $\Gamma_{\ell,m}$, and is where we see the advantage of using multiple bucket detectors. As the distance between the detectors increases, $\Gamma_{\ell,m}$ and the deleterious speckle effects decrease, which leads to an SNR increase. Looking again at detector sizes of $A_2 = \pi a_0^2$, and placing two detectors side-by-side (centers separated by $2a_0$), we find $\Gamma_{\ell,m} = 0.049$, which is a significant decrease from $\Gamma_{\ell,\ell} = \Gamma = .61$; this configuration yields an SNR of 6.03. If we separate the detectors by a distance of $2a_0$ (so that the centers are $4a_0$ apart) we have $\Gamma_{\ell,m} = 4.3 \times 10^{-7}$, and a SNR of 6.52, which is twice that of the single detector case. Thus, detectors of this size that are side-by-side have slightly correlated speckle statistics, while detectors with centers separated by $4a_0$ have essentially uncorrelated speckle behavior, as can be seen in Fig. 7-2. This makes intuitive sense because the speckle fluctuation's average size are inversely proportional to the coherence length of the light illuminating the target as 'speckle length' $\equiv 2L/k_0 \rho_L = a_0$. Locations separated by lengths significantly greater than a_0 in the bucket detector plane will have uncorrelated speckle statistics. This means that adding bucket detectors far enough apart linearly increases the SNR, while detectors placed closer together will yield a slightly lower increase, as seen in Fig. 7-3. This speckle averaging is the same effect that is seen when increasing the size of the bucket detector.



(a) $\Gamma_{\ell,m}$ as a function of the distance between the center of detectors ℓ and m . (b) SNR as a function of the distance between the center of detectors ℓ and m .

Figure 7-2: $\Gamma_{\ell,m}$ for distances $d = 0$ ($\ell = m$) to $d = 4a_0$ between the centers of detectors ℓ and m , and the subsequent SNR for the two detector configuration, are plotted. The detectors are taken to have area $A_2 = \pi a_0^2$.

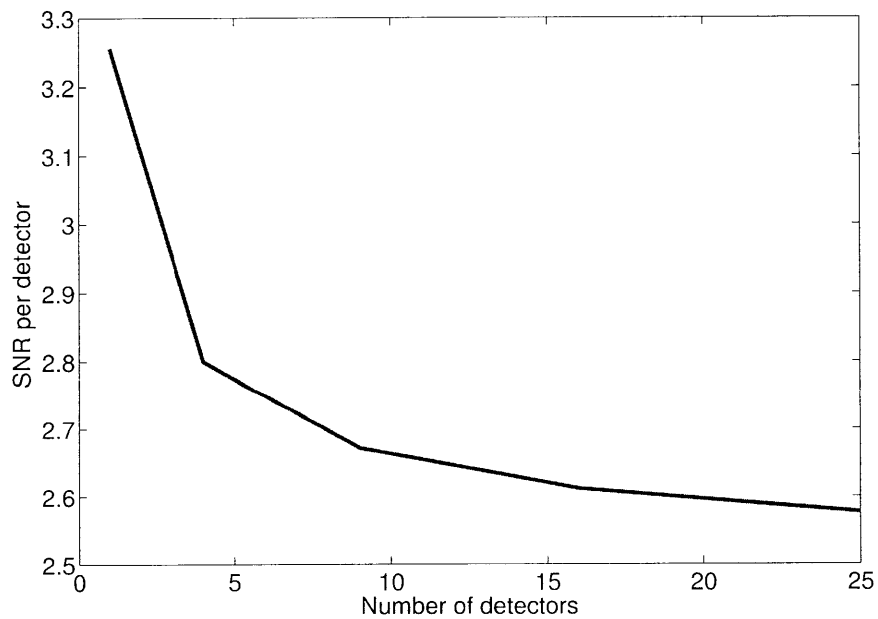


Figure 7-3: The SNR per bucket detector for square detector arrays. The collecting lens for each detector is taken to be a circle of area $A_2 = \pi a_0^2$, and they are arranged in squares (with sides touching) of size 1, 2×2 , 3×3 , 4×4 , 5×5

7.2 Multiple Wavelengths

In place of—or possibly in conjunction with—using multiple bucket detectors we can use a multiple wavelength source to increase the SNR. Whereas the bucket detectors in Sec. 7.1 see different speckle statistics due to their transverse separation, the return fields for the various wavelengths have different speckle statistics at the same transverse location because each wavelength diffracts differently from the rough surface. This will allow us to make multiple co-linear measurements to average out the effects of the target speckle.

For the multiple bucket detector setup we did a full treatment, finding the correlation between the speckle statistics for bucket detectors separated by arbitrary distances. This was because it is reasonable to assume that in an implementation we could be constrained by the size of the array; we might want to pack the detectors tightly. We should not be constrained to choosing similar wavelengths for our sources. Thus, we are only interested in finding the cut-off wavelength separation at which the return fields have uncorrelated target-speckle statistics, and the image characteristics in this regime.

We start with the setup in Fig. 7-4, and we build up the correlation function as the average of separate correlation measurements made at every wavelength. Each wavelength diffracts differently, so if we assume the same source coherence and intensity radii, the on-target average illumination pattern will be more spread out for some wavelengths, less for others. This will result in less power being measured at each detector (both CCD and bucket) at certain wavelengths; therefore, when averaging the separate correlation functions, we need to scale the measurements appropriately. For our work, we will scale each measurement by $(\bar{\rho}_L/\rho_L^{(\ell)})(a_L^{(\ell)}/\bar{a}_L)^2$, where $a_L^{(\ell)}$ and $\rho_L^{(\ell)}$ are the on-target intensity and coherence radii at wavelength λ_ℓ , and \bar{a}_L and $\bar{\rho}_L$ are the average of $\{a_L^{(\ell)}\}$ and $\{\rho_L^{(\ell)}\}$, respectively. Following our previous work, CCD output $i_1^{(\ell)}(t)$ associated with wavelength λ_ℓ is correlated with the bucket detector output $i_2^{(\ell)}(t)$ for each ℓ and averaged as

$$C(\rho_1) = \frac{1}{n} \sum_{\ell=1}^n \left(\frac{\bar{\rho}_L}{\rho_L^{(\ell)}} \right)^2 \left(\frac{a_L^{(\ell)}}{\bar{a}_L} \right)^4 \frac{1}{T_I} \int_{-T_I/2}^{T_I/2} dt i_1^{(\ell)}(t) i_2^{(\ell)}(t). \quad (7.6)$$

The resolution and image contrast are found from an ensemble average as

$$\langle C(\boldsymbol{\rho}_1) \rangle = \frac{1}{n} \sum_{\ell=1}^n \left(\frac{\bar{\rho}_L}{\rho_L^{(\ell)}} \right)^2 \left(\frac{a_L^{(\ell)}}{\bar{a}_L} \right)^4 \frac{1}{T_I} \int_{-T_I/2}^{T_I/2} dt \langle i_1^{(\ell)}(t) i_2^{(\ell)}(t) \rangle. \quad (7.7)$$

Since each $\langle i_1^{(\ell)}(t) i_2^{(\ell)}(t) \rangle$ is a function of the wavelength λ_ℓ , they each have a different point-spread function, and therefore the resolution is limited by the longest wavelength used to $\max_\ell(\rho_L^{(\ell)}) = 2L/\min_\ell(k_\ell)a_0$. Looking at the contrast, we find the background term becomes

$$C_0 = \frac{q^2 \eta^2 A_1 A_2}{L^2} \left(\frac{2P}{\pi \bar{a}_L^2} \right)^2 \frac{1}{n} \sum_{\ell=1}^n \left(\frac{\bar{\rho}_L}{\rho_L^{(\ell)}} \right)^2 \int d\boldsymbol{\rho}_2 \mathcal{T}(\boldsymbol{\rho}_2), \quad (7.8)$$

and the image-bearing term, under the assumption that each wavelength is short enough to resolve the target, becomes

$$C_1(\boldsymbol{\rho}_1) = \frac{q^2 \eta^2 A_1 A_2}{L^2} \left(\frac{2P}{\pi \bar{a}_L^2} \right)^2 \mathcal{T}(\boldsymbol{\rho}_1) \pi \bar{\rho}_L^2. \quad (7.9)$$

Using the definition in Eq (2.16), we find

$$\mathcal{C} = \frac{\pi}{A_T} \left[\sum_{\ell=1}^n \left(\frac{1}{\rho_L^{(\ell)}} \right)^2 \right]^{-1}. \quad (7.10)$$

This differs from the results for using multiple bucket detectors only slightly, as the coherence lengths are added in parallel; since the on-target coherence lengths will be of the same order of magnitude, the contrast has the same basic interpretation as being approximately the inverse of the number of resolution cells in the image.

Turning to the SNR evaluation, and the definition in Eq (2.21), we are left only needing

to evaluate the second moment of the correlation function as

$$\begin{aligned} \langle C^2(\boldsymbol{\rho}_1) \rangle &= \frac{1}{n^2} \sum_{\ell=1}^n \sum_{m=1}^n \left(\frac{\bar{\rho}_L^2}{\rho_L^{(\ell)} \rho_L^{(m)}} \right)^2 \left(\frac{a_L^{(\ell)} a_L^{(m)}}{\bar{a}_L^2} \right)^4 \\ &\times \frac{1}{T_I^2} \int_{-T_I/2}^{T_I/2} dt \int_{-T_I/2}^{T_I/2} du \langle i_1^{(\ell)}(t) i_2^{(\ell)}(t) i_1^{(m)}(u) i_2^{(m)}(u) \rangle. \end{aligned} \quad (7.11)$$

We again look at the high-brightness long-integration-time limit where the effects of the target speckle dominates. To do this we need to review our treatment of the scattering effects of the rough surface given in Eq (2.4). This treatment was for a single wavelength λ_0 , and the phase-insensitive autocorrelation is given by Eq (2.5). We are now dealing with multiple wavelengths of light, so we define the target reflection coefficient for wavelength λ_ℓ as

$$T_\ell(\boldsymbol{\rho}) = \sqrt{\mathcal{T}(\boldsymbol{\rho})} e^{2ik_\ell \Delta z(\boldsymbol{\rho})}, \quad (7.12)$$

where $k_\ell = 2\pi/\lambda_\ell$. The phase-insensitive cross correlation of reflection coefficients for different wavelengths is thus

$$\begin{aligned} \langle T_\ell^*(\boldsymbol{\rho}) T_m(\boldsymbol{\rho}') \rangle &= \sqrt{\mathcal{T}(\boldsymbol{\rho}) \mathcal{T}(\boldsymbol{\rho}')} \langle e^{-2i(k_\ell \Delta z(\boldsymbol{\rho}) - k_m \Delta z(\boldsymbol{\rho}'))} \rangle \\ &= \sqrt{\mathcal{T}(\boldsymbol{\rho}) \mathcal{T}(\boldsymbol{\rho}')} e^{-2\sigma_z^2(k_\ell^2 + k_m^2) + 4k_\ell k_m K_{zz}(\boldsymbol{\rho} - \boldsymbol{\rho}')} \end{aligned}$$

As before, we are assuming that the covariance function $K_{zz}(\boldsymbol{\rho} - \boldsymbol{\rho}')$ for the height variations $\Delta z(\boldsymbol{\rho})$ is very narrow, allowing us to approximate

$$\langle T_\ell^*(\boldsymbol{\rho}) T_m(\boldsymbol{\rho}') \rangle = \lambda_\ell \lambda_m \delta(\boldsymbol{\rho} - \boldsymbol{\rho}') \mathcal{T}(\boldsymbol{\rho}) e^{-2\sigma_z^2(k_\ell - k_m)^2} \quad (7.13)$$

Thus, when $\sigma_z^2(k_\ell - k_m)^2 = 1$, then $\langle T_\ell^*(\boldsymbol{\rho}) T_m(\boldsymbol{\rho}') \rangle = \lambda_\ell \lambda_m \delta(\boldsymbol{\rho} - \boldsymbol{\rho}') \mathcal{T}(\boldsymbol{\rho}) e^{-2} \approx 0$, and the return fields from the two different-wavelength sources are essentially uncorrelated. This

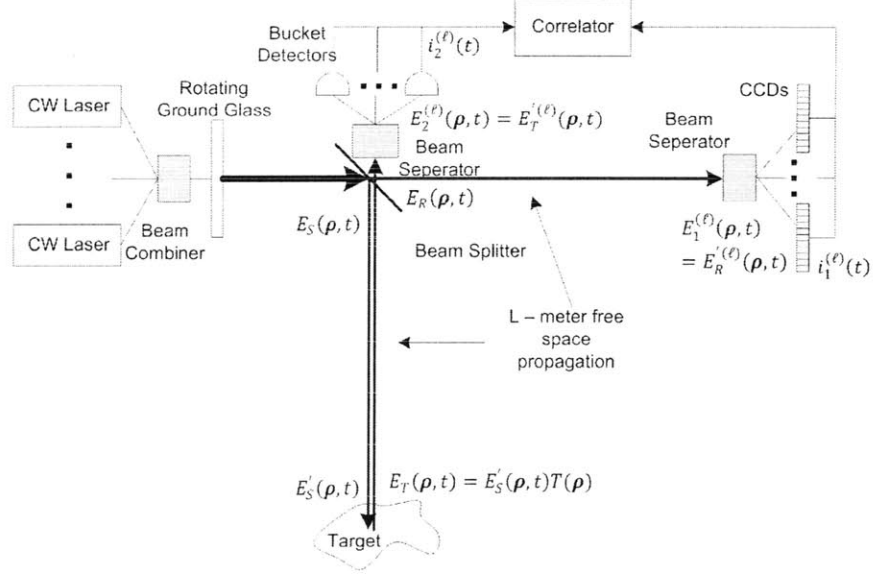


Figure 7-4: Reflective GI system using multiple lasers at different wavelengths, and one bucket detector for each wavelength.

gives us the minimum wavelength-separation criterion between two wavelengths as

$$|\Delta\lambda| \geq \frac{\bar{\lambda}^2}{2\pi\sigma_z}, \quad (7.14)$$

where $\bar{\lambda}$ is approximately the average of the wavelengths. In this regime, we can approximate the exponential as a Kronecker delta function, i.e., $e^{-2\sigma_z^2(k_\ell - k_m)^2} \rightarrow \delta_{\ell,m}$. This gives us a high-brightness long-integration-time SNR of

$$\text{SNR}_{H, \text{long-}T_I} = \frac{n2A_2}{\pi a_0^2 \Gamma}. \quad (7.15)$$

This is the same basic result we found for the multiple bucket detector setup, when the bucket detectors were sufficiently separated; averaging over multiple correlations, each with uncorrelated speckle statistics, leads to a linear increase in the maximum SNR.

7.3 Compressive Sensing

In traditional sensing methods, resolution is limited by the Nyquist rate, i.e., you must sample at a rate at least twice as high as the desired signal bandwidth in order to acquire them. However, when dealing with signals that have a sparse representation in some basis, the captured data can then be compressed, reducing the number of bits needed to accurately represent it [13]. A sparse representation means that in some basis, almost all coefficients are close to zero, so most of the information is held in only a few significant coefficients [14]. For a simple example, imagine some audio signal composed of only three frequencies. If we wanted to sample in time, then, according to Nyquist, we would have to sample at twice the highest frequency to have a faithful representation of the signal. However, in the frequency domain, this signal can be represented by only three coefficients; if we wanted to compress the signal, we could represent it in the frequency domain and only keep the three important data points corresponding to the three frequencies present, significantly reducing the number of data points required to represent the signal.

Any signal with some definable structure is likely to have a sparse representation in some basis [14]. Of interest to us are “natural images.” Natural images are generally discontinuously smooth; that is, they are composed of areas of slowly varying features that are separated by sharp boundaries. As is exploited in a number of image compression schemes, such as the ubiquitous JPEG format, natural images have a sparse representation in the 2-D discrete cosine basis [14].

Compressive sensing is a means to directly acquire the significant coefficients of a signal in its sparse basis, requiring significantly fewer measurements than if the signal was sampled at the Nyquist rate [13]. Conceptually, this technique exploits our knowledge of the structure of the image; we know that it is sparse in some basis (even though we don’t know which coefficients matter), and use this knowledge to reduce the amount of information we need to acquire.

At the heart of this technique is the notion that the information is preserved through linear transformations; therefore, by taking a series of linear projections, enough information

can be gathered to reconstruct the signal. This process involves projecting the sparse target onto a series of vectors to build up a vector of projections [14]. This series of projections takes the form of a measurement matrix \mathbf{A} such as

$$\mathbf{y} = \mathbf{A}\mathbf{x} \tag{7.16}$$

where \mathbf{x} is a sparse representation of our signal, and \mathbf{y} is the vector of projections. The most efficient measurement matrices have the lowest correlation between columns of the measurement matrix. This is often referred to as incoherence [14], and means that for each projection, each coefficient of \mathbf{x} receives a nearly uncorrelated weighting. To recover \mathbf{x} one uses linear programming methods and knowledge of the measurement matrix to find \mathbf{x} based on an L_1 -optimization.

The authors of [12] realized that the output of a bucket detector in transmissive ghost imaging is simply the projection of the target transmissivity pattern onto some illumination pattern. Therefore, by sending a series of illumination patterns at the target a data set of minimally correlated projections can be built up, which is the ideal data set for compressive sensing. By using an SLM, they controlled the illumination patterns cast on the target, and used that knowledge to perform the reconstruction. In traditional ghost imaging, the known illumination pattern is used to perform a correlation with the bucket detector's output to form an image. However, by instead performing compressive sensing on that output (again using knowledge of the illumination pattern) the sparsity of natural images is leveraged to perform a better reconstruction from fewer measurements.

The projective measurement made by the bucket detector in transmissive ghost imaging can be viewed in terms of the output current as

$$i_2(t) = \int_{\mathcal{A}_2} d\boldsymbol{\rho} I(\boldsymbol{\rho}, t) |T(\boldsymbol{\rho})|^2, \tag{7.17}$$

where $I(\boldsymbol{\rho}, t) = |E(\boldsymbol{\rho}, t)|^2$, and we are ignoring shot-noise for the moment. This can be

written in matrix form as

$$\mathbf{i}_2 = \mathbf{I}\mathbf{T} \quad (7.18)$$

where \mathbf{T} is a column vector of $|T(\boldsymbol{\rho})|^2$ indexed by the transverse location $\boldsymbol{\rho}$, \mathbf{I} is the pseudo-random measurement matrix with columns indexed by time t , and rows indexed by $\boldsymbol{\rho}$. Our output is thus a column vector indexed by time. Now, \mathbf{T} is not sparse in its spatial representation, but for the rotation matrix $\boldsymbol{\Psi}$ to some sparse basis, we have

$$\mathbf{T} = \boldsymbol{\Psi}\mathbf{T}' \quad (7.19)$$

where \mathbf{T}' is our representation of the target transmissivity in the sparse basis. If we combine the basis rotation matrix and measurement matrix as $\mathbf{A} = \mathbf{I}\boldsymbol{\Psi}$ we then have

$$\mathbf{i}_2 = \mathbf{A}\mathbf{T}'. \quad (7.20)$$

In reflective imaging, it is a little more complicated to frame the bucket detector's output as a projective measurement, due to the scattering from the rough surface. However, we can make the connection as follows. First, since the bucket detector measures the total power that passes through the collecting lens, we can theoretically look in any plane behind the lens to make our connection: the total power will be the same in every plane. Therefore, we can look in the image plane for our connection, where the transverse intensity pattern is a product of the illumination pattern $I(\boldsymbol{\rho}, t) = |E'_S(\boldsymbol{\rho}, t)|^2$, the target reflectivity $\mathcal{T}(\boldsymbol{\rho})$, and an exponentially distributed random process $S(\boldsymbol{\rho})$. Here $S(\boldsymbol{\rho})$ accounts for the effects of the rough-surface scattering, and for each pixel in the final image can be thought of as a collection of independent, identically-distributed (IID) exponential random variables. Therefore, we can write the output of the bucket detector as

$$i_2(t) = \int_{\mathcal{A}_2} d\boldsymbol{\rho} I(\boldsymbol{\rho}, t) S(\boldsymbol{\rho}) \mathcal{T}(\boldsymbol{\rho}). \quad (7.21)$$

This can be put in matrix form as

$$\mathbf{i}_2 = \mathbf{I}\mathbf{S}\mathbf{T} \tag{7.22}$$

where \mathbf{I} is the intensity matrix illuminating the target as before, \mathbf{T} is a column vector of \mathcal{T} indexed by transverse location $\boldsymbol{\rho}$, \mathbf{S} is a diagonal matrix with each element being an IID exponential random variable, and \mathbf{i}_2 is our projective measurements, indexed by time. Thus, the only difference between the transmissive and reflective cases is the diagonal matrix \mathbf{S} . Now, rotating to a sparse basis as in Eq (7.19), have an output

$$\mathbf{i}_2 = \mathbf{A}\mathbf{T}' \tag{7.23}$$

for $\mathbf{A} = \mathbf{I}\mathbf{S}\boldsymbol{\Psi}$. While our measurement matrix still has columns that are fairly uncorrelated, we no longer know the measurement matrix. Whether we can fully recover \mathbf{T}' , or merely a speckled version, is the subject of current research.

Chapter 8

Conclusion and Future Work

In this thesis we developed a framework for analyzing reflective ghost imaging systems in the context of stand-off sensing. We developed results for three possible imaging systems, which were then compared to each other as well as to a basic laser radar system. We then applied turbulence on the propagation paths for these systems and analyzed the resulting resolution degradation. Finally, we explored ways to improve reflective ghost imagers, primarily the high-brightness, long integration time SNR.

The first system we explored utilized pseudothermal light for the signal and reference beams, with a classical phase-insensitive cross correlation between them. This is realized by passing laser light through rotating ground glass, and then a 50–50 beam splitter to create identical spatiotemporally random fields on both arms. This system is perhaps the most robust of those we explored; the laser source can be made very strong without affecting the correlation between the fields, and we do not need to worry about the calibration of an SLM. The next system we investigated utilized the output of an SPDC, along with a polarizing beam splitter, to create entangled signal and reference beams with a non-classical phase-sensitive cross correlation. We evaluated these fields within a Gaussian-state framework, where the low-brightness limit is the biphoton state and the high-brightness limit is classically correlated light. Finally, we investigated a computational ghost imaging system in which the signal arm is created by modulating the phase front of a laser with an SLM, and the reference

field is calculated from the known applied phase modulations. The laser radar system we used for comparison is a flood-light system in which the target is uniformly illuminated, and a CCD array is used to make a high-resolution spatial measurement of the reflected field.

We compared these systems through their resolutions, contrasts, and signal-to-noise ratios. To facilitate the comparison we said all lenses were of identical area πa_0^2 , where a_0 is the average intensity radius of the source for ghost imagers. We found that all three ghost imagers, as well as the laser radar system, have the same effective resolution of $\rho_L = 2L/k_0 a_0$. Looking at the contrast, the pseudothermal ghost imager, SPDC ghost imager in the high-brightness regime, and the computational ghost imager have a constant background term which limits the contrast to Eq (2.18). This can be overcome by AC-coupling the outputs of either detector. In the low-brightness regime the output of the SPDC becomes the biphoton state, and the resulting images are background free. This is also true for the laser radar, and thus both systems have an unlimited contrast as defined in Eq (2.16). For AC-coupled operation, all ghost imager systems and the laser radar system have the same resolution and contrast. However, a performance difference can be found in the SNR of each system.

The maximum SNR for each system is achieved when the source is strong and the integration time is long. This averages out the shot noise in the detectors, and for ghost imaging, the speckled nature of the spatiotemporally varying light that illuminates the target. However, the roughness of the surface creates speckle in the return field that is time-invariant; integrating for longer will not remove this randomness. These target-speckle variations are different at each transverse location, and are the limiting factor in the SNR for both ghost imagers and laser radars.

However, ghost imagers have an advantage. The size of the target-induced speckle is inversely proportional to the coherence length of the light at the target. Thus, the average size of these speckles for a ghost imager is $a_0 = 2L/k_0 \rho_L$. If our receiving lens is of the same size as, or larger than, the transmitting lens, there will be some averaging of the speckle by the bucket detector. For laser radar the target is illuminated with nearly uniform light, so the speckle size cast on the receiving lens is much smaller than for a ghost imager. However,

for ghost imaging the light is captured by a bucket detector, while for a laser radar the light is focused onto a CCD array; the speckle size is much larger than a CCD pixel, resulting in almost no speckle averaging. Therefore, while the laser radar system is limited to $\text{SNR} = 1$, the ghost imager can achieve an SNR in the low single digits. As discussed in Chapter 2, for a receiving lens of area $A_2 = \pi a_0^2$, the maximum SNR for the ghost imagers is 3.266.

For low-brightness situations, we saw a larger difference in the SNR behavior of the various systems. For the pseudothermal ghost imager, we make two measurements of classical light, and thus have randomness from both measurements. For the SPDC imager, the low-brightness limit is approximately the biphoton state; while we still have randomness from the two measurements, it is significantly lower than for the pseudothermal imager. However, the computational imager has a better low-brightness SNR asymptote than both systems, as it only has randomness from one measurement. The only area where the laser radar has better SNR characteristics than the ghost imagers is for very short integration times, and very high-brightness illumination. This is because the laser radar only has to overcome shot noise, which can be accomplished with either a long integration time or high-brightness illumination; the ghost imagers also have to average out the randomness of the source, which can only be accomplished with a sufficiently long integration time.

After exploring the basic image characteristics for these systems, we looked at the effects of turbulence on the image resolution. We found that ghost imagers, classical or quantum, have the same resolution degradation from turbulence. There was less degradation for computational imaging, as there is no turbulence on the reference path. It is also worth noting that turbulence on the return path, from the target to the bucket detector, has no effect on resolution. In comparison, the laser radar system had the same degradation as the computational imager. Thus, ghost imagers and laser radar systems suffer similar resolution degradation from turbulence.

Finally, we looked at ways of improving the SNR performance of ghost imaging. We showed that bucket detectors spaced far enough apart measure light with uncorrelated target-speckle statistics; thus, by using multiple bucket detectors at different transverse locations,

we can increase the maximum SNR linearly with the number of detectors. We also showed that light sources far enough apart in wavelength result in uncorrelated target-speckle statistics at the bucket detector; thus, by measuring each wavelength separately we can increase the SNR linearly with the number of source wavelengths utilized. We also explored applying compressive sensing methods to improve image quality while reducing image capture time.

We have provided a simple connection between reflective ghost imaging and compressive sensing, but some theoretical issues require further exploration. If the target has a sparse representation, then a speckled version of the target should still have a sparse representation (though not as sparse). Therefore, we should be able to reconstruct the speckled version of the target with compressive sensing. However, we would like to reconstruct the actual target without the speckle. We will look into ways of adapting compressive sensing techniques to do this, possibly utilizing multiple bucket detectors or multiple wavelength sources. We will also explore ways of measuring the quality of these images, and perform a more rigorous comparison to modern pulsed laser radar systems.

Appendix A

Detailed SNR Derivation

In this appendix we will show in more detail the derivations performed to arrive at the SNR expressions for the pseudothermal ghost imager in Eq (2.28) and the SPDC imager in Eq (3.18). These derivations parallel each other, so we will not show as much detail in the derivation of Eq (3.18); the differences are in the sources of noise, the correlation functions, and the complexity of the subsequent integrations. To complete the SNR derivations, we need to calculate the second moment of the correlation function $\langle C^2(\boldsymbol{\rho}_1) \rangle$.

A.1 Pseudothermal Ghost Imager

We will first perform the derivation for the pseudothermal ghost imager, and thus start with the second moment

$$\langle C^2(\boldsymbol{\rho}_1) \rangle = \frac{1}{T_I^2} \int_{-T_I/2}^{T_I/2} dt \int_{-T_I/2}^{T_I/2} du \langle i_1(t) i_2(t) i_1(u) i_2(u) \rangle. \quad (\text{A.1})$$

Using Eq (2.2) to expand the current expressions, recognizing the statistical independence of the shot noise and the fields, and using our shot noise assumptions from Chapter 2 we

arrive at

$$\begin{aligned}
\langle i_1(t)i_2(t)i_1(u)i_2(u) \rangle = & \\
& \int d\tau_1 \int d\tau_2 \int d\tau_3 \int d\tau_4 h(t - \tau_1)h(t - \tau_2)h(u - \tau_3)h(u - \tau_4) \times \\
& [q^4\eta^4 \langle P_1(\tau_1)P_2(\tau_2)P_1(\tau_3)P_2(\tau_4) \rangle + q^2\eta^2 \langle P_1(\tau_1)P_1(\tau_3)\Delta i_2(\tau_2)\Delta i_2(\tau_4) \rangle + \\
& q^2\eta^2 \langle P_2(\tau_2)P_2(\tau_4)\Delta i_1(\tau_1)\Delta i_1(\tau_3) \rangle + \langle \Delta i_1(\tau_1)\Delta i_1(\tau_3)\Delta i_2(\tau_2)\Delta i_2(\tau_4) \rangle]
\end{aligned}$$

Using iterated expectations and $\langle \Delta i_m(t_1)\Delta i_m(t_2) \rangle = q^2\eta P_m(t_1)\delta(t_1 - t_2)$, Eq (A.1) can be written as the sum of four terms as

$$\langle C^2(\boldsymbol{\rho}_1) \rangle = T_1 + T_2 + T_3 + T_4 \quad (\text{A.2})$$

where

$$\begin{aligned}
T_1 &= \int d\tau_1 \int d\tau_2 \int d\tau_3 \int d\tau_4 \int_{A_2} d\boldsymbol{\rho}' \int_{A_2} d\boldsymbol{\rho}'' h(t - \tau_1)h(t - \tau_2)h(u - \tau_3)h(u - \tau_4) \\
&\quad \times q^4\eta^4 A_1^2 \langle |E_1(\boldsymbol{\rho}_1, \tau_1)|^2 |E_2(\boldsymbol{\rho}', \tau_2)|^2 |E_1(\boldsymbol{\rho}_1, \tau_3)|^2 |E_2(\boldsymbol{\rho}'', \tau_4)|^2 \rangle, \\
T_2 &= \int d\tau_1 \int d\tau_2 \int d\tau_3 \int_{A_2} d\boldsymbol{\rho}' h(t - \tau_1)h(t - \tau_2)h(u - \tau_3)h(u - \tau_2) \\
&\quad \times q^4\eta^3 A_1^2 \langle |E_1(\boldsymbol{\rho}_1, \tau_1)|^2 |E_1(\boldsymbol{\rho}_1, \tau_3)|^2 |E_2(\boldsymbol{\rho}', \tau_2)|^2 \rangle, \\
T_3 &= \int d\tau_1 \int d\tau_2 \int d\tau_4 \int_{A_2} d\boldsymbol{\rho}' \int_{A_2} d\boldsymbol{\rho}'' h(t - \tau_1)h(t - \tau_2)h(u - \tau_1)h(u - \tau_4) \\
&\quad \times q^4\eta^3 A_1 \langle |E_1(\boldsymbol{\rho}_1, \tau_1)|^2 |E_2(\boldsymbol{\rho}', \tau_2)|^2 |E_2(\boldsymbol{\rho}'', \tau_4)|^2 \rangle, \\
T_4 &= \int d\tau_1 \int d\tau_2 h(t - \tau_1)h(t - \tau_2)h(u - \tau_1)h(u - \tau_2) q^4\eta^2 \langle |E_1(\boldsymbol{\rho}_1, \tau_1)|^2 |E_2(\boldsymbol{\rho}', \tau_2)|^2 \rangle.
\end{aligned}$$

These four terms represent our four sources of noise: T_1 comes from the randomness of the fields at the detectors due to the fluctuations of the pseudothermal source and scattering off the target; T_2 arises from the randomness in the field at the high spatial-resolution detector beating with the shot noise in the bucket detector; T_3 comes from the randomness in the field at the bucket detector beating with the shot noise in the high spatial-resolution detector;

and finally, T_4 is the beat of the shot noises from the two detectors. The most complicated of these terms is T_1 , and in fact the methods used to solve the other terms are a subset of those used to solve T_1 . Therefore, we will show the most detail in the derivation of T_1 , and show the parallels for the other terms.

A.1.1 Source fluctuations noise term, T_1

To evaluate T_1 we want our averaging of the fields to be a jointly Gaussian eighth-order moment, so that we can use Gaussian-moment factoring. However, the measured fields $E_1(\boldsymbol{\rho}_1, t)$ and $E_2(\boldsymbol{\rho}, t)$ are not jointly Gaussian, due to the reflection off of the target. Since we are using a semiclassical treatment, we directly measure the fields impinging the detectors, so $E_1(\boldsymbol{\rho}, t) = E'_R(\boldsymbol{\rho}_1, t)$ and $E_2(\boldsymbol{\rho}, t) = E'_T(\boldsymbol{\rho}, t)$, the latter of which we can back propagate to $E'_S(\boldsymbol{\rho}', t)$ by Eq (2.3).

With that, we find the field average from T_1 becomes

$$\begin{aligned} \langle |E_1(\boldsymbol{\rho}_1, \tau_1)|^2 |E_2(\boldsymbol{\rho}', \tau_2)|^2 |E_1(\boldsymbol{\rho}_1, \tau_3)|^2 |E_2(\boldsymbol{\rho}'', \tau_4)|^2 \rangle &= \left(\frac{k_0}{2\pi L} \right)^4 \int d\boldsymbol{\rho}_2 \int d\boldsymbol{\rho}_3 \int d\boldsymbol{\rho}_4 \int d\boldsymbol{\rho}_5 \\ &\times \langle E_R'^*(\boldsymbol{\rho}_1, \tau_1) E_R'(\boldsymbol{\rho}_1, \tau_1) E_S'^*(\boldsymbol{\rho}_2, \tau_2) E_S'(\boldsymbol{\rho}_3, \tau_2) E_R'^*(\boldsymbol{\rho}_1, \tau_3) E_R'(\boldsymbol{\rho}_1, \tau_3) E_S'^*(\boldsymbol{\rho}_4, \tau_4) E_S'(\boldsymbol{\rho}_5, \tau_4) \rangle \\ &\times \langle T^*(\boldsymbol{\rho}_2) T(\boldsymbol{\rho}_3) T^*(\boldsymbol{\rho}_4) T(\boldsymbol{\rho}_5) \rangle e^{-\frac{ik_0}{2L}(L+|\boldsymbol{\rho}'-\boldsymbol{\rho}_2|^2)} e^{\frac{ik_0}{2L}(L+|\boldsymbol{\rho}'-\boldsymbol{\rho}_3|^2)} e^{-\frac{ik_0}{2L}(L+|\boldsymbol{\rho}''-\boldsymbol{\rho}_4|^2)} e^{\frac{ik_0}{2L}(L+|\boldsymbol{\rho}''-\boldsymbol{\rho}_5|^2)}. \end{aligned}$$

We now have a fourth-order moment in the target surface, and an eighth-order moment in the fields to evaluate. Both terms are higher-order moments of zero-mean Gaussian random processes, so we can apply the Gaussian-moment factoring theorem to express them in terms of second order moments. Since we are using pseudothermal light, only the phase-insensitive moments matter; the phase-sensitive cross correlation between $E'_S(\boldsymbol{\rho}, t)$ and $E'_R(\boldsymbol{\rho}, t)$, as well as the phase-sensitive autocorrelation for each field, are zero. The same is true for the surface, which only has a phase-insensitive autocorrelation. Thus,

$$\begin{aligned} \langle T^*(\boldsymbol{\rho}_2) T(\boldsymbol{\rho}_3) T^*(\boldsymbol{\rho}_4) T(\boldsymbol{\rho}_5) \rangle &= \delta(\boldsymbol{\rho}_2 - \boldsymbol{\rho}_3) \delta(\boldsymbol{\rho}_4 - \boldsymbol{\rho}_5) \lambda_0^4 \mathcal{T}(\boldsymbol{\rho}_2) \mathcal{T}(\boldsymbol{\rho}_4) \\ &+ \delta(\boldsymbol{\rho}_2 - \boldsymbol{\rho}_5) \delta(\boldsymbol{\rho}_4 - \boldsymbol{\rho}_3) \lambda_0^4 \mathcal{T}(\boldsymbol{\rho}_2) \mathcal{T}(\boldsymbol{\rho}_4), \end{aligned} \quad (\text{A.3})$$

giving us

$$\begin{aligned}
\langle |E_1(\boldsymbol{\rho}_1, \tau_1)|^2 |E_2(\boldsymbol{\rho}', \tau_2)|^2 |E_1(\boldsymbol{\rho}_1, \tau_3)|^2 |E_2(\boldsymbol{\rho}'', \tau_4)|^2 \rangle &= \frac{1}{L^4} \int d\boldsymbol{\rho}_2 \int d\boldsymbol{\rho}_4 \mathcal{T}(\boldsymbol{\rho}_2) \mathcal{T}(\boldsymbol{\rho}_4) \\
&\times [\langle E_R'^*(\boldsymbol{\rho}_1, \tau_1) E_R'(\boldsymbol{\rho}_1, \tau_1) E_S'^*(\boldsymbol{\rho}_2, \tau_2) E_S'(\boldsymbol{\rho}_2, \tau_2) E_R'^*(\boldsymbol{\rho}_1, \tau_3) E_R'(\boldsymbol{\rho}_1, \tau_3) E_S'^*(\boldsymbol{\rho}_4, \tau_4) E_S'(\boldsymbol{\rho}_4, \tau_4) \rangle \\
&+ \langle E_R'^*(\boldsymbol{\rho}_1, \tau_1) E_R'(\boldsymbol{\rho}_1, \tau_1) E_S'^*(\boldsymbol{\rho}_2, \tau_2) E_S'(\boldsymbol{\rho}_4, \tau_2) E_R'^*(\boldsymbol{\rho}_1, \tau_3) E_R'(\boldsymbol{\rho}_1, \tau_3) E_S'^*(\boldsymbol{\rho}_4, \tau_4) E_S'(\boldsymbol{\rho}_2, \tau_4) \rangle \\
&\times e^{\frac{ik_0}{L} \boldsymbol{\rho}_2 \cdot (\boldsymbol{\rho}' - \boldsymbol{\rho}'')} e^{-\frac{ik_0}{L} \boldsymbol{\rho}_4 \cdot (\boldsymbol{\rho}' - \boldsymbol{\rho}'')}]. \tag{A.4}
\end{aligned}$$

We now apply the Gaussian-moment factoring theorem to the eighth-order field moments, setting all phase-sensitive moments to zero and applying our DC-block filter, to arrive at a complicated expression that is a function of the propagated Gaussian-Schell correlation function in Eq (2.10). In this model the time and space arguments are separable, so we can perform the time integrations (over $u, t, \tau_1, \tau_2, \tau_3, \tau_4$) and the spatial integrations (over $\boldsymbol{\rho}_2, \boldsymbol{\rho}_4, \boldsymbol{\rho}', \boldsymbol{\rho}''$) separately.

Time integrations Each time integral is of some function that is a product of correlations functions and detector responses, all of which are of a Gaussian form. This means that the integrations, while complicated, are tractable for a computer to evaluate. The end result is a function of exponentials and error functions, but using our assumption of $T_I/T_0 \gg 1$ we can say that $\text{erf}[T_I/T_0] \approx 1$ and $\exp[-(T_I/T_0)^2] \approx 0$, giving us fairly simple results.

Spatial integrations The spatial integrals are more complex, as the target surface is involved, and not all of the propagation terms canceled. However, the the correlation functions are Gaussian, so with a few basic manipulations we can evaluate these integrals. First, we apply our previously stated assumptions that the the coherence length at the target is small enough to resolve all features, and the intensity radius is large enough that the average on-target illumination pattern is approximately constant so that

$$\int d\boldsymbol{\rho}_2 \mathcal{T}(\boldsymbol{\rho}_2) e^{-2|\boldsymbol{\rho}_2|^2/a_L^2} e^{-|\boldsymbol{\rho}_1 - \boldsymbol{\rho}_2|^2/\rho_L^2} \approx \mathcal{T}(\boldsymbol{\rho}_1) \int d\boldsymbol{\rho}_2 e^{-|\boldsymbol{\rho}_1 - \boldsymbol{\rho}_2|^2/\rho_L^2}. \tag{A.5}$$

Second, we define the Fourier transform of the target as $\mathbb{T}(\boldsymbol{\xi})$ so that

$$\int d\boldsymbol{\rho}_2 \mathcal{T}(\boldsymbol{\rho}_2) e^{-\frac{ik_0}{L} \boldsymbol{\rho}_2 \cdot (\boldsymbol{\rho}' - \boldsymbol{\rho}'')} = \mathbb{T}\left(\frac{k_0}{L}(\boldsymbol{\rho}' - \boldsymbol{\rho}'')\right). \quad (\text{A.6})$$

Finally, we need to handle the integrations at the bucket detector. For the first eighth-order term in Eq (A.4), the propagation terms cancel, so we can simply evaluate $\int_{\mathcal{A}_2} d\boldsymbol{\rho}' \int_{\mathcal{A}_2} d\boldsymbol{\rho}'' = A_2^2$. However, in the second term, the propagation terms do not all cancel, and leave complex exponentials that will effect a Fourier transform to the difference coordinates $\frac{k_0}{L}(\boldsymbol{\rho}' - \boldsymbol{\rho}'')$. This will leave us needing to evaluate three different functions of these difference coordinates.

First, we have

$$\int_{\mathcal{A}_2} d\boldsymbol{\rho}' \int_{\mathcal{A}_2} d\boldsymbol{\rho}'' e^{-\frac{\rho_L^2 k_0^2 |\boldsymbol{\rho}' - \boldsymbol{\rho}''|^2}{2L^2}} = A_2 \frac{L^2}{\rho_L^2 k_0^2} \int d\boldsymbol{\nu} e^{-\frac{|\boldsymbol{\nu}|^2}{2}} O(\boldsymbol{\nu}, 4\alpha), \quad (\text{A.7})$$

where we have employed the normalized difference coordinate $\boldsymbol{\nu} = \rho_L k_0 (\boldsymbol{\rho}' - \boldsymbol{\rho}'')/L$, and are utilizing the two-circle overlap function and parameter $\alpha = \sqrt{A_2/\pi a_0^2}$ as defined in Chapter 2. There is no closed form of this integral that we could identify, but it is constant for a given α , so we have defined the normalized parameter Γ in Eq (2.26) so that

$$\int_{\mathcal{A}_2} d\boldsymbol{\rho}' \int_{\mathcal{A}_2} d\boldsymbol{\rho}'' e^{-\frac{\rho_L^2 k_0^2 |\boldsymbol{\rho}' - \boldsymbol{\rho}''|^2}{2L^2}} = A_2 a_0^2 \pi \frac{\Gamma}{2}. \quad (\text{A.8})$$

Second, we need to evaluate terms of the form

$$\mathcal{T}(\boldsymbol{\rho}_1) \int_{\mathcal{A}_2} d\boldsymbol{\rho}' \int_{\mathcal{A}_2} d\boldsymbol{\rho}'' \mathbb{T}\left(\frac{k_0}{L}(\boldsymbol{\rho}' - \boldsymbol{\rho}'')\right) e^{-\frac{\rho_L^2 k_0^2 |\boldsymbol{\rho}' - \boldsymbol{\rho}''|^2}{2L^2}} e^{\frac{ik_0}{L} \boldsymbol{\rho}_1 \cdot (\boldsymbol{\rho}' - \boldsymbol{\rho}'')}. \quad (\text{A.9})$$

To do this we will employ the difference coordinate $\boldsymbol{\xi} = \frac{k_0}{L}(\boldsymbol{\rho}' - \boldsymbol{\rho}'')$ and the inverse Fourier transform definition

$$x(\boldsymbol{\rho}) = \mathcal{F}^{-1}[\mathbb{X}(\boldsymbol{\xi})](\boldsymbol{\rho}) = \frac{1}{(2\pi)^2} \int d\boldsymbol{\xi} \mathbb{X}(\boldsymbol{\xi}) e^{i\boldsymbol{\xi} \cdot \boldsymbol{\rho}}$$

to arrive at

$$\begin{aligned} \mathcal{T}(\boldsymbol{\rho}_1) & \int_{\mathcal{A}_2} d\boldsymbol{\rho}' \int_{\mathcal{A}_2} d\boldsymbol{\rho}'' \mathbb{T} \left(\frac{k_0}{L} (\boldsymbol{\rho}' - \boldsymbol{\rho}'') \right) e^{-\frac{\rho_L^2 k_0^2}{2L^2} |\boldsymbol{\rho}' - \boldsymbol{\rho}''|^2} e^{\frac{ik_0}{L} \boldsymbol{\rho}_1 \cdot (\boldsymbol{\rho}' - \boldsymbol{\rho}'')} \\ & = \mathcal{T}(\boldsymbol{\rho}_1) A_2 \frac{L^2}{k_0^2} \mathcal{F}^{-1}[\mathbb{T}(\boldsymbol{\xi})](\boldsymbol{\rho}_1) * \mathcal{F}^{-1}[e^{-\rho_L^2 |\boldsymbol{\xi}|^2/2}(\boldsymbol{\xi})](\boldsymbol{\rho}_1) * \mathcal{F}^{-1} \left[O \left(\boldsymbol{\xi}, 2 \frac{k_0}{L} \sqrt{\frac{A_2}{\pi}} \right) (\boldsymbol{\xi}) \right] (\boldsymbol{\rho}_1). \end{aligned}$$

Since $\mathcal{F}^{-1}[\mathbb{T}(\boldsymbol{\xi})](\boldsymbol{\rho}_1) = \mathcal{T}(\boldsymbol{\rho}_1)$ and $\mathcal{F}^{-1}[e^{-\rho_L^2 |\boldsymbol{\xi}|^2/2}(\boldsymbol{\xi})](\boldsymbol{\rho}_1) = (1/\pi \rho_L^2) e^{-|\boldsymbol{\rho}_1|^2/2\rho_L^2}$, and ρ_L is small enough to resolve all features, we have $\mathcal{F}^{-1}[\mathbb{T}(\boldsymbol{\xi})](\boldsymbol{\rho}_1) * \mathcal{F}^{-1}[e^{-\rho_L^2 |\boldsymbol{\xi}|^2/2}(\boldsymbol{\xi})](\boldsymbol{\rho}_1) = \mathcal{T}(\boldsymbol{\rho}_1)$. Also, the two-circle overlap function $O(\boldsymbol{\xi}, 2r)$ is simply the convolution of two circles of radius r as

$$\pi r^2 O(\boldsymbol{\xi}, 2r) = \text{circ} \left(\frac{|\boldsymbol{\xi}|}{r} \right) * \text{circ} \left(\frac{|\boldsymbol{\xi}|}{r} \right), \quad (\text{A.10})$$

where $\text{circ}(\cdot)$ is the unit-length circle function. The inverse Fourier transform of a circle is a Jinc function as

$$\pi r^2 \mathcal{F}^{-1} [O(\boldsymbol{\xi}, 2r)(\boldsymbol{\xi})](\boldsymbol{\rho}_1) = r^4 \left(\frac{J_1(|\boldsymbol{\rho}_1|r)}{|\boldsymbol{\rho}_1|r} \right)^2, \quad (\text{A.11})$$

whose width is $\sim \rho_L$ and thus resolves the target. This leaves us with

$$\mathcal{T}(\boldsymbol{\rho}_1) \int d\boldsymbol{\rho}' \int d\boldsymbol{\rho}'' \mathbb{T} \left(\frac{k_0}{L} (\boldsymbol{\rho}' - \boldsymbol{\rho}'') \right) e^{-\frac{\rho_L^2 k_0^2}{2L^2} |\boldsymbol{\rho}' - \boldsymbol{\rho}''|^2} e^{\frac{ik_0}{L} \boldsymbol{\rho}_1 \cdot (\boldsymbol{\rho}' - \boldsymbol{\rho}'')} = \mathcal{T}^2(\boldsymbol{\rho}_1) A_2 \frac{L^2}{k_0^2}. \quad (\text{A.12})$$

Finally, we need to evaluate $\int_{\mathcal{A}_2} d\boldsymbol{\rho}' \int_{\mathcal{A}_2} d\boldsymbol{\rho}'' \left| \mathbb{T} \left(\frac{k_0}{L} (\boldsymbol{\rho}' - \boldsymbol{\rho}'') \right) \right|^2$. We again use difference coordinates and the two-circle overlap function to evaluate this, and define the term A'_F as in Eq (2.25) to arrive at

$$\int_{\mathcal{A}_2} d\boldsymbol{\rho}' \int_{\mathcal{A}_2} d\boldsymbol{\rho}'' \left| \mathbb{T} \left(\frac{k_0}{L} (\boldsymbol{\rho}' - \boldsymbol{\rho}'') \right) \right|^2 = A_2 \frac{L^2}{k_0^2} A'_F. \quad (\text{A.13})$$

It should be noted that, by Parseval's theorem, $A'_T \geq A'_F$, with equality when $\mathbb{T}(\boldsymbol{\xi})$ is very narrow, in which case $A'_F \approx \int d\boldsymbol{\xi} |\mathbb{T}(\boldsymbol{\xi})|^2 = \int d\boldsymbol{\rho} |\mathcal{T}(\boldsymbol{\rho})|^2 = A'_T$. With the final assumption

of $A'_T/\rho_L^2 \gg 30$, we can combining all of these terms to arrive at an expression for the field noise of

$$T_1 = \left(\frac{2P}{\pi a_L^2} \right)^4 \frac{A_1^2 A_2^2 q^4 \eta^4 \pi^2 \rho_L^4 T_0}{L^4 T_I} \left[\frac{A'_T}{\sqrt{2\pi} \rho_L^2} + \frac{T_I}{T_0} \mathcal{T}^2(\boldsymbol{\rho}_1) + \frac{A'_F}{\sqrt{2\pi} \rho_L^4} \frac{L^2}{A_2 \pi k_0^2} + \frac{T_I}{T_0} \frac{2\pi L^2 \Gamma}{A_2 k_0^2 \rho_L^2} \mathcal{T}(\boldsymbol{\rho}_1) \right]. \quad (\text{A.14})$$

A.1.2 Remaining noise terms

Evaluating the next three terms only involves a subset of the operations needed evaluate T_1 . We again need to back propagate to $E'_S(\boldsymbol{\rho}', t)$ with Eq (2.3) to arrive at functions of higher-order Gaussian moments. For T_2 and T_3 we evaluate sixth-order Gaussian moments, and for T_4 we have a fourth-order Gaussian moment; all of these can be expressed in terms of sums of products of the correlation function in Eq (2.10) by Gaussian-moment factoring. All of the temporal integrations occur over a products of Gaussians, and can again be evaluated by mathematical software, such as MATLAB or Mathematica. All of the spatial integrals can be evaluated with the methods used for T_1 . With this, we arrive at expression for these three noise terms as

$$T_2 = \left(\frac{2P}{\pi a_L^2} \right)^3 \frac{q^4 \eta^3 A_1^2 A_2 2\pi \rho_L^2}{L^2 T_I} \mathcal{T}(\boldsymbol{\rho}_1) \quad (\text{A.15})$$

$$T_3 = \left(\frac{2P}{\pi a_L^2} \right)^3 \frac{q^4 \eta^3 A_1 A_2 2\pi \rho_L^2}{L^4 T_I} \left[\frac{4\pi A_2 \rho_L^2}{3} + \frac{L^2}{k_0^2} \right] \mathcal{T}^2(\boldsymbol{\rho}_1) \quad (\text{A.16})$$

$$T_4 = \left(\frac{2P}{\pi a_L^2} \right)^2 \frac{q^4 \eta^2 A_1 A_2 \sqrt{\pi} \rho_L^2 \Omega_B}{4\sqrt{2} L^2 T_I} \mathcal{T}(\boldsymbol{\rho}_1). \quad (\text{A.17})$$

Combining all of these terms, and substituting $a_0 = 2L/k_0 \rho_L$, we now can write the

second moment of the correlation function from Eq (A.2) as

$$\begin{aligned}
\langle C^2(\boldsymbol{\rho}_1) \rangle &= \left(\frac{2P}{\pi a_L^2} \right)^4 \frac{A_1^2 A_2^2 q^4 \eta^4 T_0}{L^4} \frac{\pi^2 \rho_L^4}{T_I} \\
&\times \left[\frac{A'_T}{\sqrt{2\pi} \rho_L^2} + \frac{T_I}{T_0} \mathcal{T}^2(\boldsymbol{\rho}_1) + \frac{A'_F}{\sqrt{2\pi} \rho_L^2} \frac{a_0^2}{4\pi A_2} + \frac{T_I}{T_0} \frac{\Gamma}{2} \frac{\pi a_0^2}{A_2} \mathcal{T}(\boldsymbol{\rho}_1) \right. \\
&+ \frac{a_L^2}{PL^2 T_0 \eta A_2 \rho_L^2} \mathcal{T}(\boldsymbol{\rho}_1) + \frac{\pi a_L^2}{PL^4 T_0 \eta A_1} \left[\frac{4}{3} + \frac{a_0^2}{4\pi A_2} \right] \mathcal{T}^2(\boldsymbol{\rho}_1) \\
&\left. + \frac{a_L^4 \sqrt{\pi} \Omega_B}{16\sqrt{2} P^2 \rho_L^2 \eta^2 A_1 A_2 L^2 T_0} \mathcal{T}(\boldsymbol{\rho}_1) \right]. \tag{A.18}
\end{aligned}$$

The mean of the correlation function can be found in Eq (2.22), giving us a squared mean of

$$\langle C(\boldsymbol{\rho}_1) \rangle^2 = \frac{A_1^2 A_2^2 q^4 \eta^4}{L^4} \left(\frac{2P}{\pi a_L^2} \right)^4 \pi^2 \rho_L^4 \mathcal{T}^2(\boldsymbol{\rho}_1). \tag{A.19}$$

Combining this with the second moment in Eq (A.18), and substituting the dimensionless brightness term $\mathcal{I} = PT_0 \rho_L^2 / a_L^2$, we arrive at to SNR of

$$\begin{aligned}
\text{SNR} &= \frac{\langle C(\boldsymbol{\rho}_1) \rangle^2}{\langle C^2(\boldsymbol{\rho}_1) \rangle - \langle C(\boldsymbol{\rho}_1) \rangle^2} \\
&= \frac{T_I}{T_0} \mathcal{T}^2(\boldsymbol{\rho}_1) \left/ \left[\frac{A'_T}{\sqrt{2\pi} \rho_L^2} + \frac{T_I}{T_0} \mathcal{T}^2(\boldsymbol{\rho}_1) + \frac{A'_F}{\sqrt{2\pi} \rho_L^2} \frac{a_0^2}{4\pi A_2} + \frac{T_I}{T_0} \frac{\Gamma}{2} \frac{\pi a_0^2}{A_2} \mathcal{T}(\boldsymbol{\rho}_1) \right. \right. \\
&\left. \left. + \frac{L^2}{\eta \mathcal{I} A_2} \mathcal{T}(\boldsymbol{\rho}_1) + \frac{\pi \rho_L^2}{A_1 \eta \mathcal{I}} \left[\frac{4}{3} + \frac{a_0^2}{4\pi A_2} \right] \mathcal{T}^2(\boldsymbol{\rho}_1) + \frac{T_0 \Omega_B \rho_L^2 \sqrt{\pi} L^2}{16\sqrt{2} A_1 \eta^2 \mathcal{I}^2 A_2} \mathcal{T}(\boldsymbol{\rho}_1) - \frac{T_I}{T_0} \mathcal{T}^2(\boldsymbol{\rho}_1) \right] \right., \tag{A.20}
\end{aligned}$$

which simplifies to Eq (2.28), which we reproduce here:

$$\begin{aligned}
\text{SNR} &= \frac{\mathcal{T}^2(\boldsymbol{\rho}_1) \frac{T_I}{T_0}}{\frac{A'_T + A'_F \frac{a_0^2}{4\pi A_2}}{\sqrt{2\pi} \rho_L^2} + \mathcal{T}^2(\boldsymbol{\rho}_1) \frac{T_I}{T_0} \frac{\Gamma \pi a_0^2}{2A_2} + \frac{\mathcal{T}(\boldsymbol{\rho}_1) L^2}{\eta \mathcal{I} A_2} + \frac{\pi \rho_L^2 \mathcal{T}^2(\boldsymbol{\rho}_1)}{A_1 \eta \mathcal{I}} \left[\frac{4}{3} + \frac{a_0^2}{4\pi A_2} \right] + \frac{\mathcal{T}(\boldsymbol{\rho}_1) T_0 \Omega_B \rho_L^2 \sqrt{\pi} L^2}{16\sqrt{2} A_1 \eta^2 \mathcal{I}^2} \frac{L^2}{A_2}}. \tag{A.21}
\end{aligned}$$

A.2 SPDC Ghost Imager

The derivation for the SPDC ghost imager closely follows that of the pseudothermal ghost imager, so we will provide a less detailed derivation. The deviations come in the generation of the noise terms, their physical interpretation, and the cross correlation function between the signal and reference fields.

As before, the SNR derivation requires evaluation of the second moment of the correlation function

$$\langle \hat{C}^2(\boldsymbol{\rho}_1) \rangle = \frac{1}{T_I^2} \int_{-T_I/2}^{T_I/2} dt \int_{-T_I/2}^{T_I/2} du \langle \hat{i}_1(t) \hat{i}_2(t) \hat{i}_1(u) \hat{i}_2(u) \rangle. \quad (\text{A.22})$$

We can use Eqs (3.5) and to write the currents in terms of the detected field operators $\hat{E}_1(\boldsymbol{\rho}, t)$ and $\hat{E}_2(\boldsymbol{\rho}, t)$ as

$$\begin{aligned} & \langle \hat{i}_1(t) \hat{i}_2(t) \hat{i}_1(u) \hat{i}_2(u) \rangle \\ &= q^4 A_1^2 \int d\tau_1 \int d\tau_2 \int d\tau_3 \int d\tau_4 \int_{\mathcal{A}_2} d\boldsymbol{\rho}' \int_{\mathcal{A}_2} d\boldsymbol{\rho}'' h(t - \tau_1) h(t - \tau_2) h(u - \tau_3) h(u - \tau_4) \\ & \times \langle \hat{E}_1^\dagger(\boldsymbol{\rho}_1, \tau_1) \hat{E}_1(\boldsymbol{\rho}_1, \tau_1) \hat{E}_2^\dagger(\boldsymbol{\rho}', \tau_2) \hat{E}_2(\boldsymbol{\rho}', \tau_2) \hat{E}_1^\dagger(\boldsymbol{\rho}_1, \tau_3) \hat{E}_1(\boldsymbol{\rho}_1, \tau_3) \hat{E}_2^\dagger(\boldsymbol{\rho}'', \tau_4) \hat{E}_2(\boldsymbol{\rho}'', \tau_4) \rangle. \end{aligned}$$

We now use the commutator relationships in Eqs (3.1) and (3.2) to normally order the field operators as

$$\begin{aligned} & \langle \hat{E}_1^\dagger(\boldsymbol{\rho}_1, \tau_1) \hat{E}_1(\boldsymbol{\rho}_1, \tau_1) \hat{E}_2^\dagger(\boldsymbol{\rho}', \tau_2) \hat{E}_2(\boldsymbol{\rho}', \tau_2) \hat{E}_1^\dagger(\boldsymbol{\rho}_1, \tau_3) \hat{E}_1(\boldsymbol{\rho}_1, \tau_3) \hat{E}_2^\dagger(\boldsymbol{\rho}'', \tau_4) \hat{E}_2(\boldsymbol{\rho}'', \tau_4) \rangle \\ &= \langle \hat{E}_1^\dagger(\boldsymbol{\rho}_1, \tau_1) \hat{E}_2^\dagger(\boldsymbol{\rho}', \tau_2) \hat{E}_1^\dagger(\boldsymbol{\rho}_1, \tau_3) \hat{E}_2^\dagger(\boldsymbol{\rho}'', \tau_4) \hat{E}_1(\boldsymbol{\rho}_1, \tau_1) \hat{E}_2(\boldsymbol{\rho}', \tau_2) \hat{E}_1(\boldsymbol{\rho}_1, \tau_3) \hat{E}_2(\boldsymbol{\rho}'', \tau_4) \rangle \\ & \times \langle \hat{E}_1^\dagger(\boldsymbol{\rho}_1, \tau_1) \hat{E}_2^\dagger(\boldsymbol{\rho}', \tau_2) \hat{E}_1^\dagger(\boldsymbol{\rho}_1, \tau_3) \hat{E}_1(\boldsymbol{\rho}_1, \tau_1) \hat{E}_1(\boldsymbol{\rho}_1, \tau_3) \hat{E}_2(\boldsymbol{\rho}'', \tau_4) \rangle \delta(\boldsymbol{\rho}' - \boldsymbol{\rho}'') \delta(\tau_2 - \tau_4) \\ & \times \langle \hat{E}_1^\dagger(\boldsymbol{\rho}_1, \tau_1) \hat{E}_2^\dagger(\boldsymbol{\rho}', \tau_2) \hat{E}_2^\dagger(\boldsymbol{\rho}'', \tau_4) \hat{E}_2(\boldsymbol{\rho}', \tau_2) \hat{E}_1(\boldsymbol{\rho}_1, \tau_3) \hat{E}_2(\boldsymbol{\rho}'', \tau_4) \rangle \delta(\tau_1 - \tau_3) \\ & \times \langle \hat{E}_1^\dagger(\boldsymbol{\rho}_1, \tau_1) \hat{E}_2^\dagger(\boldsymbol{\rho}', \tau_2) \hat{E}_1(\boldsymbol{\rho}_1, \tau_3) \hat{E}_2(\boldsymbol{\rho}'', \tau_4) \rangle \delta(\boldsymbol{\rho}' - \boldsymbol{\rho}'') \delta(\tau_2 - \tau_4) \delta(\tau_1 - \tau_3). \end{aligned}$$

Using Eq (3.6) we can write this in terms of the propagated field operators \hat{E}'_S and \hat{E}'_R . Since the terms are normally ordered, and the vacuum terms are zero mean and commute

with each other and the field operators, this is simply

$$\begin{aligned}
& \langle \hat{E}_1^\dagger(\boldsymbol{\rho}_1, \tau_1) \hat{E}_1(\boldsymbol{\rho}_1, \tau_1) \hat{E}_2^\dagger(\boldsymbol{\rho}', \tau_2) \hat{E}_2(\boldsymbol{\rho}', \tau_2) \hat{E}_1^\dagger(\boldsymbol{\rho}_1, \tau_3) \hat{E}_1(\boldsymbol{\rho}_1, \tau_3) \hat{E}_2^\dagger(\boldsymbol{\rho}'', \tau_4) \hat{E}_2(\boldsymbol{\rho}'', \tau_4) \rangle \\
&= \eta^4 \langle \hat{E}_R^\dagger(\boldsymbol{\rho}_1, \tau_1) \hat{E}_T^\dagger(\boldsymbol{\rho}', \tau_2) \hat{E}_R^\dagger(\boldsymbol{\rho}_1, \tau_3) \hat{E}_T^\dagger(\boldsymbol{\rho}'', \tau_4) \hat{E}_R(\boldsymbol{\rho}_1, \tau_1) \hat{E}_T(\boldsymbol{\rho}', \tau_2) \hat{E}_R(\boldsymbol{\rho}_1, \tau_3) \hat{E}_T(\boldsymbol{\rho}'', \tau_4) \rangle \\
&\times \eta^3 \langle \hat{E}_R^\dagger(\boldsymbol{\rho}_1, \tau_1) \hat{E}_T^\dagger(\boldsymbol{\rho}', \tau_2) \hat{E}_R^\dagger(\boldsymbol{\rho}_1, \tau_3) \hat{E}_R(\boldsymbol{\rho}_1, \tau_1) \hat{E}_R(\boldsymbol{\rho}_1, \tau_3) \hat{E}_T(\boldsymbol{\rho}'', \tau_4) \rangle \delta(\boldsymbol{\rho}' - \boldsymbol{\rho}'') \delta(\tau_2 - \tau_4) \\
&\times \eta^3 \langle \hat{E}_R^\dagger(\boldsymbol{\rho}_1, \tau_1) \hat{E}_T^\dagger(\boldsymbol{\rho}', \tau_2) \hat{E}_T^\dagger(\boldsymbol{\rho}'', \tau_4) \hat{E}_T(\boldsymbol{\rho}', \tau_2) \hat{E}_R(\boldsymbol{\rho}_1, \tau_3) \hat{E}_T(\boldsymbol{\rho}'', \tau_4) \rangle \delta(\tau_1 - \tau_3) \\
&\times \eta^2 \langle \hat{E}_R^\dagger(\boldsymbol{\rho}_1, \tau_1) \hat{E}_T^\dagger(\boldsymbol{\rho}', \tau_2) \hat{E}_R(\boldsymbol{\rho}_1, \tau_3) \hat{E}_T(\boldsymbol{\rho}'', \tau_4) \rangle \delta(\boldsymbol{\rho}' - \boldsymbol{\rho}'') \delta(\tau_2 - \tau_4) \delta(\tau_1 - \tau_3).
\end{aligned}$$

We again have the correlation second moment as a sum of four terms, $\langle \hat{C}^2(\boldsymbol{\rho}_1) \rangle = T_1 + T_2 + T_3 + T_4$, where

$$\begin{aligned}
T_1 &= \int d\tau_1 \int d\tau_2 \int d\tau_3 \int d\tau_4 \int_{A_2} d\boldsymbol{\rho}' \int_{A_2} d\boldsymbol{\rho}'' h(t - \tau_1) h(t - \tau_2) h(u - \tau_3) h(u - \tau_4) q^4 \eta^4 A_1^2 \\
&\quad \times \langle \hat{E}_R^\dagger(\boldsymbol{\rho}_1, \tau_1) \hat{E}_T^\dagger(\boldsymbol{\rho}', \tau_2) \hat{E}_R^\dagger(\boldsymbol{\rho}_1, \tau_3) \hat{E}_T^\dagger(\boldsymbol{\rho}'', \tau_4) \hat{E}_R(\boldsymbol{\rho}_1, \tau_1) \hat{E}_T(\boldsymbol{\rho}', \tau_2) \hat{E}_R(\boldsymbol{\rho}_1, \tau_3) \hat{E}_T(\boldsymbol{\rho}'', \tau_4) \rangle, \\
T_2 &= \int d\tau_1 \int d\tau_2 \int d\tau_3 \int_{A_2} d\boldsymbol{\rho}' h(t - \tau_1) h(t - \tau_2) h(u - \tau_3) h(u - \tau_2) q^4 \eta^3 A_1^2 \\
&\quad \times \langle \hat{E}_R^\dagger(\boldsymbol{\rho}_1, \tau_1) \hat{E}_T^\dagger(\boldsymbol{\rho}', \tau_2) \hat{E}_R^\dagger(\boldsymbol{\rho}_1, \tau_3) \hat{E}_R(\boldsymbol{\rho}_1, \tau_1) \hat{E}_T(\boldsymbol{\rho}', \tau_2) \hat{E}_R(\boldsymbol{\rho}_1, \tau_3) \rangle, \\
T_3 &= \int d\tau_1 \int d\tau_2 \int d\tau_4 \int_{A_2} d\boldsymbol{\rho}' \int_{A_2} d\boldsymbol{\rho}'' h(t - \tau_1) h(t - \tau_2) h(u - \tau_1) h(u - \tau_4) q^4 \eta^3 A_1 \\
&\quad \times \langle \hat{E}_R^\dagger(\boldsymbol{\rho}_1, \tau_1) \hat{E}_T^\dagger(\boldsymbol{\rho}', \tau_2) \hat{E}_T^\dagger(\boldsymbol{\rho}'', \tau_4) \hat{E}_R(\boldsymbol{\rho}_1, \tau_1) \hat{E}_T(\boldsymbol{\rho}', \tau_2) \hat{E}_T(\boldsymbol{\rho}'', \tau_4) \rangle, \\
T_4 &= \int d\tau_1 \int d\tau_2 h(t - \tau_1) h(t - \tau_2) h(u - \tau_1) h(u - \tau_2) q^4 \eta^2 \\
&\quad \times \langle \hat{E}_R^\dagger(\boldsymbol{\rho}_1, \tau_1) \hat{E}_T^\dagger(\boldsymbol{\rho}', \tau_2) \hat{E}_R(\boldsymbol{\rho}_1, \tau_1) \hat{E}_T(\boldsymbol{\rho}', \tau_2) \rangle.
\end{aligned}$$

We now have four terms which can be described as arising from: the randomness in the fields from the source fluctuations and scattering; the source randomness in the reference field mixing with the fluctuations from the measurement of the signal field; the source randomness in the signal field mixing with the fluctuations from the measurement of the reference field; and the beating of the randomness from the two quantum measurements of the Gaussian field operators. For simplicity, we will evaluate these terms separately

We first back propagate $E'_T(\boldsymbol{\rho}, t)$ to $E'_S(\boldsymbol{\rho}', t)$ by Eq (3.3), making our noise terms a functions of normally ordered Gaussian moments, to which we can apply the moment factoring theorem to obtain an expression which is a sum of the product of second order moments. In the classical case, the signal and reference fields had phase-insensitive cross and auto correlations given by Eq (2.6). For the SPDC ghost imager we have a phase-sensitive cross correlation given by Eq (3.7) and a phase-insensitive autocorrelation for each field given by Eq (3.8). These propagate into the far field as Eq (3.9) and (3.10). After performing Gaussian moment factoring our terms are the product two different correlation functions, one of which is complex. However, after some additional manipulation the temporal and spatial terms can be separated, and evaluated as they were for the classical case. Substituting in our dimensionless brightness term \mathcal{I} , the first term T_1 evaluates to

$$T_1 = \frac{16q^4\eta^4 A_1^2 A_2^2 \mathcal{I}^4}{\pi^2 L^4 T_0^4 \rho_L^4} \left[\frac{A'_T}{\sqrt{2\pi}\rho_L^2} \frac{T_0}{T_I} + \left(1 + \frac{1}{\sqrt{2\pi}\mathcal{I}} + \frac{1}{8\pi\mathcal{I}^2} \right) \mathcal{T}^2(-\boldsymbol{\rho}_1) \right. \\ \left. + \frac{A'_F}{\sqrt{2\pi}\rho_L^2} \frac{T_0}{T_I} \frac{L^2}{A_2\pi k_0^2 \rho_L^2} + 2\pi^2 \Gamma \left(1 + \frac{1}{\sqrt{2\pi}\mathcal{I}} + \frac{1}{8\pi\mathcal{I}^2} \right) \frac{L^2}{A_2\pi k_0^2 \rho_L^2} \mathcal{T}^2(-\boldsymbol{\rho}_1) \right]$$

The remaining noise terms are evaluated in the same manner, giving us

$$T_2 = \frac{16q^4\eta^3 A_1^2 A_2 \mathcal{I}^3}{\pi^2 L^2 T_0^3 T_I \rho_L^4} \left(\frac{1}{2\sqrt{2\pi}\mathcal{I}} + 1 \right) \mathcal{T}(-\boldsymbol{\rho}_1), \\ T_3 = \frac{16q^4\eta^3 A_1 A_2^2 \mathcal{I}^3}{\pi L^4 T_0^3 T_I \rho_L^2} \left(\frac{1}{2\sqrt{2\pi}\mathcal{I}} + 1 \right) \left[\frac{4}{3} + \frac{L^2}{\pi k_0^2 \rho_L^2 A_2} \right] \mathcal{T}^2(-\boldsymbol{\rho}_1), \\ T_4 = \frac{\sqrt{\pi} q^4 \eta^2 A_1 A_2 \mathcal{I}^2 \Omega_B}{\sqrt{2\pi^2} L^2 T_0^2 T_I \rho_L^2} \left(\frac{1}{2\sqrt{2\pi}\mathcal{I}} + 1 \right) \mathcal{T}(-\boldsymbol{\rho}_1).$$

Combining these terms, and substituting $a_0 = 2L/k_0\rho_L$, we have an expression for the second

moment of the correlation function

$$\begin{aligned}
\langle \hat{C}^2(\boldsymbol{\rho}_1) \rangle &= \frac{16q^4\eta^4 A_1^2 A_2^2 \mathcal{I}^4 T_0}{\pi^2 L^4 T_0^4 \rho_L^4} \frac{T_I}{T_I} \left[\frac{A'_T}{\sqrt{2\pi}\rho_L^2} + \frac{T_I}{T_0} \left(\frac{1}{2\sqrt{2\pi}\mathcal{I}} + 1 \right)^2 \mathcal{T}^2(-\boldsymbol{\rho}_1) \right. \\
&+ \frac{A'_F}{\sqrt{2\pi}\rho_L^2} \frac{a_0^2}{4\pi A_2} + \frac{T_I}{T_0} \frac{\Gamma}{2} \left(\frac{1}{2\sqrt{2\pi}\mathcal{I}} + 1 \right)^2 \frac{\pi a_0^2}{A_2} \mathcal{T}^2(-\boldsymbol{\rho}_1) + \left(\frac{1}{2\sqrt{2\pi}\mathcal{I}} + 1 \right) \frac{\mathcal{T}(-\boldsymbol{\rho}_1)L^2}{A_2 \mathcal{I} \eta} \\
&\left. + \left(\frac{1}{2\sqrt{2\pi}\mathcal{I}} + 1 \right) \frac{\pi \rho_L^2 \mathcal{T}^2(-\boldsymbol{\rho}_1)}{A_1 \mathcal{I} \eta} \left[\frac{4}{3} + \frac{a_0^2}{4\pi A_2} \right] + \left(\frac{1}{2\sqrt{2\pi}\mathcal{I}} + 1 \right) \frac{\mathcal{T}(-\boldsymbol{\rho}_1) \sqrt{\pi} L^2 T_0 \Omega_B \rho_L^2}{16\sqrt{2} A_1 A_2 \mathcal{I}^2 \eta^2} \right]
\end{aligned}$$

The mean of the correlation function is in Eq (3.16), and after substituting in our brightness term \mathcal{I} , we have a squared mean of

$$C_1(\boldsymbol{\rho}_1) = \frac{16q^4\eta^4 A_1^2 A_2^2 \mathcal{I}^4}{\pi^2 L^4 T_0^4 \rho_L^4} \mathcal{T}^2(-\boldsymbol{\rho}_1) \left(\frac{1}{2\sqrt{2\pi}\mathcal{I}} + 1 \right)^2, \quad (\text{A.23})$$

Combining this with our second moment, and substituting $\mathbb{I} = (1/(2\sqrt{2\pi}\mathcal{I}) + 1)$, we arrive at the SNR expression in Eq (3.18), which we reproduce here:

$$\begin{aligned}
\text{SNR} &= \frac{\frac{T_I}{T_0} \mathbb{I}^2}{\frac{A'_T + \frac{a_0^2 A'_F}{4\pi A_2}}{\sqrt{2\pi}\rho_L^2 \mathcal{T}(\boldsymbol{\rho}_1)^2} + \frac{T_I}{T_0} \frac{\Gamma \pi a_0^2}{2A_2 \mathcal{T}(\boldsymbol{\rho}_1)^2} \mathbb{I}^2 + \left(\frac{L^2}{A_2 \mathcal{I} \eta \mathcal{T}(\boldsymbol{\rho}_1)} + \frac{\pi \rho_L^2}{A_1 \mathcal{I} \eta} \left[\frac{4}{3} + \frac{a_0^2}{4\pi A_2} \right] + \frac{\sqrt{\pi} L^2 T_0 \Omega_B \rho_L^2}{16\sqrt{2} A_1 A_2 \mathcal{I}^2 \eta^2 \mathcal{T}(\boldsymbol{\rho}_1)} \right) \mathbb{I}}.
\end{aligned} \quad (\text{A.24})$$

Bibliography

- [1] T. B. Pittman, Y. Shih, D. V. Strekalov, and A. V. Sergienko, “Optical imaging by means of two-photon quantum entanglement,” *Phys. Rev. A* **52**, 3429 (1995).
- [2] A. Valencia, G. Scarcelli, M. D. Angelo, and Y. Shih, “Two-photon imaging with thermal light,” *Phys. Rev. Lett.* **94**, 063601 (2005).
- [3] F. Ferri, D. Magatti, A. Gatti, M. Bache, E. Brambilla, and L. A. Lugiato, “High-resolution ghost image and ghost diffraction experiments with thermal light,” *Phys. Rev. Lett.* **94**, 183602 (2005).
- [4] B. I. Erkmen and J. H. Shapiro, “Unified theory of ghost imaging with Gaussian-state light,” *Phys. Rev. A* **77**, 043809 (2008).
- [5] J. H. Shapiro and B. I. Erkmen, “Ghost imaging: from quantum to classical to computational,” *Advances in Optics and Photonics* **2**, 405 (2010).
- [6] B. I. Erkmen and J. H. Shapiro, “Signal-to-noise ratio of Gaussian-state ghost imaging,” *Phys. Rev. A* **79**, 023833 (2009).
- [7] R. E. Meyers, K. S. Deacon, and Y. Shih, “Ghost-imaging experiment by measuring reflected photons,” *Phys. Rev. A* **77**, 041801 (2008).
- [8] R. E. Meyers and K. S. Deacon, “Quantum ghost imaging experiments at ARL,” *Proc. SPIE* **7815**, 78150I (2010).
- [9] J. H. Shapiro, “Computational ghost imaging,” *Phys. Rev. A* **78**, 061802 (2008).

- [10] Y. Bromberg, O. Katz, and Y. Silberberg, “Ghost imaging with a single detector,” *Phys. Rev. A* **79**, 053840 (2009).
- [11] J. Cheng, “Ghost imaging through turbulent atmosphere,” *Opt. Express* **17**, 7916 (2009).
- [12] O. Katz, Y. Bromberg, and Y. Silberberg, “Compressive ghost imaging,” *Appl. Phys. Lett.* **95**, 131110 (2009).
- [13] R. G. Baraniuk, “Compressive sensing,” *IEEE Signal Process. Mag* **24**, 118 (2007).
- [14] E. J. Candes and M. B. Wakin, “An introduction to compressive sampling,” *IEEE Signal Process. Mag* **25**, 21 (2008).
- [15] J. H. Shapiro, B. A. Capron, and R. C. Harney, “Imaging and target detection with a heterodyne-reception optical radar,” *Appl. Opt.* **20**, 3292 (1981).
- [16] G. Scarcelli, V. Berardi, and Y. Shih, “Can two-photon correlation of chaotic light be considered as correlation of intensity fluctuations ?” *Phys. Rev. Lett.* **96**, 063602 (2006).
- [17] J. W. Strohbehn, ed., *Laser Beam Propagation in the Atmosphere* (Springer-Verlag, Berlin, 1978).
- [18] V. I. Tatarskii, A. Ishimaru, and V. U. Zavorotn, eds., *Wave Propagation in Random Media (Scintillation)* (The International Society for Optical Engineering, Bellingham, 1992).
- [19] V. I. Tatarskii, *Wave Propagation in Turbulent Medium* (McGraw-Hill, New York, 1961).
- [20] A. Ishimaru, *Wave Propagation and Scattering in Random Media*, vol. 2 (Academic Press, New York, 1978).
- [21] G. Gbur and E. Wolf, “Spreading of partially coherent beams in random media,” *J. Opt. Soc. Am. A* **19**, 1592 (2002).

- [22] A. Dogariu and S. Amarande, "Propagation of partially coherent beams: turbulence-induced degradation," *Opt. Lett.* **28**, 10 (2003).